FACULTY
OF MATHEMATICS
AND PHYSICS
Charles University

DOCTORAL THESIS

Jan Záhlava

Lightning-Related Electromagnetic Wave Phenomena in the Earth's Magnetosphere

Department of Surface and Plasma Physics

Supervisor of the doctoral thesis:	doc. RNDr. František Němec, PhD.
Study programme:	Physics
Study branch:	Physics of Plasmas and Ionized Media

Prague 2019

I declare that I carried out this doctoral thesis independently, and only with the cited sources, literature and other professional sources.

I understand that my work relates to the rights and obligations under the Act No. 121/2000 Sb., the Copyright Act, as amended, in particular the fact that the Charles University has the right to conclude a license agreement on the use of this work as a school work pursuant to Section 60 subsection 1 of the Copyright Act.

In Prague date ....

First, I would like to express gratitude to my supervisor František Němec for all the years of cooperation and his priceless contribution to my scientific growth. Heartly thank you also belongs to my colleagues who significantly contributed to papers published during my doctoral study, namely Ondřej Santolík and Ivana Kolmašová. I would like to also thank the scientists who made the spacecraft missions I used possible, in particular those of the CNES laboratories in France and the University of Iowa in the USA.

Second, I thank to all the colleagues at the Department of Surface and Plasma Physics, both students and employees for creating a friendly and inspiring environment.

Needless to say, I am infinitely grateful for the support and background provided by my family, who made my goals much easier to reach. Last but not least, my thanks belong also to all my friends who did a great job preserving my sanity and keeping me aware of the human aspects of life. For all, I feel obliged to mention two of them: Robert Keil and Ondřej Svatoš.

In addition to all the personal acknowledgments, I would like to also mention the Faculty of Mathematics and Physics itself and its teaching staff who have shown me an inspiring way to view not only the professional, but also the everyday problems.

Title: Lightning-Related Electromagnetic Wave Phenomena in the Earth's Magnetosphere

Author: Jan Záhlava

Department: Department of Surface and Plasma Physics

Supervisor: doc. RNDr. František Němec, PhD., Department of Surface and Plasma Physics

Abstract: The thesis focuses on lightning-related electromagnetic wave phenomena observed by spacecraft in the Earth's inner magnetosphere. Two different approaches are used to identify the frequency and spatial extent where lightning-generated emissions significantly contribute to the overall wave intensity. First, whistler detections onboard the DEMETER spacecraft are used to sort the measurements according to the whistler activity. Second, we use a geographic distribution of lightning activity and analyze a dependence of the overall wave intensity on geomagnetic longitude. We show that, especially during the night, the overall wave intensity observed in the plasmasphere is well correlated with lightning activity. The other focus of the study is on special electromagnetic wave events consisting of alternating frequency bands of enhanced and reduced wave intensity formed in the ionosphere due to lightning. We analyze their occurrence and parameters, and we suggest a possible mechanism of their formation.

Keywords: lightning, waves in plasma, whistlers, plasmasphere

Název: Elektromagnetické vlnové jevy v magnetosféře Země související s bleskovou aktivitou

Autor: Jan Záhlava

Katedra: Katedra fyziky povrchů a plazmatu

Vedoucí: doc. RNDr. František Němec, PhD., Katedra fyziky povrchů a plazmatu

Abstrakt: V práci se zaměřujeme na družicová pozorování elektromagnetických vlnových jevů ve vnitřní magnetosféře Země spojených s bleskovou aktivitou. Používáme dva různé způsoby určení frekvenčního a prostorového rozsahu, ve kterém emise vznikající při bleskové aktivitě významně přispívají k celkové měřené vlnové intenzitě. Prvním způsobem je využití detekce hvizdů na družici DEMETER k roztřídění měření prováděných během různých úrovní hvizdové aktivity. Druhý přístup využívá geografické rozložení bleskové aktivity, kdy zkoumáme závislost intenzity vln na geomagnetické délce. Ukazuje se, že, především v noci, je celková intenzita dobře korelována s bleskovou aktivitou. V další části práce se zabýváme speciálními vlnovými událostmi tvořenými střídajícími se frekvenčními pásy se zvýšenou a sníženou intenzitou, které vznikají v ionosféře v důsledku bleskové aktivity. Analyzovali jsme jejich výskyt a parametry a navrhli možný způsob jejich vzniku.

Klíčová slova: blesková aktivita, vlny v plazmatu, hvizdy, plazmasféra

Contents

1. Introduction

1.1 Earth's Magnetosphere

The anti-Sun-ward orientation of comet tails led to the theory of a particle flow coming from the Sun. Parker [1958] has suggested that the upper layers of the Sun continuously expand to the surrounding space forming the solar wind. The outflowing plasma consists of electrons and protons with a small varying portion of alpha particles and a tiny addition of ions of heavier elements. Mean free path of the particles is approximately 1 Astronomical Unit, and solar wind can be therefore considered as nearly collision less on the Sun-Earth distance scale. Thereby the plasma environment exhibits a very good conductivity, and the flow drags the frozen in magnetic field of the Sun. Given the rotation of the Sun and the continual plasma outflow, magnetic field lines form a signature shape, the Parker spiral.

All the planetary objects in the solar system, including the Earth, are strongly influenced by the interaction with the solar wind. The intrinsic magnetic field of the Earth provides an effective protection from the solar wind particle flux [Chapman and Ferraro, 1931]. A boundary behind which the solar wind cannot access is thus formed at the surface of the equilibrium between the pressures produced primarily by the Earth's magnetic field on one side and the dynamic pressure of the solar wind on the other. Close to the subsolar point, this boundary called magnetopause, can be usually found at a radial distance between about 8 and 11 R_E [Cahill and Amazeen, 1963]. Due to the supersonic nature of the solar wind, another boundary, called bow shock, is formed upstream from the magnetopause. The roughly dipole magnetic field of the Earth is reshaped by its interaction with the solar wind and the associated current systems, resulting in the compression on the dayside and a significant prolongation on the nightside, where so called magnetotail is formed.

1.1.1 Van Allen Radiation Belts

Some of the solar wind particles can penetrate into the magnetosphere, where they can get trapped. Without further interactions, such trapped charged particles have rather limited possibilities of motion in the Earth's magnetic field.

In any magnetic field, charged particles can move freely along the field line, however, any movement in a perpendicular direction is transformed by the Lorentz force to the gyration around the field line. The angular frequency of this gyration (cyclotron frequency) is given by the magnitude of the local magnetic field B and the particle's charge to mass ratio Q/m:

$$\Omega = \frac{QB}{m}. \tag{1.1}$$

Every periodic motion leads to preservation of some quantity given by the action integral

$$J = \oint p \mathrm{d}q, \tag{1.2}$$

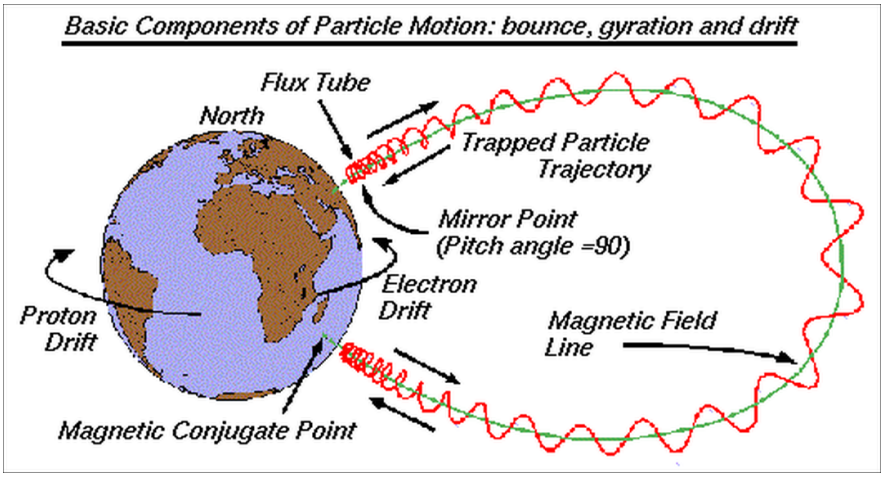

Figure 1.1: Schematic view of the charged particle movements in the Earth's magnetic field. Reprinted from Markgraf and Montenbruck [2004].

where q is a generalized coordinate and p is a generalized momentum [Goldstein, 1965]. In the case of the aforementioned gyration motion, the preserved quantity is constituted by the magnetic moment μ given by

$$\mu = \frac{mv_{\perp}^2}{2B}, \tag{1.3}$$

where $v_{\perp}$ is the component of the velocity vector perpendicular to the magnetic field.

Apart from the gyration, the trapped particles propagate along the magnetic field lines. The magnitude of the magnetic field, however, does not remain constant along the field line, increasing toward lower radial distances and larger latitudes. Given the preservation of the magnetic moment μ and the total kinetic energy of the particle ($\frac{1}{2}m\left(v_{\parallel}^2 + v_{\perp}^2\right)$), the ratio between the parallel and the perpendicular component of the particle velocity is destined to change during the particle movement. Consequently, the particle may reach a point where the magnetic field magnitude is so large that all the particle kinetic energy is stored in the perpendicular component. At such point, the particle gets reflected and it begins to move in the opposite direction along the field line. This effect is called magnetic mirroring.

The mirroring point is given by the growth of the magnetic field magnitude along the field line and by the fraction of energy momentarily stored in the perpendicular component of the velocity:

$$\frac{B}{B_m} = \left(\frac{v_{\perp}}{v}\right)^2, \tag{1.4}$$

where B is the magnetic field magnitude at the point where the total and perpendicular velocities v and $v_{\perp}$ are measured and B_m is the magnetic field magnitude needed for the mirroring to happen. Introducing the "pitch angle" α (the angle between the velocity vector and the ambient magnetic field), equation (1.4) can be rewritten as:

$$\sin^2\alpha = \frac{B}{B_m}. \tag{1.5}$$

In the Earth's magnetosphere, the trapped particles need to get reflected above some minimal altitude in order not to collide with the atmosphere, as such collisions would result in their scattering and precipitation. The minimal pitch-angle needed to preserve the bouncing motion defines the bounce loss cone.

Finally, the bouncing particles circle the Earth in the azimuthal direction due to the "grad B" and curvature drifts. Directions of these drifts are charge sensitive and, therefore, electrons move eastward, whereas positively charged protons move westward. The charge dependent direction of drift thus results in the ring current, which effectively weakens the magnitude of the Earth's magnetic field at lower radial distances. All the three aforementioned movements of charged particles trapped in the Earth's magnetic field are illustrated in Figure 1.1.

The adiabatic invariants are preserved only if the defining environment changes slowly with respect to the periods of individual movements. This condition is, however, often violated in case of the Earth's magnetosphere, for example due to the influence of varying solar wind properties. Additionally, the adiabatic invariants may be violated due to the interaction of trapped particles with electromagnetic waves of various origins and frequencies [e.g., Voss et al., 1998, Bortnik et al., 2006a, Gemelos et al., 2009, Bourriez et al., 2016]. The violation of adiabatic invariants then ultimately results in changes of the particle energy and pitch angle. All such processes result in energetic electrons being trapped primarily in two donut-shaped areas called the Van Allen radiation belts [Van Allen, 1958]. The shape of the Van Allen belts is illustrated in Figure 1.2.

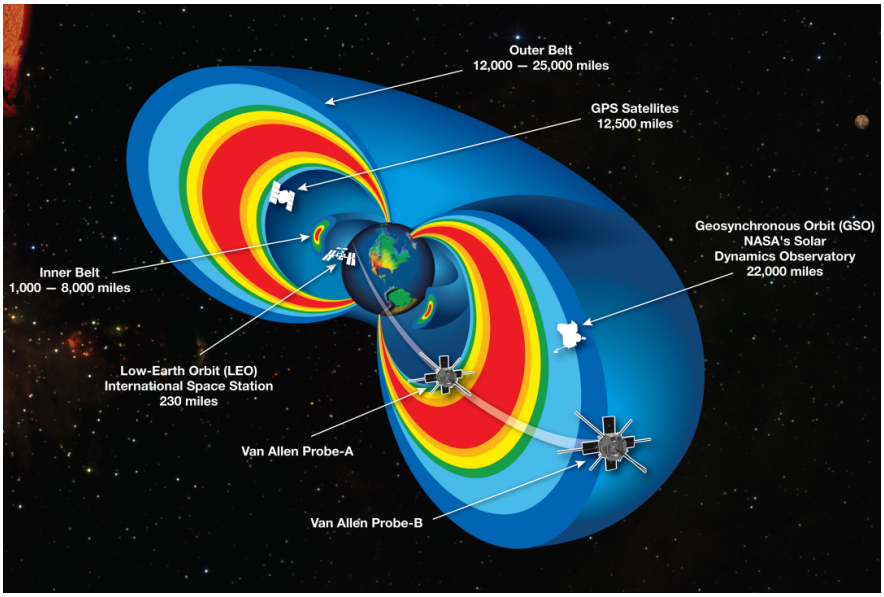

Figure 1.2: Illustration of the Van Allen radiation belts. Reprinted from Zell [2015].

Originally, it was believed that high-energy particles populate two distinct areas, one closer to the Earth dominated by protons and the other at larger radial distances dominated by electrons [Van Allen, 1958, Van Allen and Frank, 1959]. Later, Johnson and Kierein [1992] and Blake et al. [1997] showed that electrons with slightly lower energies, i.e., below about 1 MeV, are present in both areas, however, there is a deep "slot region" in between with significantly

reduced electron population. Recently, the Van Allen Probes mission has brought several additional interesting findings. Namely, Baker et al. [2014] have shown that a rather sharp drop of energetic electron flux is typically observed at L-shells lower than about 2.8, which they interpreted as an "impenetrable barrier". The drop gets even sharper for ultra-relativistic electrons ($> \sim$ 2 MeV). Regarding the ultra-relativistic electrons, Baker et al. [2013] reported a discovery of an unexpectedly long-lived storage ring of theirs, effectively forming the outermost third radiation belt.

1.1.2 Plasmasphere

The Earth's surroundings is filled with plasma extending from the ionosphere. In analogy to the Earth's atmosphere, a simple naive expectation might be that the number density should decrease approximately exponentially with the radial distance. However, the observations by Storey [1953], who analyzed dispersions of radio signals from lightning, i.e., whistlers (see Section 1.2), have shown a surprising result. Considering the propagation approximately along the field line, which is a necessary condition for the ground observations of whistlers, he estimated the plasma number density at several Earth radii to be as high as about 400 cm^{-3}, way larger than originally expected. These results were then confirmed by Carpenter [1963], who, additionally, revealed a knee-like behavior of the plasma number density as a function of L, the McIlwain's parameter [McIlwain, 1961], in the range of about $2 < L < 5$. The density drop (plasmapause) separating the high density plasmasphere from the low density plasma trough was revealed also by the spacecraft mission LUNIK. However, it was only published after being confirmed by Carpenter's results. The key plot is shown in Figure 1.3.

Generally, the estimation of the cold plasma density by dedicated spacecraft measurements has to deal with the issues of spacecraft potential due to the charging. Indirect method for plasma number density estimation was therefore implemented, e.g., onboard the Van Allen Probes using the electromagnetic waves' measurements (see Section 3.2.2). The method uses the upper hybrid resonant frequency estimation and magnetic field measurement to derive the plasma number density [Kurth et al., 2015].

The rather sudden drop of plasma number density is result of particle convection in the Earth's magnetosphere. This flow is governed by two main processes: (i) co-rotation of plasma with the Earth, which is dominant at low radial distances, and (ii) a solar wind induced convection. Both mentioned schemes, as well as their superposition are shown in Figure 1.4. The dashed line represents the last closed equipotential and it corresponds to the plasmapause position.

Two different kinds of equipotentials can be seen in Figure 1.4: (i) at low radial distances, they are closed around the Earth and (ii) beyond the plasmapause, the equipotentials extend into the magnetotail. Any cold plasma particles on the latter equipotentials eventually reach the region where they can escape to the open space. No particles are therefore supposed to be convected back to lower radial distances. Since the refilling by the ionospheric plasma is rather slow compared to the convection losses, the plasma density outside the plasmasphere is supposed to stay rather low.

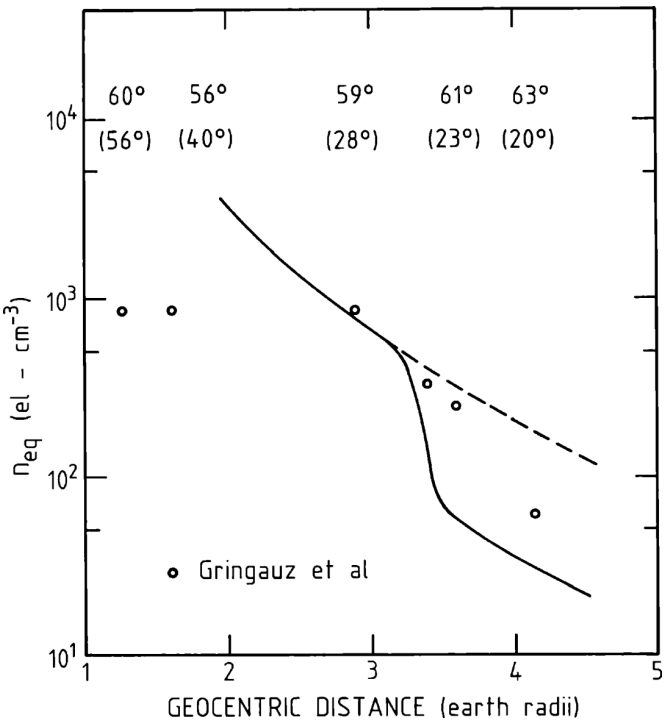

Figure 1.3: The solid curve shows the electron density profile derived from whistler measurements as a function of the geocentric distance. The circles represent the ion density measured by LUNIK 2 spacecraft. The upper and lower rows of numbers represent invariant latitudes and latitudes of the LUNIK 2 spacecraft, respectively. Reprinted from Carpenter [1965].

1.2 Whistlers

In this section, we present a theory of propagation of electromagnetic waves in the cold plasma approximation and, in particular, we derive the dispersion relation of the Whistler mode plasma waves. The presented theory assumes a linear wave behavior, hence, that the wave properties do not depend on its amplitude. Additionally, we presume that the environment does not change on distances comparable to the wavelength. Any propagating disturbance (wave) can be then at any given location $\vec{r}$ and time t written as a sum of individual planar waves in the form:

$$\vec{L}\left(\vec{r},t\right) = \Re\left\{\hat{L}\mathrm{e}^{i\left(\vec{k}\cdot\vec{r}-\omega t\right)}\right\}, \tag{1.6}$$

where $\hat{L}$ is the complex amplitude, $\vec{k}$ is the wave vector and ω represents the angular frequency. This notation further allows to rewrite differential operators in the following way:

$$\begin{aligned} \frac{\partial \vec{L}}{\partial t} &\rightarrow -i\omega\vec{L}, \\ \nabla\times\vec{L} &\rightarrow i\vec{k}\times\vec{L}, \\ \nabla\cdot\vec{L} &\rightarrow i\vec{k}\cdot\vec{L}. \end{aligned} \tag{1.7}$$

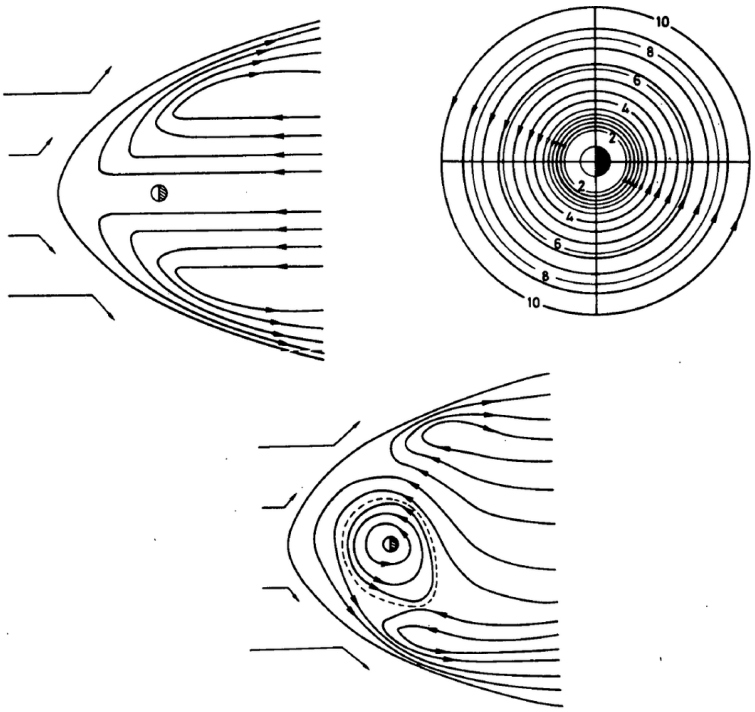

Figure 1.4: Equatorial plane view of the equipotentials of the electric field in the magnetosphere. The top left panel shows the component induced by the solar wind, the top right panel represents the co-rotational effect, and the bottom panel depicts the superposed field. The dashed curve shows the last closed equipotential, corresponding to the plasmapause. Adapted from Nishida [1966].

The electric and magnetic fields are governed by the set of Maxwell equations:

$$\begin{aligned} \nabla \times \vec{E} &= -\frac{\partial \vec{B}}{\partial t}, \\ \nabla \times \vec{B} &= \mu_0 \left[\vec{J} + \varepsilon_0 \frac{\partial \vec{E}}{\partial t} \right], \\ \nabla \cdot \vec{E} &= \frac{\varrho}{\varepsilon_0}, \\ \nabla \cdot \vec{B} &= 0, \end{aligned} \tag{1.8}$$

where $\vec{E}$ and $\vec{B}$ represent the electric and magnetic field intensities, respectively, μ_0 and ε_0 respectively represent the permeability and permittivity of vacuum, ϱ is the charge density and $\vec{J}$ stands for the electric current density. Using the equivalence $c^2 = 1/(\varepsilon_0 \mu_0)$ the wave equation can be derived in the form:

$$\nabla \times \nabla \times \vec{E} + \frac{1}{c^2} \frac{\partial^2 \vec{E}}{\partial t^2} + \mu_0 \frac{\partial \vec{J}}{\partial t} = 0. \tag{1.9}$$

Assuming further that the current density is proportional to the electric field and introducing the electric conductivity tensor $\overleftrightarrow{\sigma}$ in the form

$$\vec{J} = \overleftrightarrow{\sigma} \cdot \vec{E}, \tag{1.10}$$

we can define the permittivity tensor

$$\overleftrightarrow{\varepsilon} = \overleftrightarrow{\mathbb{1}} + \frac{i\,\overleftrightarrow{\sigma}}{\varepsilon_0 \omega}, \tag{1.11}$$

and rewrite the wave equation as

$$n^2 \hat{k}\hat{k} \cdot \vec{E} - n^2 \vec{E} + \overleftrightarrow{\varepsilon} \cdot \vec{E} = 0, \tag{1.12}$$

where $n = kc/\omega$ is the refractive index and $\hat{k}$ is a unity vector in direction of the wave vector $\vec{k}$.

The ambient magnetic field vector $\vec{B}_0$ defines a direction particularly significant for the wave propagation. It is therefore convenient to relate any wave propagation to this direction. Without loss of generality, we can investigate the problem in such a coordinate system that the ambient magnetic field is oriented along the z-axis, i.e., $\vec{B}_0 = (0, 0, B_0)$. We will further assume that $B_0 \gg B$, i.e., the ambient magnetic field is significantly stronger than the magnetic field related to the waves.

Given these assumptions, the permittivity tensor (1.11) can be expressed using the Stix coefficients [Stix, 1992] as:

$$\overleftrightarrow{\varepsilon} = \begin{pmatrix} S & iD & 0 \\ -iD & S & 0 \\ 0 & 0 & P \end{pmatrix}, \tag{1.13}$$

where $S = \frac{1}{2}(R + L)$, $D = \frac{1}{2}(R - L)$, and R, L, and P are defined as follows:

$$\begin{aligned} R &= 1 - \sum_i \frac{\Pi_i^2}{\omega(\omega + \Omega_i)} \\ L &= 1 - \sum_i \frac{\Pi_i^2}{\omega(\omega - \Omega_i)} \\ P &= 1 - \sum_i \frac{\Pi_i^2}{\omega^2}, \end{aligned} \tag{1.14}$$

where $\Pi_i = \sqrt{(n_i q_i^2)/(\varepsilon_0 m_i)}$ and $\Omega_i = (B_0 q_i)/m_i$ represent respectively the plasma and cyclotron frequencies corresponding to individual particle species. Note that the charge q_i also includes the sign, and, therefore, the cyclotron frequencies can be both positive and negative.

The wave equation (1.12) can be then expressed in a matrix form

$$\begin{pmatrix} S - n^2\cos^2\Theta & iD & n^2\sin\Theta\cos\Theta \\ -iD & S - n^2 & 0 \\ n^2\sin\Theta\cos\Theta & 0 & P - n^2\sin^2\Theta \end{pmatrix} \begin{pmatrix} E_x \\ E_y \\ E_z \end{pmatrix} = 0, \tag{1.15}$$

where Θ is the angle between the wave vector $\vec{k}$ and the ambient magnetic field $\vec{B}_0$. In order to obtain a non-zero solution for $\vec{E}$, determinant of the equation matrix has to be zero. Such condition can be written in the form of a bi-quadratic equation for the refraction index n:

$$\left(S\sin^2\Theta + P\cos^2\Theta\right) n^4 - \left[RL\sin^2\Theta + PS\left(1 + \cos^2\Theta\right)\right] n^2 + PRL = 0 \tag{1.16}$$

Given the wave and plasma parameters, one can therefore obtain up to two wave modes. For the field-aligned propagation at a frequency below the min $\{\Omega_e, \Pi_e\}$, the solutions for n^2 simplify to

$$n^2 = S \pm D = R \text{ or } L, \tag{1.17}$$

corresponding to either right- or left-handed polarized wave. Evaluating the coefficients, it turns out that between the proton cyclotron frequency Ω_i and the frequency $\omega_L = \frac{1}{2}\left(-\Omega_e + \sqrt{\Omega_e^2 + 4\Pi_e}\right)$, the value of L is negative, and, therefore, only the right-handed polarized wave can propagate.

The following calculations are done with several simplifying assumptions, specifically:

- Only the electron components in the Stix coefficients L, P, R are used (they are significantly larger than the rest).
- The wave vector is nearly aligned with the ambient magnetic field, i.e., Θ is close to zero.
- We only assume a wave with frequency $\omega \ll \min\{\Omega_e, \Pi_e\}$.

This allows us to simplify the formula

$$n^2 = \frac{k^2 c^2}{\omega^2} = R \approx \frac{\Pi_e^2}{\Omega_e \omega}. \tag{1.18}$$

From that we obtain the group velocity

$$v_g = \frac{\partial \omega}{\partial k} \approx \frac{2k\Omega_e c^2}{\Pi_e^2} = \frac{2c\sqrt{|\Omega_e|}}{\Pi_e}\sqrt{\omega}. \tag{1.19}$$

This shows that the higher the wave frequency, the larger the group velocity. When we calculate a duration T of the wave propagation under given conditions, we obtain

$$T = \int \frac{\mathrm{d}s}{v_g} \approx \frac{1}{2c}\frac{1}{\sqrt{\omega}} \int \frac{\Pi_e}{\sqrt{|\Omega_e|}} \mathrm{d}s, \tag{1.20}$$

which shows that the propagation duration depends on the inverse square root of wave frequency and on the environment properties.

Such behavior can be well observed in the case of lightning-generated emissions. A lightning stroke produces a short wide-band emission which can escape the Earth–ionosphere waveguide (see Section 1.4) and propagate through the plasmasphere. It can be then observed either in the magnetically conjugated point or, after a ionospheric reflection, in the point of origin. The dispersed wide-band emission results in a characteristic decreasing frequency-time pattern, which, transformed to sound, has given whistlers their name. Under favorable conditions, ground observations can show long trains of consecutive whistlers with increasing dispersions. An example of such event is shown in Figure 1.5. The black ellipse marks the parental lightning stroke.

The analyzed situation of nearly exactly field aligned wave propagation can be often justified by whistlers being "ducted" in channels of slightly different plasma number density formed along some magnetic field lines [Helliwell, 2014].

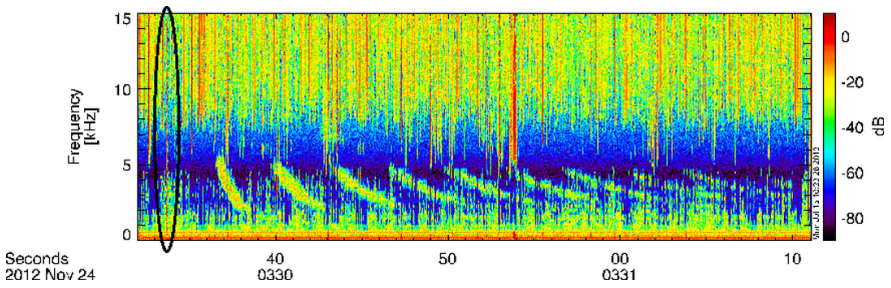

Figure 1.5: Example of frequency-time spectrogram containing a whistler train. The black ellipse marks the parental stroke. Reprinted from University of Calgary [2012].

The frequency dependence and the possibility of ground observations of ducted whistlers made them very useful for the plasmasphere probing in the early days. Since Storey [1953] described the pattern formation, it was possible to use the measured whistler dispersions to estimate plasma number density along whistler propagation paths. Great overview of lightning generated whistlers and their applications was compiled by Helliwell [1965, 2014]. However, whistlers can also propagate a different way, not following the ambient magnetic field. In such case, their trajectories are governed by gradient of the refractive index and the propagation is called "unducted" [Smith and Angerami, 1968, Santolík et al., 2009, Fišer et al., 2010]. Unducted whistlers can be observed only by spacecraft, since they generally propagate towards larger radial distances following a bouncing trajectory [Hughes, 1981, Bortnik et al., 2003, 2006a,b, Maxworth and Gołkowski, 2017]. The radial distance that the unducted waves can eventually reach depends on their frequency. Specifically, the higher the wave frequency, the lower the final radial distance.

Although lightning generated whistlers are historically the first and most studied whistler mode waves, many other waves with various, both known and unknown, origins propagate in the Earth's magnetosphere in the whistler mode. Considering the frequency range of interest of this thesis (between about 100 Hz and 20 kHz), we should mention in particular chorus and plasmaspheric hiss. These two wave event types play also very important role in the dynamics of the Van Allen radiation belts.

Chorus is generated by cyclotron resonance of embryonic whistler mode waves with electrons of the outer radiation belt [e.g., Allcock, 1957, Oliven and Gurnett, 1968, Sazhin and Hayakawa, 1992, Omura et al., 2008]. It consists of numerous consecutive rising or falling tones with periods of the order of seconds [Santolík et al., 2014]. Two bands of chorus are usually observed, one between about 0.1 and 0.45 Ω_e and the other between about 0.5 and 0.7 Ω_e [Tsurutani and Smith, 1974, 1977]. Chorus is mostly observed outside the plasmasphere [Burtis and Helliwell, 1969, Meredith et al., 2001], however, cases of chorus observations bt low altitude spacecraft were also reported [Santolík et al., 2006a]. Chorus emissions can eventually penetrate inside the plasmasphere and they are believed to be one of the sources of plasmaspheric hiss [e.g., Chum and Santolík, 2005, Bortnik et al., 2008, 2011a,b].

As the name suggests, plasmaspheric hiss occurs nearly exclusively inside the plasmasphere [Thorne et al., 1973, Meredith et al., 2004]. It is an unstructured

whistler mode emission observed at frequencies below about 2 kHz [Hayakawa and Sazhin, 1992]. Intensity of plasmaspheric hiss is the largest between about 100 and 300 Hz [Thorne et al., 1973, Tsurutani et al., 2012, Li et al., 2015]. Recently, plasmaspheric hiss was also observed at frequencies of several tens of Hz [Li et al., 2013]. It is supposed to play the most important role in the precipitation of the slot region electrons with energies ranging from tens of keV up to several MeV [Abel and Thorne, 1998a,b, Meredith et al., 2007, 2009, Ni et al., 2013, Thorne et al., 2013].

1.3 Lightning

Lightning strokes are spark discharges formed due to charging of thunderstorm clouds. Although the detailed mechanism of their generation is still not completely understood, there is a basic generally accepted idea. Rubbing of ice particles and water droplets effectively produces electric charge [Rakov and Uman, 2003]. This charge is then separated by gravitational forces resulting in a dipole structure inside the cloud with the positive charge concentrated in the upper part. Unfortunately, this scheme cannot explain all the observed phenomena, especially positive cloud-to-ground discharges. This can be overcome by a tripole model introduced by Williams [1989], who has emphasized the importance of the additional bottom positive pole for lightning initiation. More recent studies have, however, shown that the charge structure inside the thunder clouds is much more complicated, containing at least six charge centers [e.g., Coleman et al., 2008].

Lightning plays an important role in the global electrical circuit described, e.g., by Rycroft et al. [2000]. Schematic drawing of the global circuit is shown in Figure 1.6. Thunderstorm activity charges the ionosphere positively compared to the ground. Due to a good electric conductivity of both the ionosphere and the ground, the charge is spread all around the globe. At the times of fair weather, the "Earth–ionosphere capacitor" gets discharged by current densities of the order of 10^{-12} A/m^2 [Rycroft et al., 2012].

Apart from their role in the global electrical circuit, lightning strokes produce short bursts of electromagnetic emissions in a wide range of frequencies. Most of the power of an average lightning generated emission spreads between about 2 and 10 kHz, peaking between about 5 and 6 kHz [Price and Blum, 1998]. The generated electromagnetic waves can then propagate in the Earth–ionosphere waveguide over rather large distances, and, eventually, escape into the ionosphere.

Climatology studies show that the lightning occurrence rates vary with many parameters. Majority of the observed lightning occurs over or close to the landmass. On the other hand, the strokes detected over the oceans carry substantially larger electric currents, and therefore more energy per stroke [Hutchins et al., 2013a]. One can also identify seasonal and diurnal variance of the lightning occurrence rates. Generally, more lightning would be expected during the local summer. As for the diurnal dependence, lightning occurrence peaks in late afternoon. Figures 1.7a,b show respectively the discussed dependences [Colman and Starks, 2013].

Lightning-generated emissions that escape from the Earth–ionosphere waveguide and propagate to larger radial distances may significantly influence the processes in the Earth's magnetosphere. Lightning whistlers are usually observed

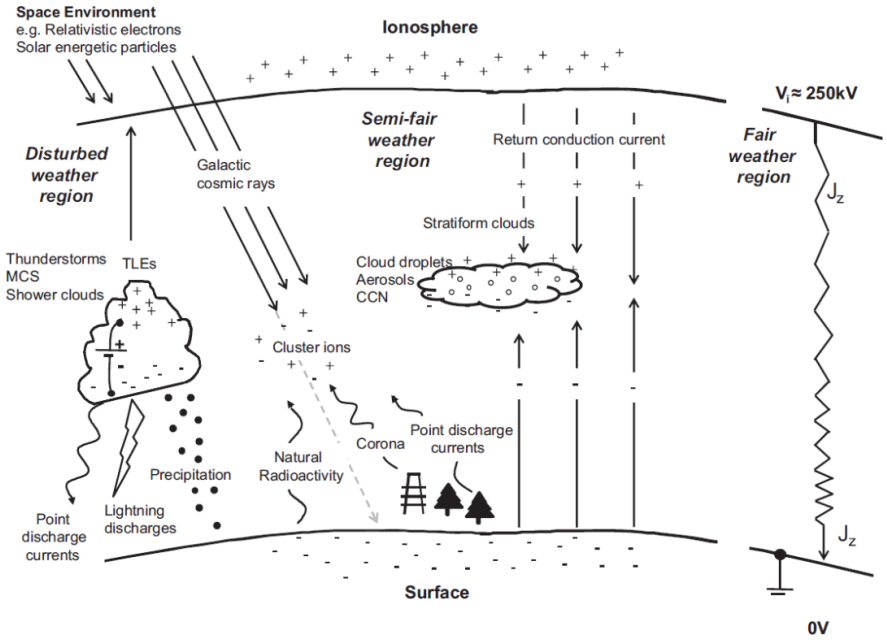

Figure 1.6: Schematic view of the global electric circuit. Reprinted from Rycroft et al. [2012].

only inside the plasmasphere and in the plasmaspheric plumes [Summers et al., 2008], whereas outside the dense plasma region, lightning-generated whistlers are detected rather rarely [Bell et al., 2004, Platino et al., 2005]. Green et al. [2005] suggested that lightning might be one of the embryonic sources for the plasmaspheric hiss. Specifically, they demonstrated that the dependence of the electromagnetic wave intensity measured by the DE 1 spacecraft exhibits a considerable longitudinal dependence on the geomagnetic longitude. At frequency of about 3 kHz, the wave intensity is larger at longitudes corresponding to landmass, and they stated that the longitudinal dependence is eventually identifiable at frequencies as low as about 500 Hz. However, this frequency range was questioned by several following studies [Thorne et al., 2006, Green et al., 2006, Meredith et al., 2006]. Namely, Meredith et al. [2006] used measurements of the CRRES satellite to show that the wave intensity dependence spatially corresponding to the lightning activity can be observed only for waves at frequencies larger than about 2 kHz.

1.4 Earth-Ionosphere Waveguide

The cavity between the bottom layer of ionosphere and the Earth's surface effectively works as electromagnetic waveguide that allows electromagnetic waves to propagate over thousands km with a rather low attenuation [Cummer, 2000]. The propagating waves can be either generated directly inside the cavity, e.g., lightning emissions [Dowden et al., 2008, Fišer et al., 2010] or VLF transmitter signals [Clilverd et al., 2002, Němec et al., 2017], or they can enter the waveguide while propagating from larger radial distances, e.g., quasi-periodic emissions observed by the ground-based stations [Manninen et al., 2013]. Detailed wave propagation properties in the Earth-Ionosphere waveguide are subject to numerous effects such

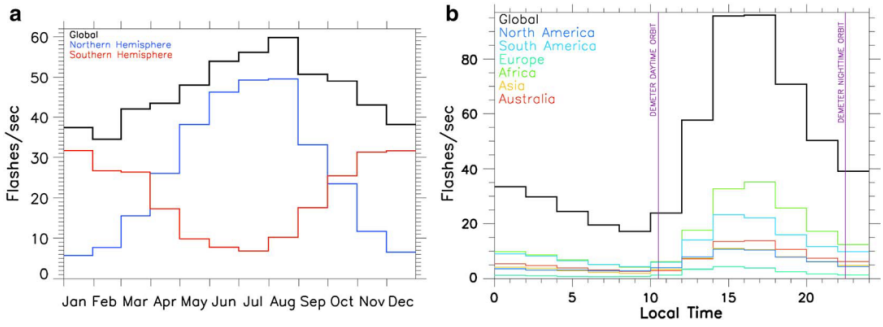

Figure 1.7: a) Seasonal dependence of global average lightning occurrence rates observed by the LIS/OTD missions. Individual lines show the result for the northern (blue) and southern (red) hemisphere, and the global average (black). b) Dependence of average lightning occurrence rates measured by the LIS/OTD missions on the local time. The black line represents the global average, whereas the other colors show the averages for individual continents. Reprinted from Colman and Starks [2013].

as the Earth's magnetic field and curvature, changes of the ionospheric plasma density, various reflection heights of waves with different frequencies, etc. To calculate the wave propagation precisely, one has to know or assume the exact conditions and numerical modeling codes have to be used. Hereinafter, we introduce the basic waveguide mode theory, which is sufficient for our purpose, as it allows to adequately understand some of the properties of the events discussed in Chapter 5.

In the case of lightning-generated emissions, the propagation of transverse magnetic (TM) mode is dominant [Budden, 1961]. In this mode, the magnetic field vector of the wave is perpendicular to the plane given by the wave vectors before and after the reflection from the boundary. We assume a simple scheme of a waveguide formed by two infinite parallel planes at a distance h. For the sake of simplicity, let's use a coordinate system where the planes are parallel to the plane (x, y). Further, one of the planes is located at $z = 0$ and the other at $z = h$. Without loss of generality, we can assume that the initial wave vector is in the plane (x, z), directed obliquely in the negative sense of z-axis and the positive sense of x-axis (see Figure 1.8).

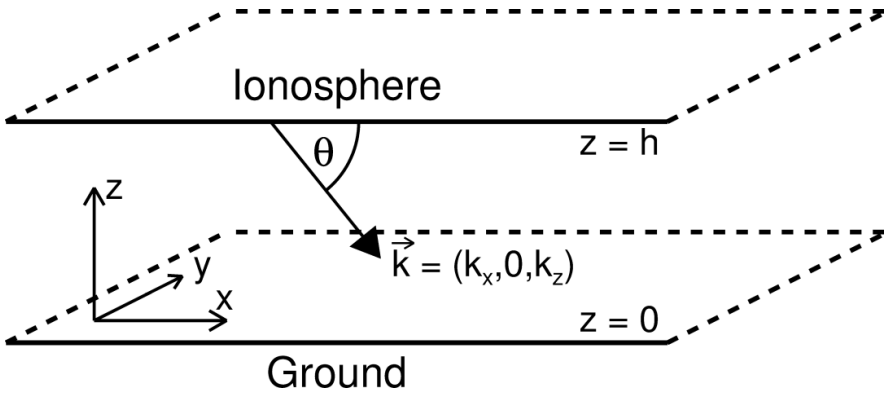

Figure 1.8: Schematic drawing of the simplified waveguide geometry.

Considering the aforementioned situation, the wave vector $\vec{k}$ and electric $\left(\vec{E}\right)$ and magnetic $\left(\vec{H}\right)$ intensity vectors can be written as:

$$\begin{aligned} \vec{k} &= (k_x, 0, k_z), \\ \vec{E} &= (E_x, 0, E_z), \\ \vec{H} &= (0, H_y, 0), \end{aligned} \tag{1.21}$$

and their component values subject to the following equations:

$$\begin{aligned} E_x(x,z,t) &= E_0 \sin\theta \exp\{-ik(x\cos\theta - z\sin\theta)\} e^{i\omega t}, \\ E_z(x,z,t) &= E_0 \cos\theta \exp\{-ik(x\cos\theta - z\sin\theta)\} e^{i\omega t}, \\ H_y(x,z,t) &= H_0 \exp\{-ik(x\cos\theta - z\sin\theta)\} e^{i\omega t}, \end{aligned} \tag{1.22}$$

where k is the absolute value of $\vec{k}$, θ is the acute angle between the wave vector $\vec{k}$ and the $x-$axis, and ω is the angular frequency of the wave. For the following steps, we abandon the time evolution, as it is strictly periodic and independent of spatial parameters.

Assuming a perfect conductivity of both boundaries and summing the initial and reflected waves, one obtains:

$$\begin{aligned} E_x(x,z) &= 2iE_0 \sin\theta \sin(kz\sin\theta) e^{-ikx\cos\theta}, \\ E_z(x,z) &= 2E_0 \cos\theta \cos(kz\sin\theta) e^{-ikx\cos\theta}, \\ H_y(x,z) &= -2H_0 \cos(kz\sin\theta) e^{-ikx\cos\theta}. \end{aligned} \tag{1.23}$$

This set of equations suffices the boundary condition at $z = 0$, namely $E_x(x,0) \equiv 0$. This should be true also for $E(x,h)$, as there is another perfectly conducting layer on the other side of the waveguide. This bounds the wave vector length and direction by equation

$$kh\sin\theta = n\pi, \tag{1.24}$$

where $n \in \mathbb{N}$ is the waveguide mode number. Given that $k = 2\pi/\lambda$ and $\lambda = c/f$, where λ is the wavelength, f stands for the wave frequency and c is the speed of light, one can rewrite equation (1.24) as

$$\sin\theta = \frac{nc}{2h}\frac{1}{f}. \tag{1.25}$$

This gives a minimal frequency for a given mode, the "critical frequency":

$$f_n = \frac{nc}{2h}. \tag{1.26}$$

For frequencies above the critical frequency, $\sin\theta < 1$ and the modes are "propagated". Otherwise, the absolute value of the $\sin\theta$ is larger than one, which means that θ has also an imaginary part. This correspondingly transforms the propagation parts of the equations (1.23), specifically,

$$-ikx\cos\theta = -ikx\left(\pm\sqrt{1-\sin^2\theta}\right) = \mp kx\sqrt{\sin^2\theta - 1}. \tag{1.27}$$

This results in an exponential attenuation of the waves with increasing distance from the source. The "evanescent" modes are thus attenuated by a factor of $\exp(-kx\beta)$ where β is a positive real number given by

$$\beta = \left\{ \left(\frac{nc}{2fh} \right)^2 - 1 \right\}^{\frac{1}{2}} . \tag{1.28}$$

Dimension of the Earth–ionosphere waveguide varies depending on the actual altitude of the bottom layer of the ionosphere. This is located at approximately 70 km during the day and about 90 km during the night [e.g., Watt and Croghan, 1964]. For more precise values, we refer to Toledo-Redondo et al. [2012], who performed a study focused on the temporal and spatial variations of the first cut-off frequency of the Earth–ionosphere waveguide.

As mentioned above, many additional effects influence the real wave propagation. Among those, magnetic field effect and the resulting west-east asymmetry of the wave attenuation is particularly important for our analysis. Crombie [1961] showed that the coefficients of reflection from the bottom layer of the ionosphere are larger for the west-to-east than for the east-to-west propagation. This result is further supported by more recent modeling work of Jacobson et al. [2012]. Experimental evaluation of the attenuation factors performed using the World Wide Lightning Location Network data by Hutchins et al. [2013b] shows that the average attenuation coefficients for the eastward propagation over the water are 1.13 ± 0.35 dB/Mm and 0.71 ± 0.68 dB/Mm for day and night, respectively. Similar calculation for westward propagation gives average attenuation of 2.98 ± 0.68 dB/Mm and 2.66 ± 0.39 dB/Mm for day and night, respectively.

2. Aims of the Thesis

As summarized in the previous chapter, investigation of lightning and its effects on the Earth's magnetosphere still leaves plenty of questions without clear answers. Additionally, recent spacecraft missions bring more precise or completely new measurements of various electromagnetic wave phenomena taking place in the Earth's magnetosphere. Many of them are of unknown origin and might be possibly due to the terrestrial activity.

This thesis contains two main research chapters, one focuses on the effects of lightning emissions on the overall wave intensity in general, and the other studies two kinds of special wave events that are most probably linked to the lightning activity.

We follow up on the previous studies as those of Green et al. [2005], Němec et al. [2010] or Colman and Starks [2013] and perform two statistical studies in order to estimate the lightning contribution to the overall wave intensity.

First we use the neural network for whistler detection onboard the DEMETER spacecraft in order to sort electromagnetic wave measurements according to the momentary lightning activity. This allows us to compare the overall wave power with and without the lightning contribution. Additionally, we compare this study at frequencies below 1.25 kHz with the wave propagation direction analysis. Based on the prevailing wave propagation direction, we can determine whether the measured wave power is dominated by the waves coming from larger radial distances or from the atmospheric processes.

Second, we take advantage of the spatial dependence of lightning occurrence, specifically, the land/ocean imbalance. Fortunately, this can be well simplified to dependence of lightning occurrence on geomagnetic longitude. As the co-rotation effect is negligible in most of the magnetosphere, we can assume that waves of non-terrestrial origin should not depend on the Earth's rotation. Any longitudinal dependence of the measured electromagnetic waves should be thus due to the terrestrial sources. Considering the frequency range of interest, lightning is the most convenient source of such waves.

The other focus of this thesis is on two kinds of special wave events observed by the DEMETER spacecraft. They both consist of alternating frequency bands of enhanced and reduced wave intensity. However, one can be observed at frequencies below about 1 kHz, whereas the other reach up to about 20 kHz with accordingly different band widths. Parameters of individual events are studied, e.g., their minimal and maximal frequencies or spatial and temporal dependence of their occurrence. For both event types we suggest possible mechanisms of their formation.

3. Data Sets

In the studies presented in this thesis, we rely on electromagnetic wave measurements of two spacecraft missions, namely, Detection of Electro-Magnetic Emissions Transmitted from Earthquake Regions (DEMETER) and Radiation Belt Storm Probes (RBSP), later renamed to the Van Allen Probes, honoring the discoverer of the radiation belts, James Van Allen. The lightning data were obtained by the spacecraft missions Lightning Imaging Sensor (LIS) / Optical Transient Detector (OTD) and by a ground-based World Wide Lightning Location Network (WWLLN).

3.1 DEMETER Spacecraft

The French Micro-satellite DEMETER operated between July 2004 and December 2010 on a nearly circular orbit with a high inclination. The original orbiting altitude of about 710 km was decreased to about 660 km in December 2005. The orbit was quasi-Sun-synchronized, resulting in the measurements being performed in two distinct magnetic local time (MLT) intervals centered at about 10:30 and 22:30 MLT. The exact MLT distribution of the DEMETER measurements is shown in Figure 3.1.

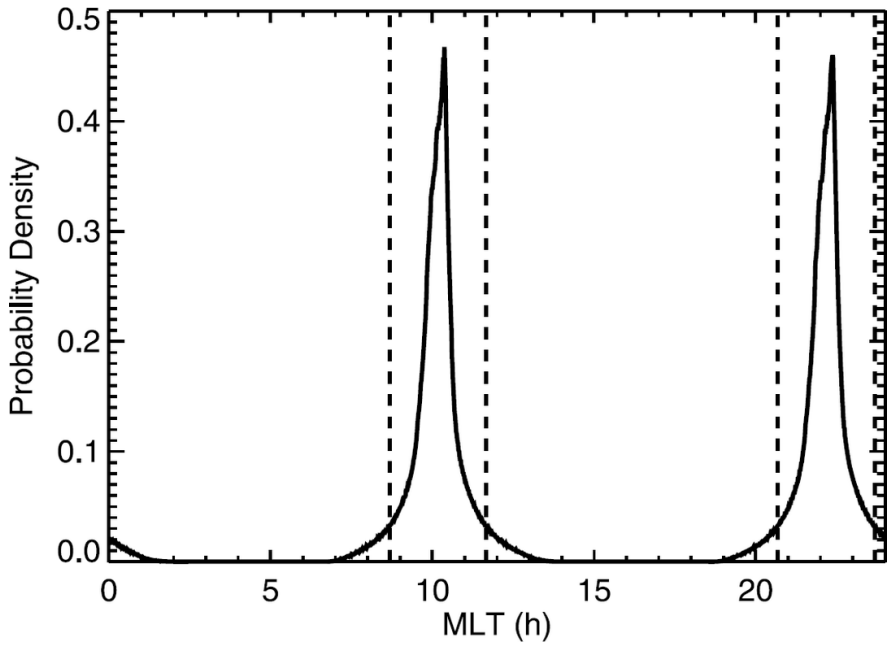

Figure 3.1: Magnetic local time distribution of measurement times of the DEMETER spacecraft. Adapted from Němec et al. [2010].

Most of the time, the spacecraft operated in a Survey mode with a reduced data transfer. This mode was active nearly continuously at geomagnetic latitudes lower than 65°. In selected areas of special interest, a Burst mode was active, i.e., more detailed measurements were performed and better resolution data were transferred to the ground. Figure 3.2 shows geomagnetic maps of the total measurement duration in individual $1° \times 1°$ bins color coded according to

the color scale on the right. Figures 3.2a and 3.2b respectively correspond to the Survey and Burst modes. The histograms on the left show the measurement times summed over geomagnetic longitude.

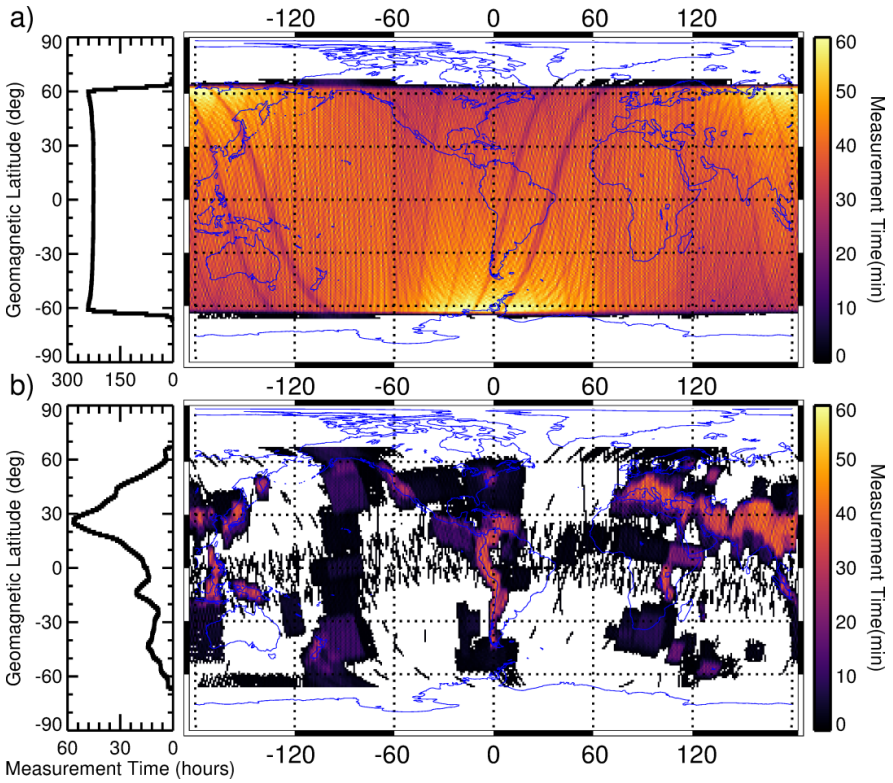

Figure 3.2: Geomagnetic maps of the DEMETER spacecraft measurement time in the (a) Survey and (b) Burst modes in individual $1^\circ \times 1^\circ$ bins. The histograms on the left represent the total measurement times as functions of geomagnetic latitude with resolution of 1 degree.

The instrumentation of the spacecraft consisted of

- Electric Field Instrument (ICE),
- Magnetic Search Coil Instrument (IMSC),
- Neural network for whistler detection (RNF),
- Plasma Analyzer Instrument (IAP),
- Instrument for Particle Detection (IDP),
- Langmuir Probe (ISL).

Out of these, we use the electric [Berthelier et al., 2006] and magnetic [Parrot et al., 2006] field measurements and the neural network for whistler detection [Elie et al., 1999].

3.1.1 ICE Instrument

The electric field measurements were performed in four frequency intervals ranging from the lowest frequencies up to about 3 MHz. In the thesis the Very Low Frequency range up to 20 kHz and the Extremely Low Frequency range up to 1.25 kHz are used.

VLF range

The Very Low Frequency range was active nearly continuously both in the Survey and the Burst mode. One component of electric field was measured and it is available in the form of frequency-time spectrograms with the time resolution of about 2.048 s and the frequency resolution of about 19.53 Hz. Additionally, in the Burst mode, also the waveforms sampled at 40 kHz were stored and transmitted to the ground.

ELF range

The Extremely Low Frequency range was active only in the Burst mode. However, at that moments, all three components of electric field were measured and their waveforms are available with a sampling rate of 2.5 kHz.

3.1.2 IMSC Instrument

Three axis search-coil magnetometer measured magnetic field fluctuations in the VLF and ELF ranges with the parameters corresponding to the electric field instrument. All 6 components of electromagnetic vector were thus recorded in the Burst mode with a sampling rate of 2.5 kHz. Such measurements allow for estimation of additional wave propagation parameters. Wave analysis methods described by Santolík and Parrot [1998, 1999], Santolík et al. [2003, 2006b, 2010] can be used to determine, e.g., the wave and Poynting vectors' directions and wave polarization.

3.1.3 RNF

Due to the limited time resolution of the Survey mode data transmitted to the ground, lightning-generated whistlers can be effectively identified only in Burst mode spectrograms. In order to have information about individual lightning generated whistlers also at the times of inactive Burst mode, onboard implemented neural network automatically inspected frequency-time spectrograms with better time resolution in the frequency range between 3 and 14 kHz for patterns corresponding to the lightning-generated whistlers and sorted them into 19 dispersion classes with the time resolution of about 0.1024 s [Elie et al., 1999]. Neural network used 10×11 matrix of spectral coefficients as an input. On the output side, single neuron indicated whether whistler was identified. In between, two hidden layers processed the input. Using spectrograms of 3 different time resolutions and 4 combinations of frequency bands, the resulting slope of whistler pattern could be modified, which enabled the 19 dispersion classes spanning from 0 $s^{1/2}$ to 300 $s^{1/2}$ to be distinguished with error of 10 % [Parrot et al., 2019]. The network

training was performed using back-propagation algorithm with set of 2500 input patterns and it was afterwards tested on additional 1500 ones. The resulting 91% success rate should be sufficient for statistical studies.

3.2 Van Allen Probes

The Van Allen Probes mission consists of a couple of identical spacecraft that operate since August 2012 on nearly similar highly elliptical orbits close to the equatorial plane. Their orbits with the perigee altitudes of about 600 km and the apogee altitudes of about 32000 km slightly precess so that all combinations of radial distances and local times are covered approximately every two years. The scientific payload consists of

- Energetic particle composition and thermal plasma suite (ECT) containing
  - Helium-oxygen-proton-electron spectrometer (HOPE)
  - Relativistic electron proton telescope (REPT)
  - Magnetic Electron Ion Spectrometer (MagEIS)
- Electric field and waves (EFW)
- Radiation belt proton spectrometer (RPS)
- RBSP ion composition experiment (RBSPICE)
- Electric and magnetic field instrument and integrated science suite (EMFISIS)

In this thesis, we focus on the EMFISIS suite [Kletzing et al., 2013] and on the plasma number density data [Kurth et al., 2015] derived from the high frequency EFW measurements. Figure 3.3 shows an example measurement of the Van Allen Probe A obtained on 15 September 2012 between about 04:10 and 10:50 UT. Individual panels show from top to bottom the color-coded frequency-time spectrogram of power spectral density of magnetic field fluctuations, MLT and L-shell of the spacecraft, and the plasma number density derived from the upper hybrid frequency evaluated using electric field measurements. The red and blue colors in the bottom three panels show where the spacecraft was considered to be inside or outside the plasmasphere, respectively.

3.2.1 EMFISIS

The EMFISIS suite contains tri-axial fluxgate and magnetic search coil magnetometers for magnetic field measurements from DC up to 12 kHz. They are placed on holders about 4 meters from the center of the spacecraft in the spacecraft spin plane. Additionally, the Waves instrument receives the electric field data obtained by the EFW instrument. We use the data obtained by the suite in the nearly continuously active Survey mode. In this mode, all six components of electromagnetic field were measured and average spectral matrices of 0.5 s snapshots are available every 6 seconds. The frequency range from 2 Hz up to 12 kHz is covered

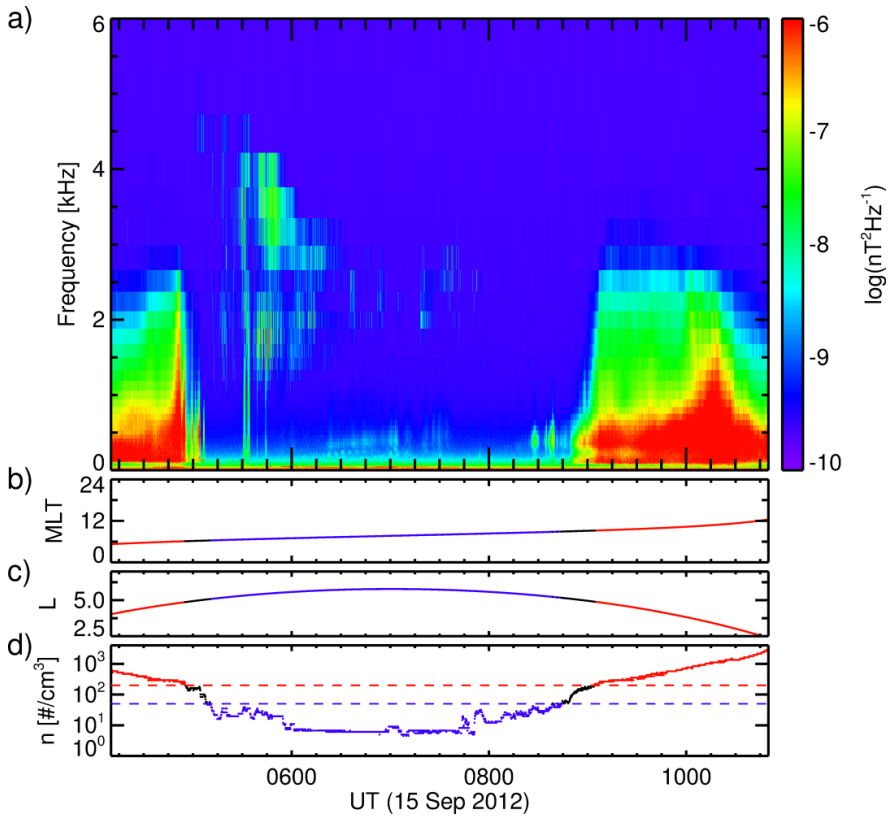

Figure 3.3: (a) Color-coded frequency-time power spectrogram of magnetic field fluctuations measured by the Van Allen Probe A on 15 September 2012 from about 04:10 to 10:50 UT. (b,c) MLT and L-shell of the spacecraft. (d) Plasma number density derived from the upper hybrid frequency estimations. The red and blue colors in panels (b–d) show whether the spacecraft was considered to be inside or outside the plasmasphere, respectively. Reprinted from Záhlava et al. [2018b].

by 65 approximately logarithmically distributed frequency channels. Similarly as described above in section 3.1.2, the performed multicomponent measurements allow for estimation of wave propagation parameters.

3.2.2 Plasma number density

The EFW instrument also provides a single component electric field measurements in the frequency range up to about 500 kHz. This can be used to identify the upper hybrid frequency. The Automated Upper-hybrid Resonance detection Algorithm (AURA) has been developed to search the frequency-time spectrograms for banded emissions that are expected around the upper hybrid resonant frequency.

Having estimated the upper hybrid resonant frequency (f_{uh}) and measuring the ambient magnetic field magnitude, ergo the local electron gyrofrequency (Ω_e), one can derive the local plasma number density (n_e). The upper hybrid resonance is given by equation $f_{uh}^2 = \Omega_e^2 + \Pi_e^2$. We therefore get the expression for the plasma

number density [Kurth et al., 2015]:

$$n_e \left[\mathrm{cm}^{-3}\right] = \left(\frac{\Pi_e \left[\mathrm{Hz}\right]}{8980}\right)^2 = \frac{(f_{uh}^2 - \Omega_e^2)\left[\mathrm{Hz}^2\right]}{8980^2}. \tag{3.1}$$

The largest density detectable by this method, given the frequency range available, is about 2000 cm^{-3}. We use the plasma number density to define whether the measurements were performed inside or outside the plasmasphere. Specifically, we define "inside the plasmasphere" as $L \leq 2.5$ or $n > 200$ cm^{-3}. Similarly, "outside the plasmasphere" is defined as $L > 2.5$ and $n < 50$ cm^{-3}. Anything that does not fit either of the conditions is not considered neither inside nor outside the plasmasphere and remains unclassified.

3.3 Lightning detection

We use two different lightning data sets. One is provided by the Lightning Imaging Sensor (LIS) / Optical Transient Detector (OTD) mission and it contains the average lightning occurrence rates obtained from the optical observations on spacecraft. The other comes from the ground based World Wide Lightning Location Network (WWLLN) and contains information about individual lightning strokes.

3.3.1 LIS/OTD

Lightning detectors installed onboard spacecraft monitor the atomic oxygen multiplet with the wavelength 777.4 nm. Lightning strokes produce pulses of this spectral line and can be therefore localized by the detector. The spatial resolution of LIS and OTD was about 10 and 5 km, respectively [Cecil et al., 2014]. The precessing low altitude orbits of the carry-on spacecraft along with the wide field of view provided rather good coverage for long term statistical studies. A more detailed description of the detectors and methods used for the data processing can be found in Boccippio et al. [2002] and Christian et al. [2003]. The data set used contains average lightning occurrence rates, total numbers of lightning strokes observed and total measurement duration maps with the spatial resolution of $2.5° \times 2.5°$ in geocentric coordinates and the temporal resolution of 2 hours in local time separately for all 365 individual days of year.

3.3.2 WWLLN

A set of over 70 ground based VLF antennas located all over the world monitor frequency range between about 3 and 18 kHz. Lightning strokes produce strong wide-band emissions. If the appropriate emission pulses are detected by at least 3 different stations, it is possible, based on the times of arrival at individual stations, to estimate the time and location of the source lightning stroke [Dowden et al., 2002]. Additionally, using the pulse powers and a sophisticated modeling of the propagation of VLF waves in the Earth-ionosphere waveguide, one can also derive energy produced by a given discharge. Therefore, WWLLN provides a data set containing locations, times and energies of individual lightning strokes

[Hutchins et al., 2012b]. Unfortunately, it is not possible to place a large amount of antennas homogeneously all over the globe, and therefore the network detection efficiency varies with location. This can be partially solved by the maps of the relative detection efficiency of the network provided in the data set [Hutchins et al., 2012a]. The network, however, gradually evolves and the number of stations used increases during the years. This results in the detection efficiency changing in time. Several studies have been performed in order to evaluate the absolute detection efficiency of the network. Abarca et al. [2010] have shown the comparison between the WWLLN and the National Lightning Detection Network (NLDN) which they considered as "the ground truth". They demonstrated that the detection efficiency of the WWLLN increased from about 3.88 % in years 2006 – 2007 up to about 10.3 % between 2008 – 2009. The follow up work by Rudlosky and Shea [2013] used a comparison with the LIS mission. They showed the detection efficiency increase from about 6 % in 2009 up to about 9.2 % in 2012. The discrepancy between the results obtained can be likely attributed to different areas and validation data sets considered. Another evaluation of the absolute detection efficiency was done by Hutchins et al. [2012a] who compared the global average lightning occurrence rates in years 2010 and 2011 obtained from the WWLLN with the long term global average of about 46 strokes per second estimated from the LIS/OTD observations. The average detection efficiency for the two years was 13.7 % and 13 %, respectively.

4. Lightning Contribution to the Electromagnetic Wave Power in the Magnetosphere

We use two approaches to investigate whether or not and, eventually, to what extent lightning contributes to the overall wave power observed by spacecraft in the Earth's magnetosphere. First, measurements of the DEMETER spacecraft in the ELF and VLF ranges are analyzed with respect to the whistler occurrence detected by the onboard implemented neural network. Second, we use the measurements of the DEMETER and the Van Allen Probes spacecraft to investigate the longitudinal dependence of the wave intensity.

4.1 Whistler Detection Analysis

A basic motivation of this method is to compare the electromagnetic wave intensity observed by the DEMETER spacecraft at the times of various levels of lightning activity. As a proxy for the lightning activity level, we use the data provided by the onboard implemented neural network for whistler detection. Having inspected the occurrence maps of whistlers in individual dispersion classes, whistlers with dispersions less than 10 $s^{1/2}$ were identified as 0+ (fractional hop) whistlers, i.e., coming from below the spacecraft. These constitute for the majority (over 85 %) of all detections. In all the further processing, whistlers with larger dispersions are excluded from the analysis, which significantly simplifies the interpretation of the obtained results.

Figures 4.1 and 4.2 show examples of whistler detection by the neural network. Figures 4.1a and 4.2a show detailed frequency-time spectrograms of power spectral density of electric field fluctuations measured by the ICE instrument in the VLF range. Whistler detections are marked in Figures 4.1b and 4.2b as a function of dispersion class and time. One can identify that the detected whistlers well correspond to the spectrograms. Measurements in the ELF range allow for detailed wave analysis and, therefore, the remaining panels show wave parameters at frequencies below 1250 kHz. Figures 4.1c, 4.2c and 4.1d, 4.2d show extremely low frequency range spectrograms of power spectral density of electric and magnetic field fluctuations, respectively. In order to focus on the observed whistlers, detailed wave propagation parameters are only shown for waves with electric power spectral density larger than 3×10^{-7} $mV^2 \cdot m^{-2} \cdot Hz^{-1}$ and magnetic power spectral density larger than 3×10^{-8} nT^2/Hz. Figures 4.1e and 4.2e show the component of Poynting vector parallel to the ambient magnetic field normalized by its standard deviation [Santolik et al., 2001]. The red color represents propagation parallel to the magnetic field, whereas the blue color stands for antiparallel propagation. In the northern hemisphere, where the data shown were obtained, parallel propagation corresponds to the direction towards the Earth, away from the magnetic equator. Figures 4.1f and 4.2f depict the ellipticity of magnetic field fluctuations ranging from -1 corresponding to the left-handed circular polarization through 0 (linear polarization) up to 1 corresponding to the

right-handed circularly polarized wave. Planarity of magnetic field fluctuations, which indicates the viability of the plain wave approximation used, is plotted in Figures 4.1g and 4.2g. Finally, Figures 4.1h and 4.2h show the wave normal angle with respect to the ambient magnetic field [Santolik et al., 2003]. Altogether, we can see that the detected whistlers propagate in the right-handed polarized whistler mode with a rather high planarity from below the spacecraft towards the magnetic equator with wave normal approximately aligned with the ambient magnetic field. The data used in Figures 4.1 and 4.2 were obtained in a 4.4 s interval starting on 4 October 2010 at 03:29:22.1 UT and a 2 s interval from 7 February 2010, 02:16:57.4 UT, respectively.

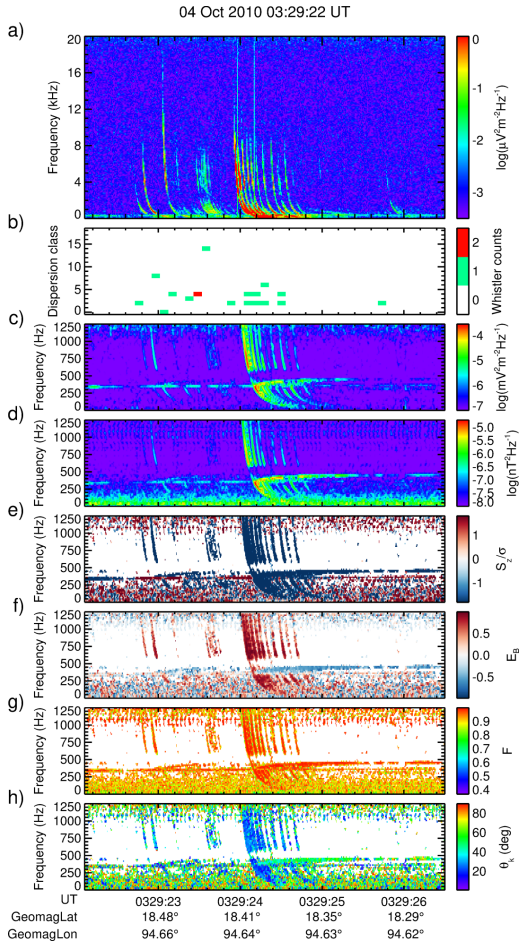

Figure 4.1: (a) Frequency-time spectrogram of power spectral density of electric field fluctuations measured in the VLF range. (b) Number of whistlers detected by the on-board neural network in each dispersion class. (c) Frequency-time spectrogram of electric field fluctuations measured in the ELF range. (d) Frequency-time spectrogram of magnetic field fluctuations measured in the ELF range. (e) Direction of the component of Poynting vector parallel to the ambient magnetic field normalized by its standard deviation. (f) Ellipticity of magnetic field fluctuations. (g) Planarity of magnetic field fluctuations. (h) Wave normal angle with respect to the ambient magnetic field. The measurements took place on 4 October 2010 between 03:29:22.1 UT and 03:29:26.5 UT during the local day. Reprinted from Záhlava et al. [2018a].

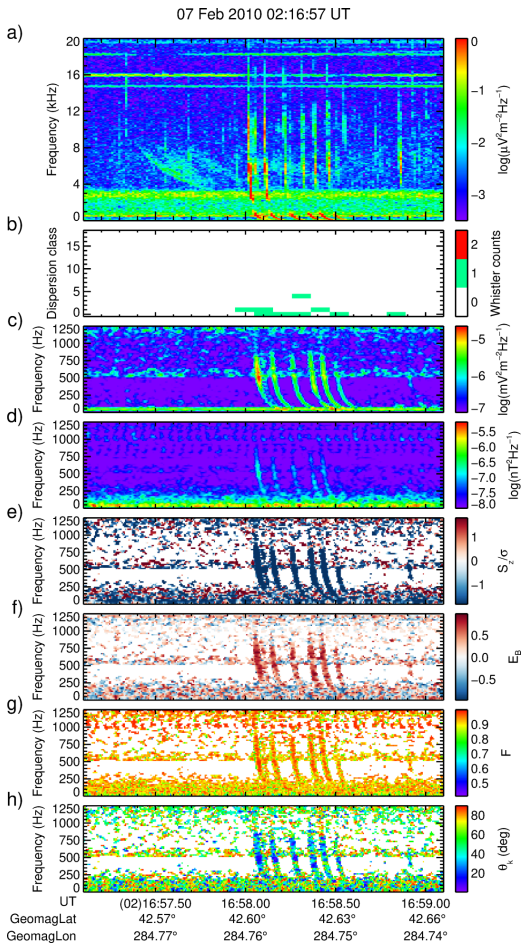

Figure 4.2: Same as Figure 4.1, but the measurements took place on 7 February 2010 from 02:16:57.4 UT to 02:16:59.4 UT corresponding to the local night. Reprinted from Záhlava et al. [2018a].

In this study, we analyze the Survey mode frequency-time spectrograms obtained by the DEMETER spacecraft in the VLF range. These are available with the time resolution of 2.048 s. To each power spectrum, we assigned a whistler occurrence level corresponding to the average occurrence rate of 0+ whistlers detected by the onboard neural network in a given 2.048 s interval. Separately for day- and night-time half-orbits, as well as for individual 1° intervals of the absolute value of geomagnetic latitude, distribution functions of the whistler occurrence rates were constructed and their quartiles are shown as functions of the absolute value of geomagnetic latitude in Figure 4.3. The red and blue colors represent the day- and night-time results, respectively, whereas their shades, as well as different symbols distinguish individual quartiles. For the further analysis, the 0.25 and 0.75 quantiles were selected as threshold values between the low, medium, and high whistler occurrence rate categories. Constructing the distribution functions separately for day and night and individual 1 degree intervals of the absolute value of geomagnetic latitude allows us to properly distinguish the time intervals of unusually high or low whistler occurrence rate in a given location and local time.

Whistler occurrence rates observed during the night are generally significantly higher than those observed during the day. This is due to a combination of sev-

eral causes. First, lightning occurrence at the local times corresponding to the DEMETER measurements is about 60 % higher during the night than during the day [Colman and Starks, 2013] (see Figure 1.7b). Moreover, the ionospheric attenuation is substantially larger during the day than during the night, as the additional D-layer is formed and the ionization is generally larger during the sunlight exposure [Němec et al., 2008, Helliwell, 2014]. The attenuation plays critical role since only whistlers sufficiently stronger than the background can be successfully detected. Especially during the day, there is a clearly identifiable peak of whistler occurrence rate at geomagnetic latitudes of about 50°. The observed whistler occurrence rate decrease towards low latitudes apparently contradicts the lightning occurrence rate being the largest there [Christian et al., 2003]. The lightning occurrence boost is, however, more than countered by the increased ionospheric attenuation near the magnetic equator. This significantly larger attenuation is caused by the inconvenient orientation of the Earth's magnetic field lines, which are nearly parallel to the Earth's surface [Helliwell, 2014]. The whistler occurrence rate drop at latitudes larger than about 50° is probably due to low lightning occurrence rates at high latitudes.

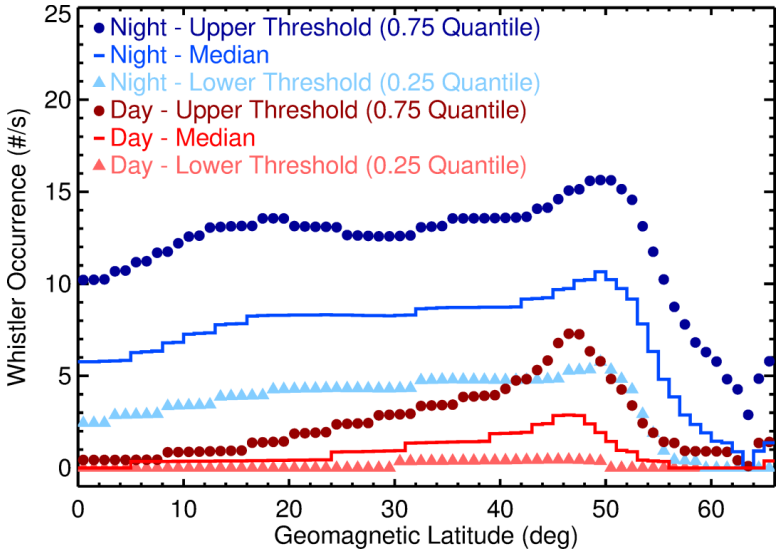

Figure 4.3: Quartiles of whistler occurrence rate as a function of the absolute value of the geomagnetic latitude. The daytime and nighttime values are represented by the red and blue colors, respectively. The 0.75 and 0.25 quantiles are shown by the dots and triangles, respectively. These are then, respectively, used as "high" and "low" whistler occurrence thresholds in the further analysis. Additionally, the solid lines of the respective colors represent the median values. Reprinted from Záhlava et al. [2018a].

The observed whistler occurrence rates are generally higher than the lightning occurrence rates per square km, and even per square degree below the spacecraft. This is consistent with the finding that whistlers can be observed well over 1,000 km from the source lightning [Fišer et al., 2010]. This area might be even larger in the latitudinal direction due to the propagation paths of unducted whistlers [Bortnik et al., 2003].

All electric field power spectra measured by DEMETER were classified according to the whistler occurrence levels at respective times. Figures 4.4a,b show

color coded median power spectral densities at the times of high and low whistler occurrence rates as functions of frequency (ordinate) and the absolute value of geomagnetic latitude (abscissa). The results were obtained for the day-time half-orbits. Figures 4.4c,d show the same for the night-time half-orbits. For the sake of simple comparison, the color scale is the same in all four panels.

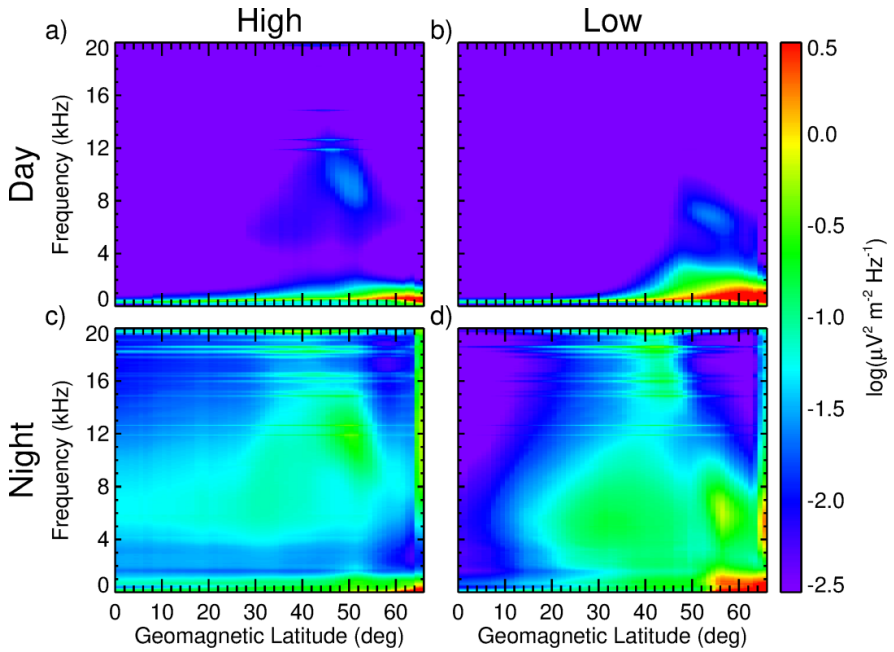

Figure 4.4: Color coded median power spectral density of electric field fluctuations as a function of frequency and the absolute value of geomagnetic latitude. Results were obtained (a) at the times of high whistler occurrence rate during the daytime half-orbits, (b) at the times of low whistler occurrence rate during the daytime half-orbits, (c) at the times of high whistler occurrence rate during the nighttime half-orbits, and (d) at the times of low whistler occurrence rate during the nighttime half-orbits. The horizontal intense lines at frequencies above about 12 kHz observable especially during the night are due to VLF transmitters. Reprinted from Záhlava et al. [2018a].

The results reveal an area of high intensity waves at frequencies below about 1 kHz and geomagnetic latitudes larger than about 45°. The median wave power in this frequency-latitude interval is larger during the day, when it also extends to slightly higher frequencies and lower latitudes. It further apparently increases at the times of low whistler occurrence as compared to the times of high whistler occurrence.

A significant variability of the median power spectral densities in individual cases is further observable at frequencies above about 2 kHz. Generally, the median intensities there are lower during the day than during the night. For better comparison between the times of high and low whistler occurrence, Figures 4.5a,b show day- and night-time ratios between the respective median power spectral densities. The red color corresponds to the median power spectral density of electric field fluctuations being larger at the times of high whistler occurrence rate than at the times of low whistler occurrence rate. The blue color represents the opposite.

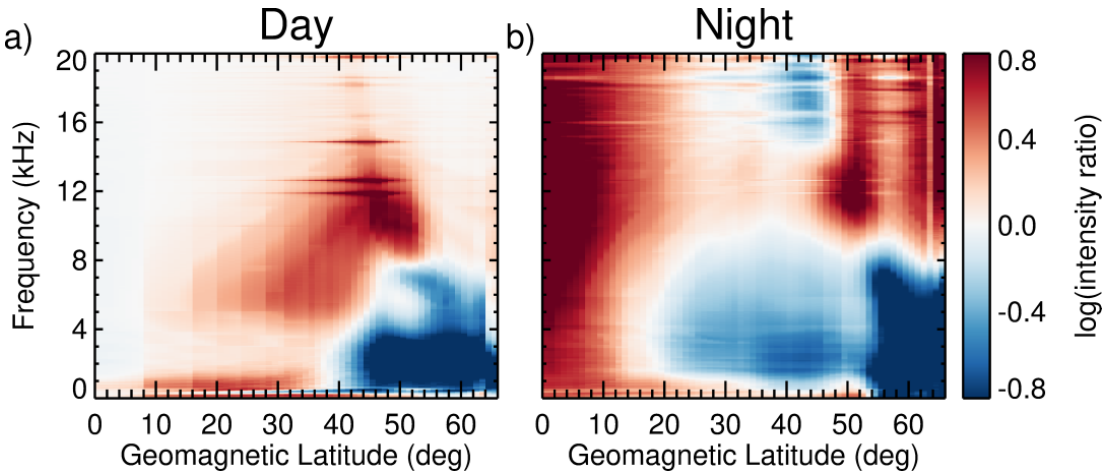

Figure 4.5: Color coded ratio between the median power spectral density of electric field fluctuations during the high and low whistler occurrence rate periods. a) Results obtained using the daytime half-orbits. b) Results obtained using the nighttime half-orbits. The red color corresponds to the situation of larger median wave intensity at the times of "high" whistler occurrence. The blue color corresponds to the frequency-geomagnetic latitude intervals where the median wave intensity is larger at the times of "low" whistler occurrence. The red horizontal lines at frequencies about 12, 15, and 18 kHz observed in particular during the daytime correspond to VLF transmitter signals. Reprinted from Záhlava et al. [2018a].

The red-colored areas indicate the frequency-geomagnetic latitude intervals where the occurrence of lightning-generated whistlers is significantly correlated with the overall wave intensity. This is especially well observable at frequencies between about 4 and 12 kHz and at latitudes between about 20° and 50° during the day and at frequencies above about 10 kHz in the whole range of latitudes during the night. Additionally, the median wave intensity is significantly enhanced in the entire analyzed frequency range at geomagnetic latitudes below about 10° during the night-time half-orbits. The blue areas showing enhanced power spectral density at the times of low whistler occurrence rates can be seen at low frequencies and high latitudes both during the day and night. During the night, two additional blue areas are present. One spans over frequency range between about 1 and 8 kHz and over latitudes larger than about 20°, the other can be seen at frequencies between about 15 and 20 kHz and geomagnetic latitudes between about 40° and 50°.

Unfortunately, the interpretation of these blue areas indicating the anti-correlation between the whistler occurrence and the median power spectral density is not that straightforward. Surely, there exist processes that could explain the negative impact of the whistler presence on the overall wave intensity. For example, lightning-generated whistlers play a non-negligible role in the precipitation of energetic electrons trapped in the Van Allen radiation belts, and these electrons are responsible for generation of whistler mode waves, e.g., chorus [Burton and Holzer, 1974, Katoh and Omura, 2016]. However, it seems more probable that the explanation stems from the varying detection efficiency of the neural network. When the whistler is weak compared to the background, the probability of its

successful detection by the neural network decreases. Consequently, the observed whistler occurrence rate is systematically underestimated at the times of high intensity of other natural emissions.

The dark red horizontal lines well observable in Figure 4.5a correspond to the frequencies of Russian Alpha Navigation transmitters. This might suggest either malfunction of the detection network due to the transmitter signal pattern, enhanced whistler observability at the times of stronger detected VLF transmitter signals, or higher whistler occurrence rates in the corresponding locations.

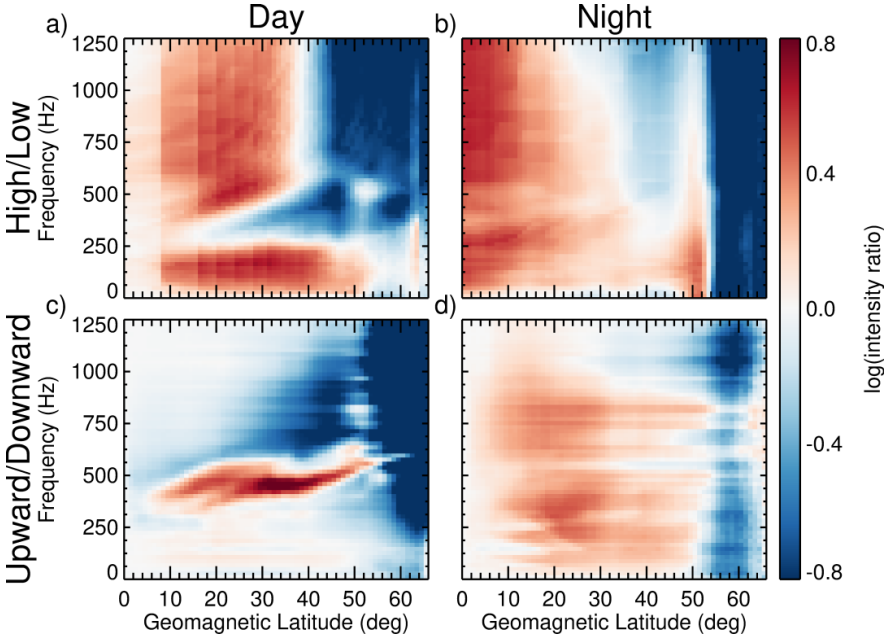

Figure 4.6: (a) Extremely low frequency part of Figure 4.5a (daytime). (b) Extremely low frequency part of Figure 4.5b (nighttime). (c), (d) Color coded ratio between the median power spectral density of electric field fluctuations of the waves propagating predominantly away from the Earth and those propagating predominantly towards the Earth. The results were obtained using the daytime (c) and nighttime (d) half-orbits. The red color corresponds to the frequency-geomagnetic latitude intervals where the median wave intensity is larger for the upward propagation. Reprinted from Záhlava et al. [2018a].

In the ELF range, all six components of electromagnetic vector were measured in the Burst mode, and it is thus possible to determine additional wave propagation parameters. Among others, the Poynting vector component parallel to the ambient magnetic field carries a significant piece of information for our study. Based on its sign, we can determine whether the waves come to the spacecraft from the Earth or from larger radial distances. This can be effectively used to classify the measurements to those with and without dominant terrestrial contribution. Figures 4.6a,b show the ELF parts of Figures 4.5a,b, respectively. Nearly the whole ELF range is dominated by lightning at geomagnetic latitudes lower than about 40°, whereas the rest is covered in blue. During the day, there is, however, a blue wedge reaching down to latitudes of about 20° in the frequency range between about 250 and 400 Hz.

For the comparison, Figures 4.6c,d show the respective day- and night-time results obtained using the wave propagation direction analysis. Specifically, they

show the ratio between the median power spectral density of electric field fluctuations propagating primarily upwards, i.e., away from the Earth's surface towards the magnetic equator, and those propagating primarily in the opposite direction. We can identify, especially during the day, that vast areas are covered in white indicating principally no correlation between the median wave intensity and lightning-generated whistlers. During the night, geomagnetic latitudes up to about 50° are dominated by electromagnetic waves propagating from below the spacecraft, presumably lightning-generated whistlers. Up to this point, the results of the two methods are in a rough correspondence. However, during the daytime, there is a discrepancy at frequencies between about 250 and 400 Hz and geomagnetic latitudes from 10° to 50°. The more intense waves seem to propagate from below the spacecraft, however, the whistler analysis suggests that they are not of a lightning origin. A possible explanation of this phenomenon was offered by Santolík and Parrot [1999]. The observed upgoing waves are probably *type F waves* described by them. Such waves originate from hiss or chorus that propagate at high latitudes down to low altitudes where they get reflected towards lower latitudes at the multi-ion cutoff frequency [Santolík et al., 2006b].

To conclude this part: We analyzed the electric field measurements by the DEMETER spacecraft. Based on the number of whistlers detected by the onboard neural network, we compared electromagnetic wave measurements at the times of high and low whistler occurrence. The ratio between the median wave intensity at the times of high and low whistler occurrence revealed the frequency-geomagnetic latitude intervals where the whistler occurrence significantly correlates with the overall wave intensity. The results are, in the ELF range, in agreement with the analysis based on the wave propagation direction. This topic was further investigated by Záhlava et al. [2019], who used the ground based lightning detections by the WWLLN to estimate the contemporary lightning activity for the measurements of the DEMETER and the Van Allen Probes spacecraft. Good correlation between the wave intensity and the lightning occurrence is found in most of the studied frequency–L-shell range, especially in the afternoon-to-night sector.

4.2 Longitudinal Dependence

In this section, we introduce a study that takes advantage of land/ocean imbalance of the lightning occurrence rates in order to investigate the lightning effects on the overall wave intensity in the magnetosphere. Fortunately, this can be well simplified to the dependence of the studied phenomena on the geomagnetic longitude. Following the discussion ignited by Green et al. [2005] and continued by Thorne et al. [2006] and Meredith et al. [2006], we show a detailed analysis of what frequency range is most influenced by the lightning activity.

There is no reason for the electromagnetic waves generated at larger radial distances to directly depend on the geomagnetic longitude, and any longitudinal dependence observed can be thus supposed to be of the terrestrial origin. Altogether, there are four main longitude-dependent sources of electromagnetic waves on the Earth. First, the powerful military VLF transmitters produce electromagnetic emissions carrying hundreds of kilowatts of wave power [Bullough et al., 1975, Gamble et al., 2008, Starks et al., 2008, Foster et al., 2016]. However, such

waves are usually very narrowband and they are emitted at frequencies higher than 10 kHz [Cohen and Inan, 2012], which is above the investigated frequency range. Another source of rather narrow band emissions is the electromagnetic radiation produced by electric power lines [Helliwell et al., 1975, Bell et al., 1982, Němec et al., 2006]. In addition to the narrow band nature of the emissions, they are also rather weak, and thus do not significantly contribute to the overall wave intensity [Němec et al., 2010].

We use the electromagnetic wave measurements performed by the DEMETER and the Van Allen Probes spacecraft and compare the measured intensities with the lightning occurrence rates observed by the LIS/OTD mission. Considering the Van Allen Probes, we further distinguish whether the measurements were performed inside or outside the plasmasphere. "Inside the plasmasphere" corresponds to a situation when $L \leq 2.5$ or $n > 200$ cm^{-3}, where L is the L-shell of the spacecraft and n is the locally evaluated plasma number density. Accordingly, we define "outside the plasmasphere" as $L > 2.5$ and $n < 50$ cm^{-3}. In cases when neither condition is satisfied or the plasma number density is unavailable at $L > 2.5$, the measurements are not included in the study.

Figure 4.7 shows the daytime results. Specifically, Figure 4.7a depicts the median power spectral density of magnetic field fluctuations measured by the Van Allen Probes outside the plasmasphere in the local time interval between 9 and 12 hours as a function of the geomagnetic longitude and frequency. The values are color-coded corresponding to the scale on the right side. Figure 4.7b uses the same representation, but it was obtained for the spacecraft measurements inside the plasmasphere. Figure 4.7c shows the geomagnetic longitude-frequency dependence of the median power spectral density of electric field fluctuations measured by the DEMETER spacecraft during its day-time half-orbits. Finally, for a comparison, Figure 4.7d contains the normalized whistler rate. It was calculated as follows: The provided geographic lightning occurrence maps were recalculated to the geomagnetic coordinates preserving the spatial resolution of 2.5° both in longitude and latitude. Then, an average ionospheric profile was calculated for all combinations of the local time and geomagnetic latitude with the resolution of 2 hours and 2.5°. Specifically, the International Reference Ionosphere (IRI) model [Bilitza and Reinisch, 2008] was used to obtain the profiles with longitudinal resolution of 30° at equinoxes of 1996, 1999, 2002, 2005, 2008. These were averaged and then used as inputs for a full wave propagation calculation algorithm [Bortnik and Bleier, 2004, Nagano et al., 1975, Němec et al., 2008, Tao et al., 2010] to estimate the attenuation of a 2 kHz wave propagating from the altitude of 50 km up to 1,000 km. These estimations of the wave attenuation were then used along with the area lightning rates to calculate the total power of lightning generated whistlers reaching the top of the ionosphere at a given geomagnetic longitude. Finally, the dashed lines show approximate geomagnetic longitudes of the peaks of the normalized whistler rate in the local time interval 8–12 hours. Note that the local time interval chosen for the Van Allen Probes better corresponds to the local time distribution of the DEMETER measurements. Unfortunately, the LIS/OTD data set is provided with 2 hour resolution, and therefore, we had to use a longer local time interval.

The Van Allen Probes observed no longitudinal variation of the median power spectral density both inside and outside the plasmasphere. Overall, the wave

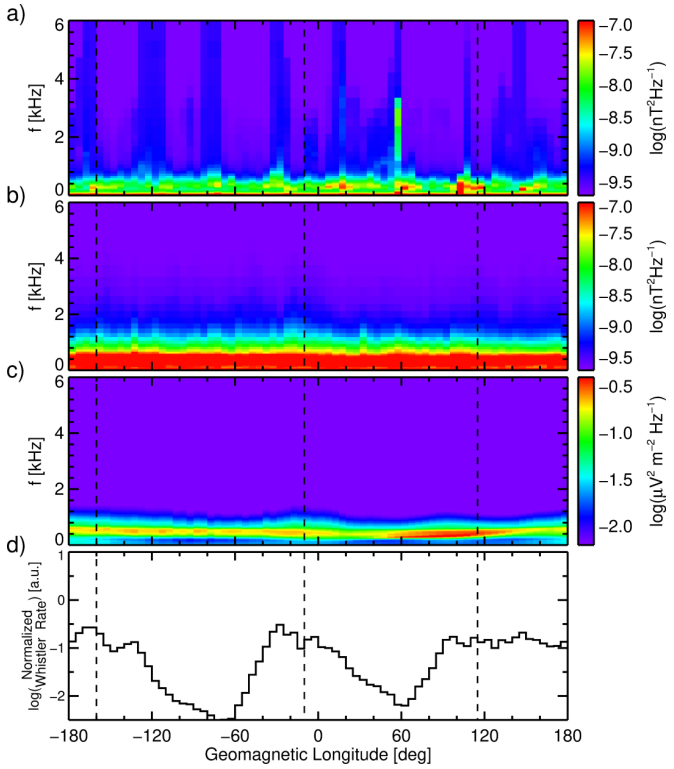

Figure 4.7: a) Median power spectral density of magnetic field fluctuations measured by Van Allen Probes outside the plasmasphere in the MLT interval from 9 to 12 hours as a function of frequency and geomagnetic longitude. b) Same as a), but inside the plasmasphere. c) Median power spectral density of electric field fluctuations measured by the DEMETER spacecraft during the daytime half-orbits as a function of frequency and geomagnetic longitude. d) Average lightning occurrence rate in the local time interval 8-12 hours normalized by the ionospheric attenuation factor as a function of the geomagnetic longitude. The dashed lines mark the longitudinal positions of the largest normalized lightning occurrence rates. Reprinted from Záhlava et al. [2018b].

intensity at frequencies below about 1 kHz is significantly higher inside plasmasphere than that observed outside. In the case of the low altitude DEMETER spacecraft, it is possible to identify a slight variation of the median wave intensity at frequencies of about 1 kHz, but the effect is very weak.

The situation is drastically different during the night. Figures 4.8–4.10 adapt the same format as Figure 4.7, but for the MLT interval between 21 and 24 hours for the Van Allen Probes, night-time half-orbits of DEMETER and the local time interval from 20 to 24 hours for the lightning data. Additionally, the results are calculated separately for three levels of geomagnetic activity. Figures 4.8,4.9, and 4.10 respectively represent the AE index intervals AE $<$ 100, 100 $\leq$ AE $<$ 300, and 300 $\leq$ AE. Qualitatively, all the three Figures show rather similar dependences. The overall wave intensity slightly depends on the geomagnetic activity, being higher at the times of higher geomagnetic activity. Outside the plasmasphere, the results are rather similar to those obtained for the daytime measurements, i.e., no longitudinal dependence is observed. Nevertheless, both the Van Allen Probes inside the plasmasphere and the DEMETER spacecraft

observed three significant maxima at geomagnetic longitudes of about −170°, −15°, and 75°, roughly corresponding to the East Asia, North America and Russia, respectively. Additionally, the latter two peaks are located at geomagnetic longitudes of substantially enhanced normalized whistler rate.

The main difference between the Van Allen Probes and DEMETER is in the frequency extent of the phenomenon. In case of the Van Allen Probes, it can be observed from about 0.5 kHz, and the overall wave intensity decreases significantly above about 3 kHz. The lower boundary of about 0.5 kHz can be observed also in the case of DEMETER, however, there is other longitudinal dependence observable at lower frequencies. Another significant frequency boundary is at about 1.7 kHz, roughly corresponding to the critical frequency of the Earth-ionosphere waveguide, around which the overall wave intensity is reduced. The observed longitudinal dependence of the median power spectral density reaches up to the top frequency used for the plots, i.e., 6 kHz, and extends up to over 10 kHz (not shown).

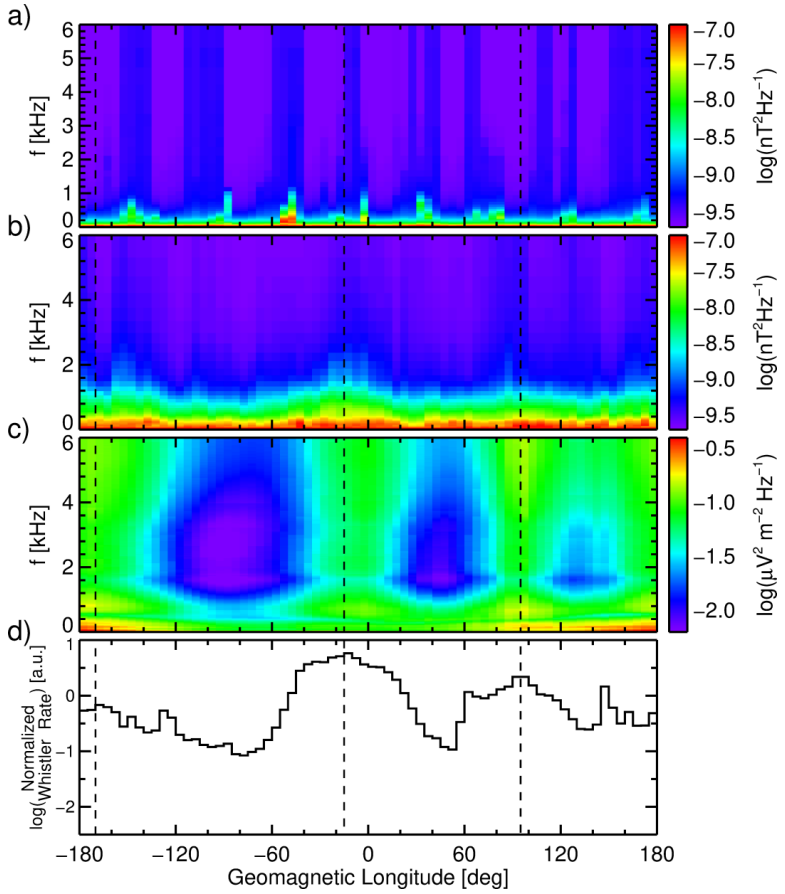

Figure 4.8: Same as Figure 4.7, but for the MLT interval 21-24 hours (panels a,b), nighttime half-orbits (panel c), and for local time interval from 20 to 24 hours (panel d). Only data measured at the times of AE < 100 are used. Reprinted from Záhlava et al. [2018b].

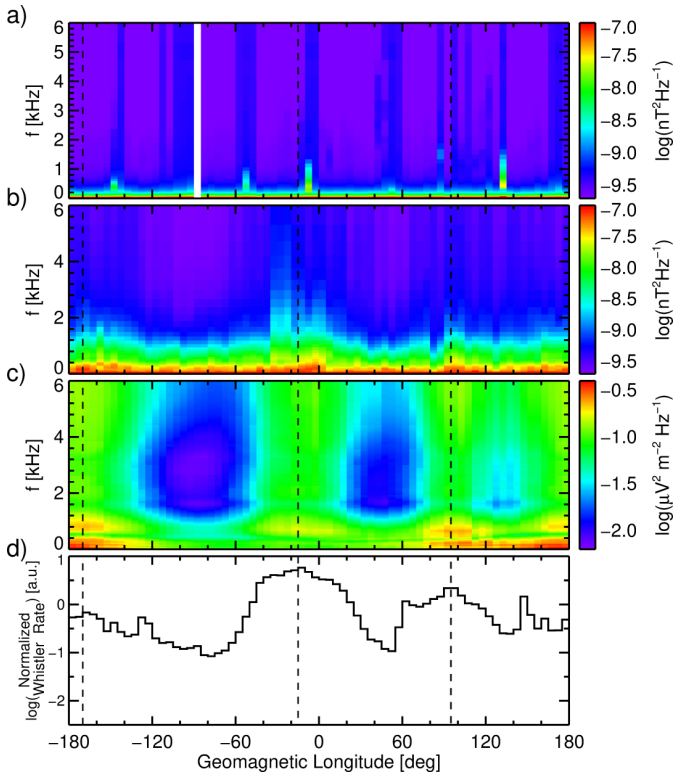

Figure 4.9: Same as Figure 4.8, but only data measured at the times of 100 $\leq$ AE $<$ 300 are used. Reprinted from Záhlava et al. [2018b].

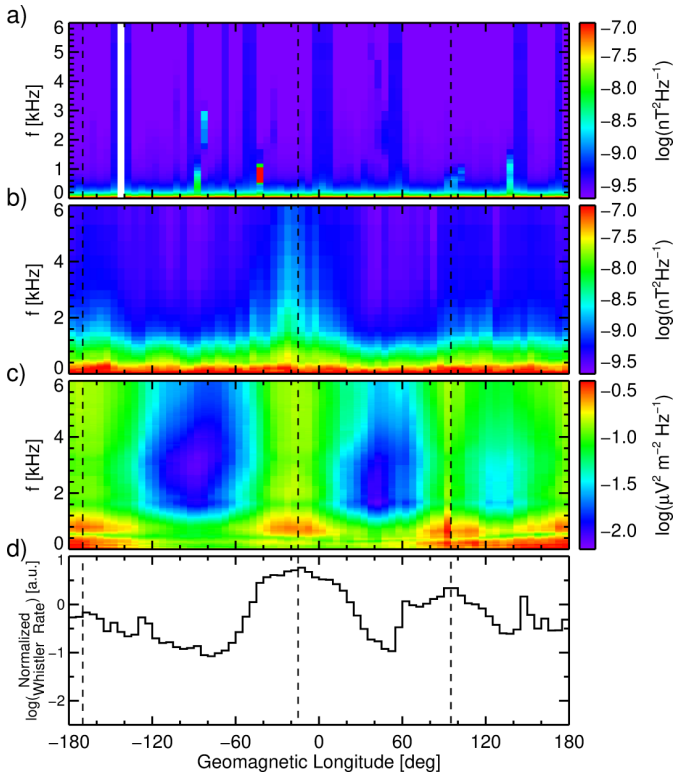

Figure 4.10: Same as Figure 4.8, but only data measured at the times of AE $\geq$ 300 are used. Reprinted from Záhlava et al. [2018b].

The question of the lower frequency limit of the longitudinal dependence was the main topic of the discussion between Green et al. [2005], Thorne et al. [2006], and Meredith et al. [2006]. Using the Van Allen Probes data, we focus on this in detail. Figure 4.11 shows the median power spectral density observed in individual frequency bins between 189 and 595 Hz in the MLT interval from 21 to 24 hours. The values are normalized by the maxima of individual dependences. The dashed lines, again, mark the geomagnetic longitudes of the enhanced normalized whistler rates. As expected, there is no sharp boundary below which the effect would disappear completely. To some extent, even in the frequency bin between 189 and 210 Hz one can identify the intensity peaks. However, they become more noticeable at frequencies above about 400 Hz, where the values of the intensity minima are only about one half of the maximal values.

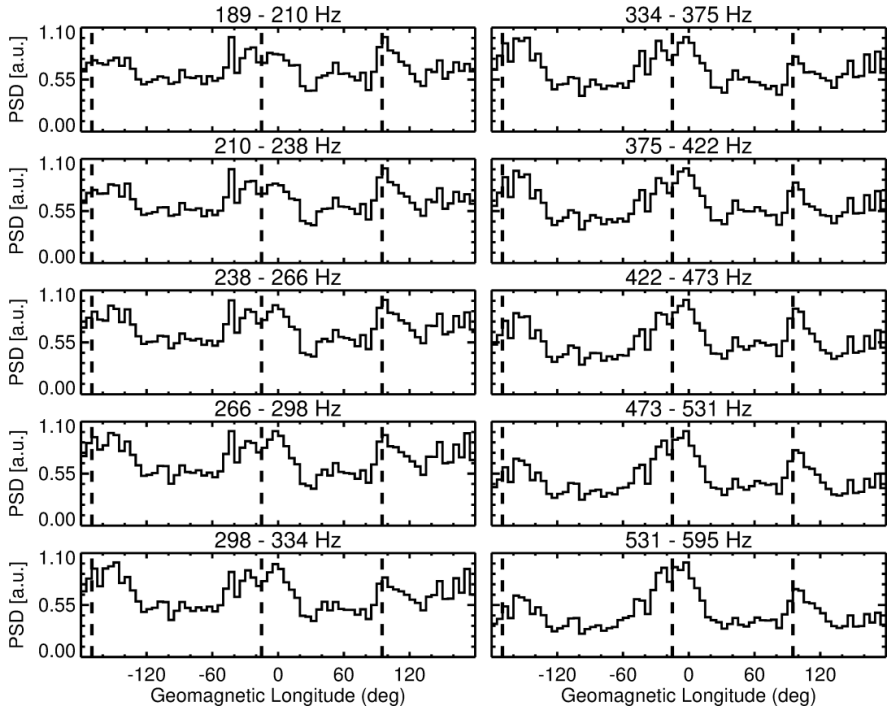

Figure 4.11: Median power spectral density in selected frequency channels measured by the Van Allen Probes inside the plasmasphere in the MLT interval between 21 an 24 hours. Individual dependences are normalized by their respective maxima. The longitudes of the largest normalized lightning occurrences are marked by the dashed lines. Reprinted from Záhlava et al. [2018b].

Further, we split the frequency range covered by the Van Allen Probes into four intervals, for which Figures 4.12a,b show the median power spectral density normalized by the respective maxima in the MLT intervals between 9 and 12 hours and from 21 to 24 hours, respectively. The lowest frequencies up to about 400 Hz are represented by the blue color. The green and yellow curves show the dependences in the frequency ranges from 400 Hz to 2.1 kHz and from 2.1 kHz to 7.5 kHz, respectively. These two exhibit significant nighttime variation of the median wave intensity with respect to the geomagnetic longitude. It is especially well pronounced in the case of the green one. Finally, the red color shows the normalized median wave power at frequencies larger than about 7.5 kHz.

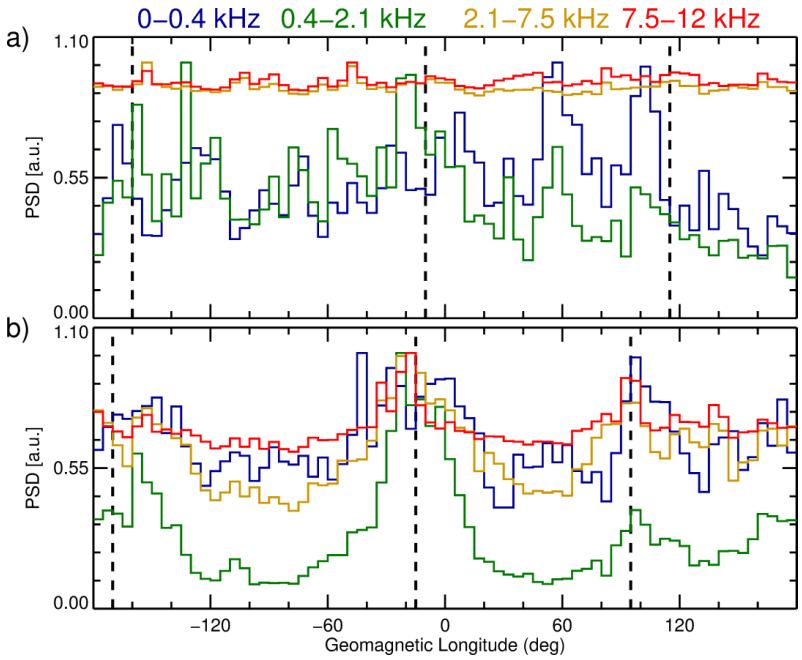

Figure 4.12: a) Longitudinal dependence of median magnetic power spectral density measured by the Van Allen Probes inside the plasmasphere in the MLT interval from 9 to 12 hours. Dependences obtained in individual frequency ranges are normalized by their respective maxima and color-coded according to the legend on the top. The longitudes of the largest normalized lightning occurrences are marked by the dashed lines. b) Same as a) but for the MLT interval between 21 and 24 hours. Reprinted from Záhlava et al. [2018b].

The frequency range between about 2.1 and 7.5 kHz is expected to be the most influenced by the lightning activity as lightning-generated electromagnetic emissions are most intense in this frequency range [Holzworth et al., 1999]. On the other hand, the lightning effect on the frequency range between 0.4 and 2.1 kHz was a merit of discussion. Based on our results, we can confirm the statement of Green et al. [2005] considering the frequency extent of the longitudinal dependence. However, it is not clear whether lightning constitutes for a source of plasmaspheric hiss, or the enhanced wave intensity is directly due to the lightning-generated whistlers.

Unlike DEMETER, the Van Allen Probes orbits cover all combinations of the geomagnetic longitude and the MLT. This allows us to extend the Day/Night distinction and investigate the whole diurnal variation of the longitudinal dependence. Figure 4.13a shows the median power spectral density of magnetic field fluctuations observed by the Van Allen Probes as a function of the MLT (ordinate) and the geomagnetic longitude (abscissa). Considering the most significant longitudinal variation observed, the frequency range between about 0.4 and 2 kHz was used for this plot. The dashed lines, again, mark the approximate locations of the largest nighttime normalized whistler rate. One can clearly identify areas of below average wave intensity at geomagnetic longitudes in between the dashed lines in the MLT interval approximately from 18 to 6 hours. Figure 4.13b is shown to demonstrate the nearly uniform distribution of the number of data points in individual bins.

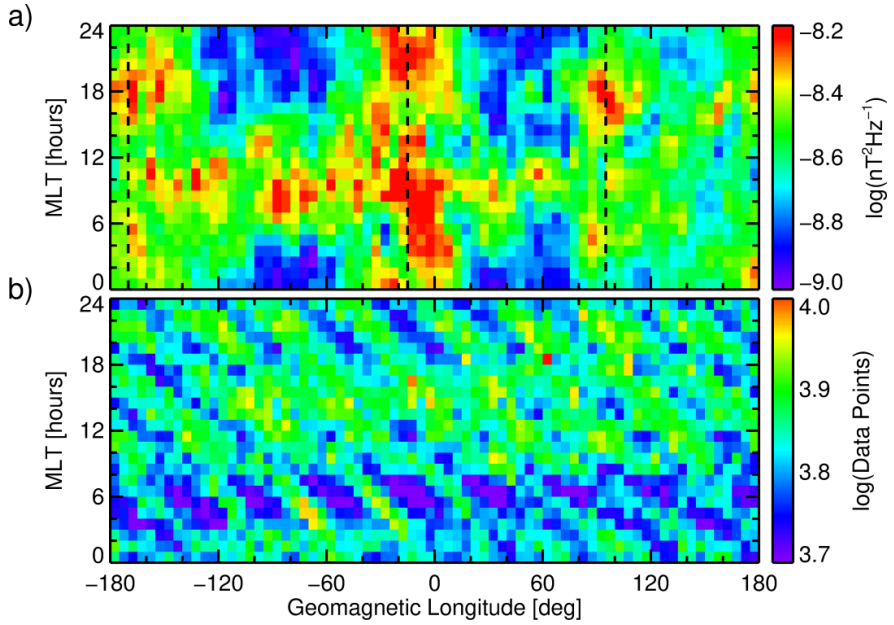

Figure 4.13: a) Median magnetic power spectral density in the frequency range between 0.4 and 2 kHz measured by Van Allen Probes inside the plasmasphere as a function of MLT and geomagnetic longitude. The dashed lines mark the longitudes of the largest normalized lightning occurrence rates. b) Number of data points in individual bins. Reprinted from Záhlava et al. [2018b].

The 6-component measurements of the electromagnetic field vector allow for a detailed analysis of the wave propagation parameters. One of the most important wave properties for the wave-particle interactions is the wave normal angle, i.e., the angle between the wave vector and the ambient magnetic field line. We distinguish quasi-parallel waves with wave normal angles lower than 30° and quasi-perpendicular waves with wave normal angles larger than 60°. The respective median power spectral densities are shown in Figures 4.14a and 4.14b as functions of the MLT and the geomagnetic longitude. For the comparison, Figure 4.14c depicts the normalized whistler rate as a function of the same parameters. The dashed lines, again, mark the peaks as in Figure 4.13. In order to have a reliable wave normal angle estimation, only waves with planarity over 0.5 are considered in Figures 4.14a,b. The quasi-parallel waves exhibit significantly larger median power spectral density compared to the quasi-perpendicular waves. However, they do not exhibit any longitudinal dependence. On the other hand, the behavior of median power spectral density of the quasi-perpendicular waves well corresponds to that of the normalized whistler rate shown in Figure 4.14c. At geomagnetic longitudes between about −40° and 20°, roughly corresponding to the North America, median power spectral density of quasi-perpendicular waves is enhanced at nearly all MLTs. The largest wave intensity can be observed in the morning sector. Additionally the median power of quasi-perpendicular waves is enhanced in the whole morning sector, except for the longitudes roughly corresponding to the Atlantic and the Pacific oceans. Finally, there is another MLT - geomagnetic longitude interval of high median wave power between about 15 and 24 hours at geomagnetic longitudes between about 80° and 120°, corresponding to the location of enhanced normalized whistler rate.

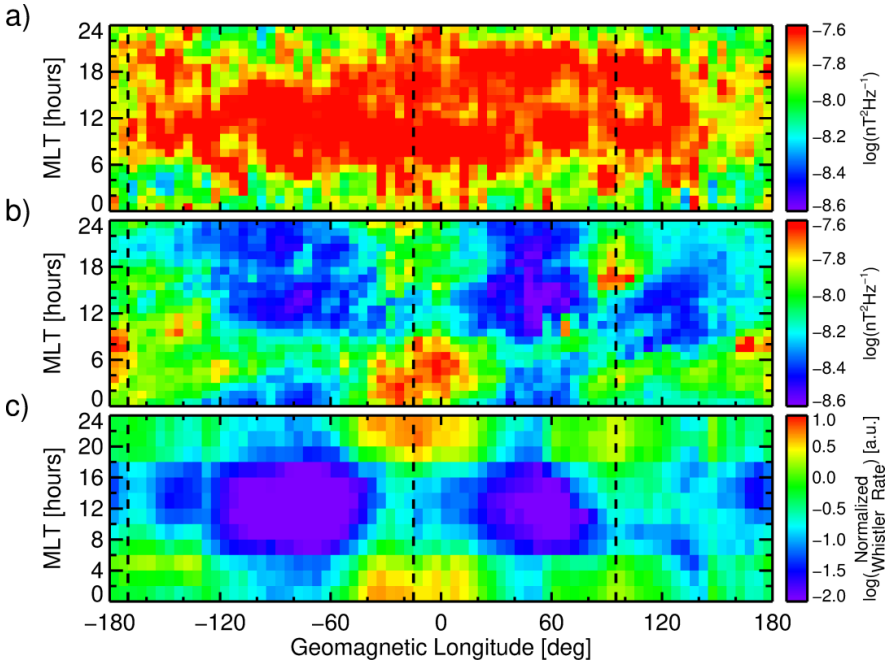

Figure 4.14: a) Same as Figure 4.13a, but only for wave normal angles lower than 30°. b) Same as Figure 4.13a, but only for wave normal angles larger than 60°. c) Normalized lightning occurrence rate as a function of MLT and the geomagnetic longitude. The dashed lines mark the longitudes of the largest normalized lightning occurrence rates. Reprinted from Záhlava et al. [2018b].

Being significantly better pronounced in the case of the quasi perpendicular waves, the longitudinal dependence suggests a high importance of the non-ducted whistlers [Bortnik et al., 2003]. This also explains the overall decrease of the wave intensity at higher frequencies as, for each wave frequency, there is a maximal L-shell which such a wave can reach before being reflected back. This maximal L-shell decreases with increasing frequency. Considering the eccentric nearly equatorial orbits of the Van Allen Probes, the high frequency waves would be expected to occur only in a small portion of all measurements. In fact, the frequency extent of the longitudinal dependence is indeed slightly different in different L-shell ranges, reaching higher frequencies at smaller radial distances (not shown). The causal link to lightning is also in agreement with the limitation of the effect to within the plasmasphere, as lightning-generated whistlers are rather rare in the plasma trough [Bell et al., 2004, Platino et al., 2005].

In summary, Záhlava et al. [2018b] confirmed the observations of Green et al. [2005] that the intensity of whistler mode waves at frequencies as low as about 400 Hz exhibits a significant dependence on the geomagnetic longitude. We have also shown that the longitudinal dependence can be observed up to about 7.5 kHz in the case of the Van Allen Probes inside the plasmasphere. The longitudinal dependence substantially varies with the MLT, being most pronounced in the evening-to-morning sector, and especially in the case of highly oblique wave normals. During the day, the only observable wave power enhancement can be found over the North America. Finally, the longitudinal dependence well follows the lightning occurrence rates corrected for the ionospheric attenuation.

5. Attenuation Events

In the Earth's magnetosphere, numerous types of special wave events of both known and unknown origin can be observed. There are several event types produced by the man-made devices. We should definitely mention the activity of powerful military transmitters that produce narrow-band signals at several given frequencies [Bullough et al., 1975, Cohen and Inan, 2012]. Aside from the original frequency bands and the sideband structures, the interaction between close enough transmitters can result in the events based on their frequency difference [Němec et al., 2017]. Another artificial source of electromagnetic power observed by spacecraft is the electric power distribution network. Based on the location, the so called Power Line Harmonic Radiation (PLHR) consists of narrow frequency bands of enhanced wave intensity equidistantly spaced 50 or 60 Hz apart [Bullough, 1995]. Rather similar pattern, but with the frequency spacing not corresponding to the power system frequencies, can be observed occasionally at frequencies of the order of kilohertz [Rodger et al., 1999, Němec et al., 2009]. Such events are known as Magnetospheric Line Radiation (MLR), and their generation mechanism is still not well understood [Rodger et al., 2000, Bezděková et al., 2015]. However, they are believed not to be man-made [Rodger et al., 2000]. Another natural events with not yet clarified origin are Quasi-periodic (QP) emissions consisting of consecutive nearly periodically occurring wave elements of enhanced wave intensity [Helliwell et al., 1975]. They are observed at frequencies of the order of kilohertz, with typical modulation periods on the order of minutes [Hayosh et al., 2014, Bezděková et al., 2019].

Besides the natural events produced at larger radial distances, special events related to the lightning activity can be observed. Two types of such events are discussed in this chapter. They were observed by the DEMETER spacecraft, one in the VLF range [Záhlava et al., 2015] and the other in the ELF range at frequencies below 1 kHz [Záhlava et al., 2018c]. Their frequency-time characteristics are otherwise quite similar, consisting of several frequency bands of alternating enhanced and reduced wave intensity.

5.1 VLF Attenuation Events

During its six and half year mission, DEMETER collected over 55000 frequency-time spectrograms of power spectral density of electric field fluctuations in the VLF range while operating in the Survey mode. Each such spectrogram covers one half-orbit of the spacecraft. Due to the specific spacecraft orbit, half of them was measured during the day-time, while the other half during the night-time. We visually inspected all these spectrograms for the presence of events similar to that presented by Parrot et al. [2015] in their Figure 12. This example is shown in Figure 5.1. The data were recorded on 27 February 2007 between 05:57 and 05:59 UT over the west coast of the North America, and a color coded power spectral density of electric field fluctuations is plotted as a function of time and frequency. The frequency range of the event is marked by the white curly brackets. Notice the approximately horizontal bands of enhanced and reduced wave intensity. Parrot et al. [2015] suggested that they are likely linked to the lightning activity.

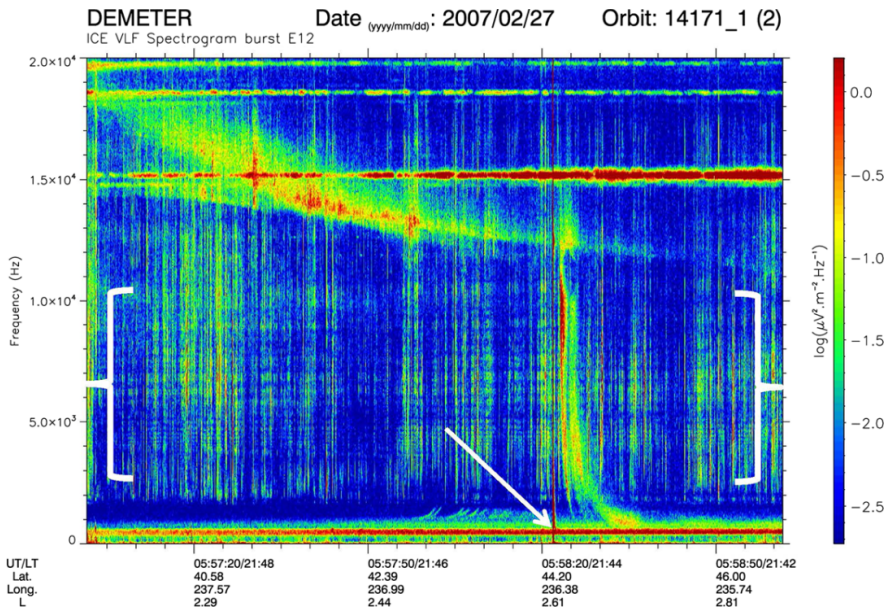

Figure 5.1: Color-coded frequency-time spectrogram of power spectral density of electric field fluctuations recorded by the DEMETER spacecraft in the VLF range on 27 February 2007 between 05:57 and 05:59 UT. The white curly brackets show the frequency interval where the event of interest was observed. Reprinted from Figure 12 (top) of Parrot et al. [2015].

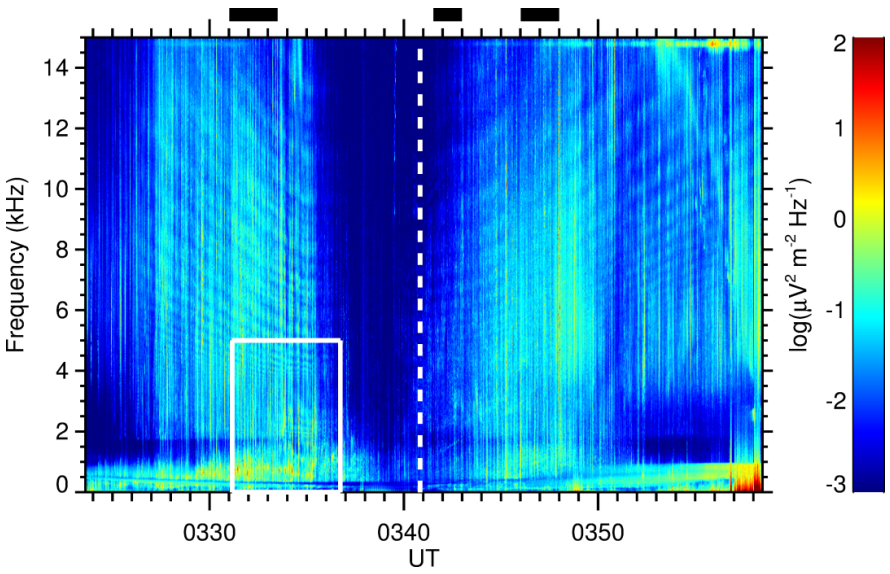

Figure 5.2: Frequency-time spectrogram of power spectral density of electric field fluctuations corresponding to one of the observed events. The frequencies of reduced intensity first decrease with time, then there is an apparent gap in the event, and, finally, the frequencies of reduced intensity increase with time. The data were measured on 7 February 2007. The white vertical dashed line at about 03:41 UT corresponds to the time when DEMETER crossed the geomagnetic equator. Black bars on the top mark the time interval when the Burst mode was active and high-resolution data were available. Reprinted from Záhlava et al. [2015]

The visual inspection revealed that no such events can be observed in the daytime spectrograms, however, as many as 1601 events were identified during the night-time. An example of one of the identified events is shown in Figure 5.2. The color-coded power spectral density of electric field fluctuations has a characteristic pattern of alternating enhanced and reduced intensity frequency bands. The structure contains (as in most cases) a gap near the geomagnetic equator, location of which is marked by the vertical white dashed line. Given the assumption of the events being of the lightning origin, the gap is most probably due to the significantly larger wave attenuation in the ionosphere close to the magnetic equator [Němec et al., 2008, Helliwell, 2014]. The example event was observed on 7 February 2007 between about 3:20 and 4:00 UT. The black boxes on the top mark the availability of the Burst mode data. Finally, the white rectangle marks the frequency-time interval shown in Figure 5.3a.

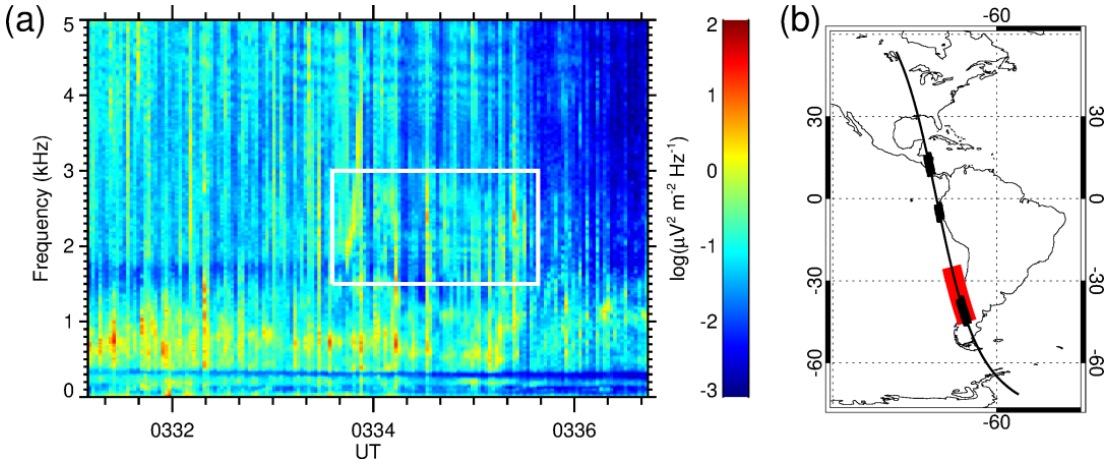

Figure 5.3: (a) Zoomed frequency-time spectrogram of power spectral density of electric field fluctuations corresponding to the interval marked by the white rectangle in Figure 5.2. The white rectangle marks an additional faint reduced intensity event at lower frequencies. (b) Map showing the DEMETER locations during the time interval analyzed in Figure 5.2 (thin curve). The part of the DEMETER orbit corresponding to the zoomed interval from Figure 5.3a is shown by the solid red rectangle. Parts of the DEMETER orbit with the active Burst mode are shown by the thick black curves. Note that DEMETER moved from the south to the north. Reprinted from Záhlava et al. [2015].

Figure 5.2 reveals several typical characteristics of the VLF events. The frequencies of the alternating bands first decrease with time, and the bands get narrower. At later times, the band frequencies increase again and the bands widen. In some cases, only one, either falling or rising, part of the event can be observed. The frequency spacing between the bands increases with increasing frequency. Specifically, while the frequency spacing is about 0.2 kHz at 4 kHz it grows up to almost 1 kHz at 10 kHz. For each event, the starting and ending times as well as the minimal and maximal frequencies closest to the bottom of the U shape possible were marked.

A three-minute zoom of the example event from Figure 5.2 is shown in Figure 5.3a. In addition to the main event at frequencies above about 3.5 kHz, the white rectangle marks a short-lasting rather similar structure at frequencies

above about 1.7 kHz. The two frequencies mentioned roughly correspond to the first two critical frequencies of the night-time Earth–ionosphere waveguide [Toledo-Redondo et al., 2012]. Figure 5.3b shows the trajectory of the DEMETER spacecraft during the given half-orbit (thin curve). The thick black parts show the areas where the Burst mode was active, and the red bar marks the time interval plotted in Figure 5.3a.

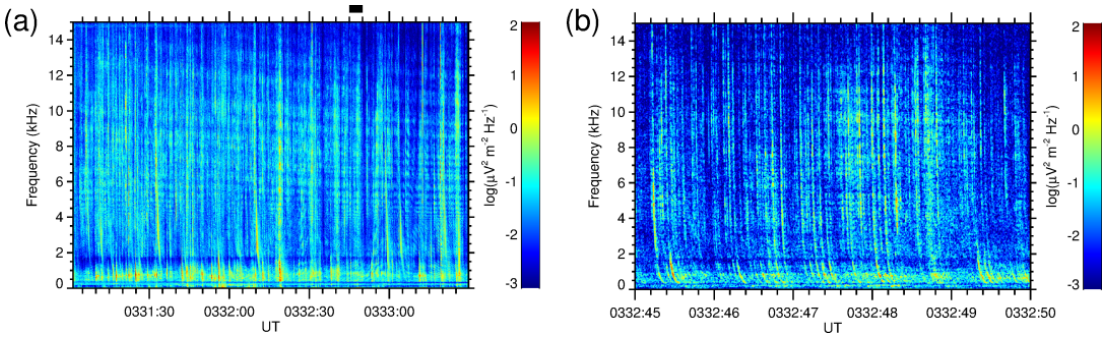

Figure 5.4: (a) Detailed frequency-time spectrogram of power spectral density of electric field fluctuations corresponding to the first Burst mode interval from Figure 5.2. (b) Detailed frequency-time spectrogram corresponding to a 5 s long time interval marked by the black bar on the top po Figure 5.4a. Reprinted from Záhlava et al. [2015].

To have a more detailed view on the event structure, the first Burst mode interval marked in Figure 5.2 was used to calculate the frequency-time spectrogram with a better time resolution. This is shown in Figure 5.4a. The plot suggests that the event consists of numerous consecutive lightning-generated whistlers, intensity of which is significantly reduced at some frequencies. This is supported by a further zoomed view in Figure 5.4b. The time interval marked by the black rectangle on the top of Figure 5.4a is shown. Given such evidence, it is unlikely that the events would be produced by a frequency-dependent source. Also note that in the zoomed plots in Figure 5.4, the enhanced intensity bands seem to be approximately horizontal, as their frequencies gradually change on longer time scales. The evolution of the frequencies of attenuation might be of either temporal or spatial origin. Unfortunately, this cannot be clearly determined using only a single spacecraft observation. Nevertheless, our further analysis demonstrates that the events are most probably produced by a localized lightning source and the frequency change is due to the changing distance between the spacecraft and the source storm.

The identified durations of the events vary from several minutes up to about 30 minutes (principally the entire half-orbit), with most events lasting between about 5 and 10 minutes. The exact distribution of the event durations is shown in Figure 5.5. We note that for the purpose of the duration estimation the equatorial gaps were ignored. Given the orbital velocity of the DEMETER spacecraft be about 400 km per minute, we can estimate the corresponding spatial extent of the events to be between about 2000 and 4000 km.

The events usually spanned over a significant portion of the DEMETER VLF frequency range. Figures 5.6a and 5.6b show, respectively, histograms of minimal and maximal frequencies of the events. Unfortunately, it was not possible

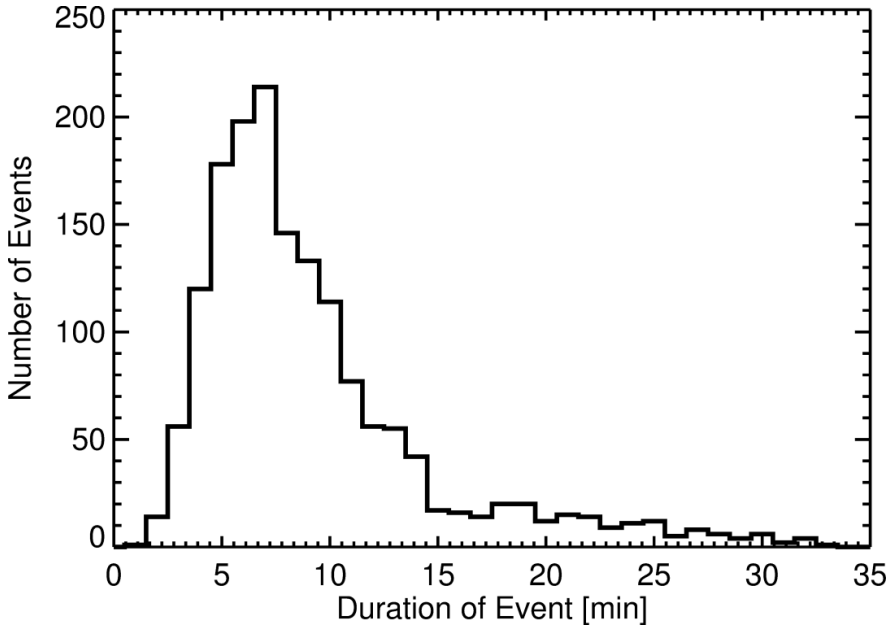

Figure 5.5: Histogram of the observed event durations. Reprinted from Záhlava et al. [2015].

to achieve much better frequency resolution than about 0.5 kHz as it was often difficult to determine the exact minimum or maximum frequency of the event. Especially in the case of the minimum frequencies, the equatorial gap often coincided with the bottom of the event U-like shape. The events were mostly limited to frequencies above about 3 to 4 kHz, roughly corresponding to twice the critical frequency of the Earth–ionosphere waveguide. The upper frequency limit varies between about 5 and 15 kHz. This is mostly due to the events gradually weakening at high frequencies, making the upper frequency limit little blurred. As was shown in Figure 5.3a, some of the events were accompanied by additional lower frequency parts. A histogram of minimum frequencies of these additional events is shown in Figure 5.6c. The values are usually between about 1.5 and 2.0 kHz, which is close to the critical frequency of Earth–ionosphere waveguide during the night ($\approx$ 1.7 kHz).

In addition to the beginning and ending times, a central time was marked for each event. This was selected as the moment closest to the minimum of the event frequency dependence, and it is further considered as the event location. Geographic locations of the events are then shown in Figure 5.7a, which depicts color coded numbers of events in individual 2.5° $\times$ 2.5° latitude-longitude bins. Most of the events are observed west off the Africa. For the comparison, average lightning occurrence rates in the local time window from 20.7 to 23.7 h are shown in Figure 5.7b. The lightning data were obtained by the spacecraft missions LIS/OTD, and the local times selected roughly correspond to the night-time half-orbits of the DEMETER spacecraft. Lightning activity is the largest at three main locations, namely Africa, and both North and South America. Comparing the two maps, one can see that the event locations appear to be somewhat related to the lightning occurrence, but they are noticeably shifted in the west/south-west direction.

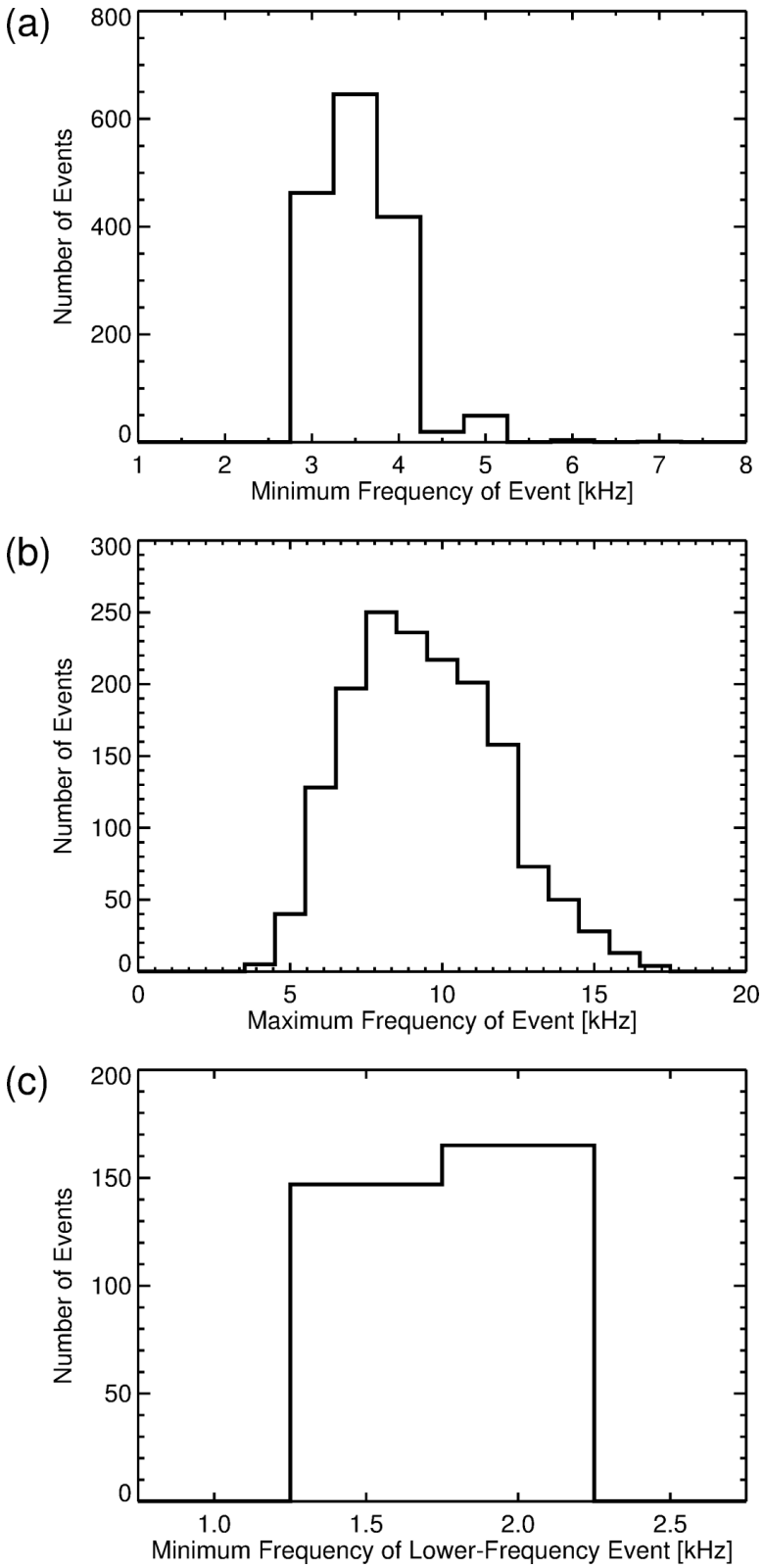

Figure 5.6: (a) Histogram of minimum frequencies of events. (b) Histogram of maximum frequencies of events. (c) Histogram of minimum frequencies of lower frequency events. The frequency resolution of all these histograms is 0.5 kHz. Reprinted from Záhlava et al. [2015].

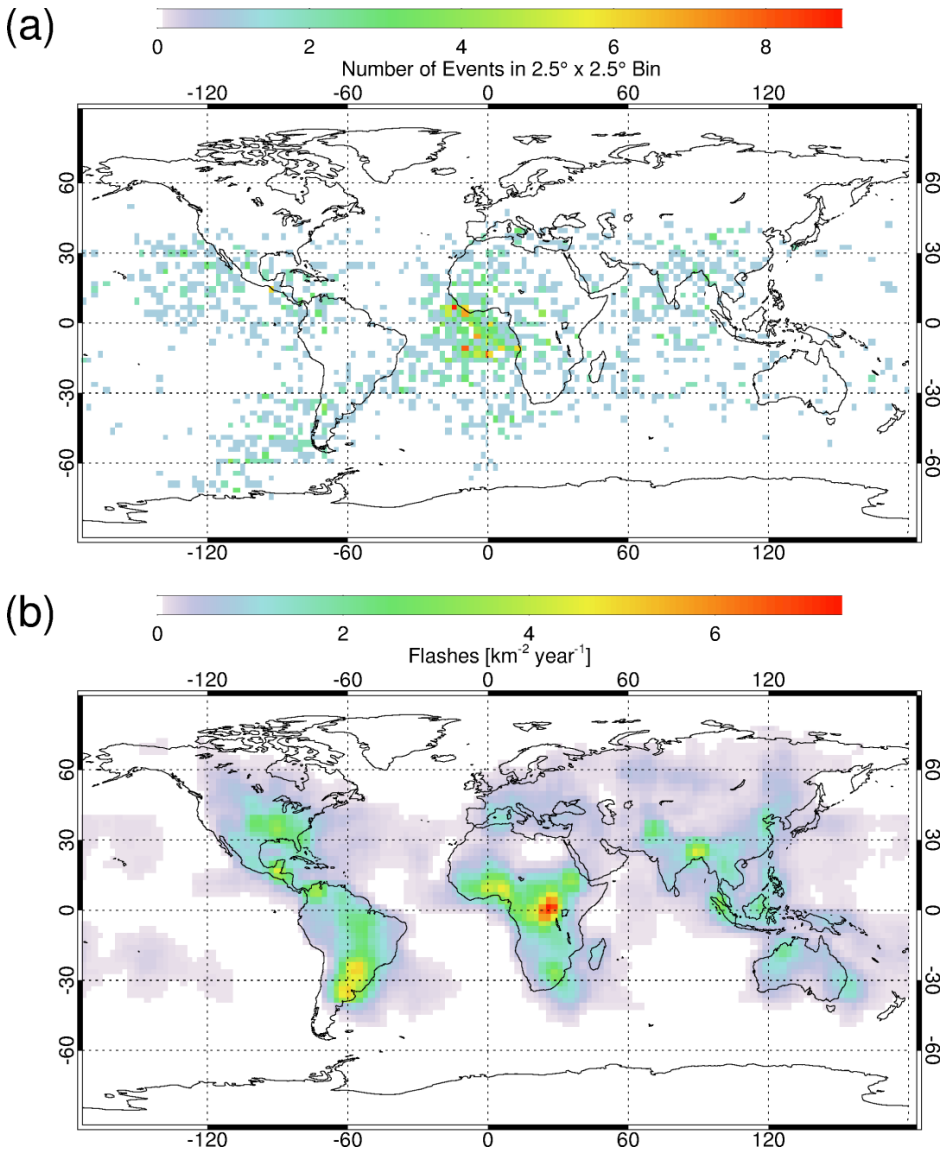

Figure 5.7: (a) Map of event locations. The location of a given event is determined as the location of the DEMETER spacecraft at the time of the minimum of the event frequency dependence. The number of events in each 2.5° × 2.5° bins is color coded according to the scale on the top. (b) The average lightning activity from LIS/OTD in the local time window 20.7-23.7 h is color coded according to the scale on the top. This local time range corresponds to DEMETER night-time half-orbits. Reprinted from Záhlava et al. [2015].

We note that both the lightning and the event occurrence exhibit a seasonal variation, however, for the general overview the overall average suffices. The observed positional shift of the events with respect to lightning can be likely explained by the event formation mechanism we suggest. This supposes that the lightning-generated waves need to propagate in the Earth–ionosphere waveguide over some distance in order to form the event. Given that the event formation is likely determined by the spacecraft-to-source storm distance, one has to incorporate the spacecraft orbit in the shift calculation.

For a better comparison, we thus show a shifted lightning occurrence map in Figure 5.8b. Assuming that the event frequency is the lowest at the time when the spacecraft is the closest to the source storm, the relevant lightning occurrence should be that shifted in a direction perpendicular to the spacecraft orbit at a given location (see Figure 5.8a). The visual comparison of the two maps in Figure 5.7 clearly shows that the lightning occurrence to the east/north-east from the event location should be used. We note, however, that the reason for the observed preferential shift in one direction can be only guessed (see below).

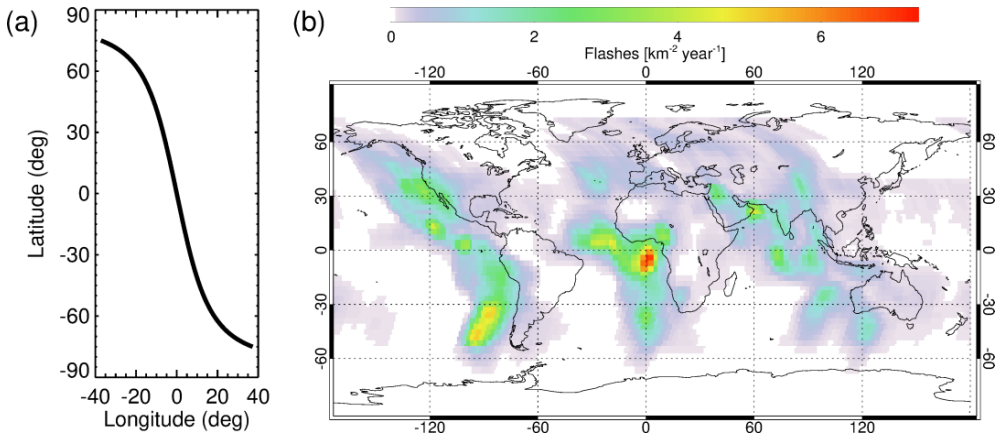

Figure 5.8: (a) Trajectory corresponding to a DEMETER nightside half-orbit. (b) Map of lightning locations from LIS/OTD shifted by 3000 km in the west/southwest direction. The direction of the shift was determined in each location to be perpendicular to the DEMETER orbit at the resulting shifted location, i.e., the shifted location is the place where the DEMETER spacecraft gets closest to the original location. Reprinted from Záhlava et al. [2015].

Another parameter coming into the shifting process is the characteristic distance. The shifted lightning occurrence was evaluated for various distances, and the best agreement between the event locations and the shifted lightning occurrence was obtained for a distance of about 3000 km. However this obtained characteristic shift corresponds to an average situation, the behavior of individual events may be clearly different both in distance and direction, as in the case study shown in Figure 5.9.

We further propose a mechanism of the event formation. It is based on the propagation of lightning-generated waves in the Earth–ionosphere waveguide and their subsequent leaking through the ionosphere up to the DEMETER spacecraft. Two well pronounced events were selected for case studies to demonstrate the idea and performance of the suggested model. Frequency-time spectrograms of

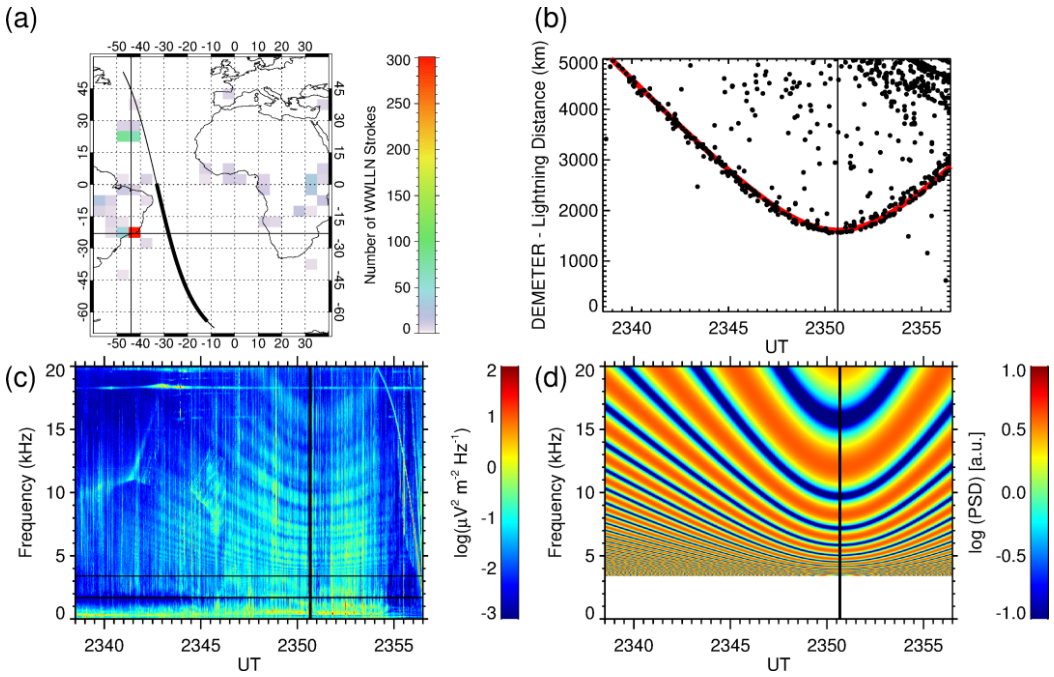

Figure 5.9: (a) DEMETER orbit is shown by the thin curve. The thick curve corresponds to the part of the DEMETER orbit where the event was observed. Numbers of lightning strokes detected during this time interval by the WWLLN network in individual 5° × 5° bins are color coded according to the scale on the right. The thin horizontal and vertical lines mark the position of a source storm (see text). (b) Distances between individual lightning strokes detected by WWLLN and the DEMETER spacecraft are shown by the black points as a function of time. The red curve shows the distance between the DEMETER spacecraft and the location of the source storm. The black vertical line marks the time when DEMETER gets closest to the source storm. (c) Frequency-time spectrogram of power spectral density of electric field fluctuations corresponding to the event. The data were measured on 29 March 2010. (d) Model frequency-time spectrogram calculated using modal interference between TM1 and TM2 modes of the Earth–ionosphere waveguide. Reprinted from Záhlava et al. [2015].

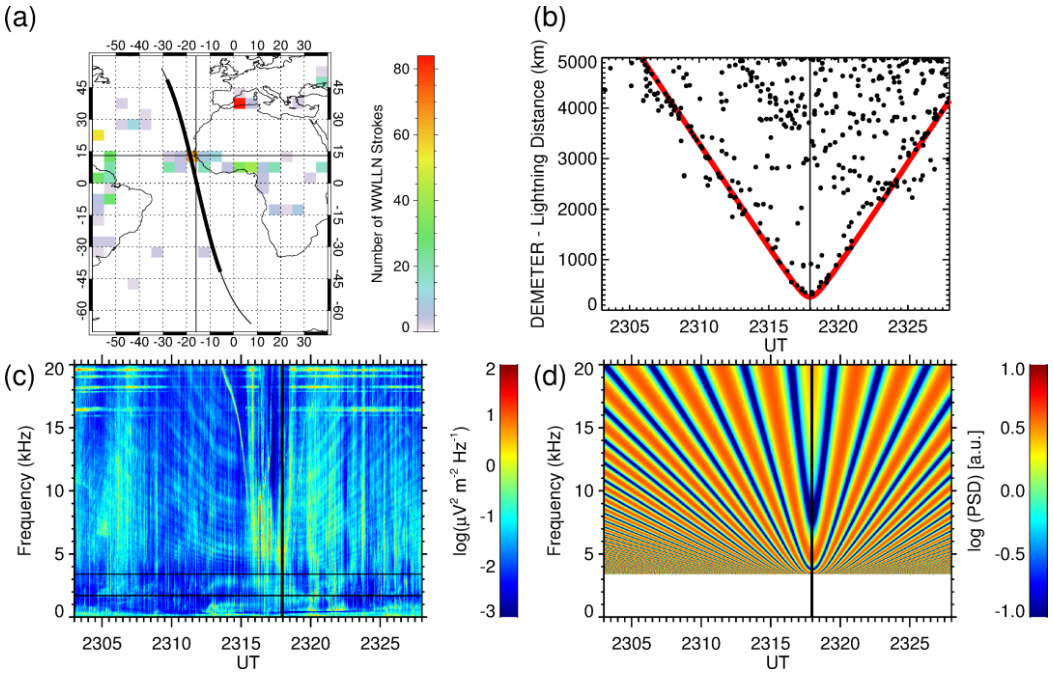

Figure 5.10: The same as Figure 5.9 but for the event measured on 22 September 2007. Note that the situation is less clear than in Figure 5.9, with several different storms occurring in the vicinity of the DEMETER spacecraft at the time of the event. Also note that the DEMETER spacecraft passed very close to the source storm in this particular event. Reprinted from Záhlava et al. [2015].

power spectral density of electric field fluctuations containing the two reduced intensity events are shown in Figures 5.9c and 5.10c. The measurements took place on 29 March 2010 and 22 September 2007, respectively. The first two critical frequencies of the Earth–ionosphere waveguide, i.e., 1.7 and 3.4 kHz, are marked by the horizontal black lines. The vertical black lines correspond to the moments when the spacecraft got closest to the source storms.

Numbers of lightning strokes detected during the events by the WWLLN are shown in Figures 5.9a and 5.10a gridded into $5° \times 5°$ map bins. The horizontal and vertical black lines mark, respectively, the latitude and longitude of the lightning cluster evaluated as a source storm responsible for the event. The thin black curve shows the DEMETER trajectory, whereas its thick part corresponds to the time interval when the event was observed. Note that the spacecraft traveled in the south-to-north direction during its night-time half-orbits. Distances between individual lightning strokes and the contemporary spacecraft locations are plotted in Figures 5.9b and 5.10b. The black dots represent individual lightning strokes and the red curves mark the spacecraft – source storm distances. The vertical black lines show the times of the closest flybys. Especially in the case of Figure 5.9b, a significant number of the strokes is located close to the red curve. On the other hand, lightning strokes in Figure 5.10b suggest two other possible source storms.

The performance of the suggested event model is shown in Figures 5.9d and 5.10d. The model is based on the waveguide mode theory, considering the Earth–ionosphere cavity to be an ideal coplanar waveguide characterized by the boundary distance h, following the theory introduced in section 1.4. We suppose that

a lightning stroke produces waves that propagate in the direction of x axis and can be described by equation

$$E(f, x) \propto \exp\left(-ikx \cos\Theta\right). \tag{5.1}$$

For the purpose of the calculation, we assume the Earth–ionosphere distance $h \approx 88$ km, corresponding to the critical waveguide frequency $f_1 = 1.7$ kHz. For the sake of maximal simplicity, only the first two waveguide modes are used. This is justified by considering that higher modes get significantly attenuated on the event characteristic distances [Parrot et al., 2008]. The resulting signal intensity at a given distance x is then calculated as a sum of the first two waveguide modes, using their complex amplitudes. The obtained sum exhibits an interference pattern of alternating frequencies of enhanced and reduced wave intensity. Similarly as in the case of the observed events, the frequencies of attenuation vary with the distance from the source. Unfortunately, this model cannot explain the additional lower frequency events below the 3.4 kHz limit. In such case, one would have to consider the interference of TM0 and TM1 modes.

The model does roughly reproduces general characteristics of the events, however, the detailed structure differs. For a more complex result, which would better reproduce the observed events, one should incorporate higher waveguide modes in the calculation as well as wave attenuation in the waveguide. Additionally, the non-planar geometry and possible inhomogeneities of the waveguide might be eventually important.

The event locations and their rather rare occurrence is the final question to answer. Given the event formation mechanism, their durations, and typical time scales of lightning strokes, it is obvious that a large number of consecutive strong strokes taking place in roughly the same location is needed for the event formation. Additionally, the lightning-generated waves need to travel over a non-negligible distance in the Earth–ionosphere waveguide to form the interference pattern. Given such specific conditions to be met, the rather small number of event observations is justified. Considering the preferentially westward shift of the event locations with respect to the lightning activity, we suggest that it is due to the asymmetric wave attenuation in the Earth–ionosphere waveguide described in section 1.4. The attenuation is larger in the case of westward propagation compared to that in the eastward direction. This means that the event can be formed at smaller distances from the source to the west from the storm, lowering a probability of being obscured by a lightning activity from other regions.

In summary, we visually identified 1601 VLF events consisting of alternating bands of enhanced and reduced wave intensity. Their geographic distribution corresponds to lightning occurrence rates shifted in the west/south-west direction perpendicular to the night-time DEMETER half-orbit by about 3000 km. We proposed a possible formation mechanism of the events based on the propagation of lightning-generated waves in the Earth–ionosphere waveguide and the waveguide mode interference. This model is able to reproduce and explain some of the main event properties.

5.2 ELF Attenuation Events

Searching through the Burst mode spectrograms obtained by the DEMETER spacecraft in its ELF range, wave events qualitatively similar to those discussed in the previous section were discovered. Frequency-time spectrogram of power spectral density of electric field fluctuations containing an example of such an ELF event is shown in Figure 5.11.

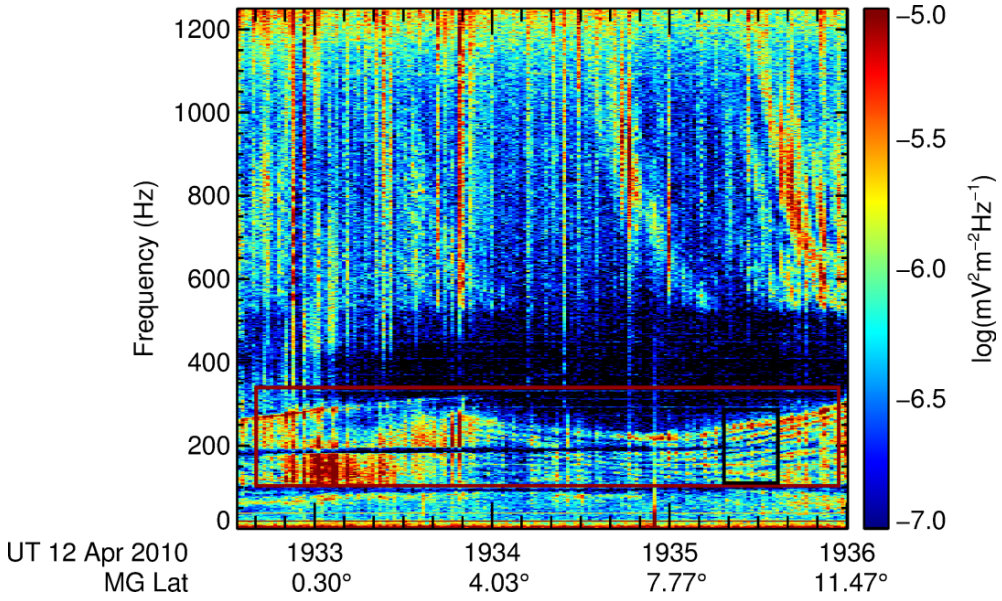

Figure 5.11: Frequency-time spectrogram of power spectral density of electric field fluctuations measured by the DEMETER spacecraft on 12 April 2010 from 19:32:35 UT to 19:36:00 UT. The red rectangle marks a frequency-time interval of an example of the studied extremely low frequency events. Moreover, part of the event selected for a detailed analysis as well pronounced and unbiased by other wave phenomena is framed by the black rectangle. Reprinted from Záhlava et al. [2018c].

The frequency-time interval containing the event is marked by the red rectangle. The events, again, consist of several alternating frequency bands of enhanced and reduced wave intensity. Similarly to the VLF events, the bands of reduced wave intensity form a U-shaped structure, and their frequency spacing decreases close to the bottom of the U shape. In the case of the ELF events, one-sided events were observed more often. As the ELF range was not monitored with a sufficient frequency resolution in the Survey mode, only the Burst mode data is used. In total 3,416 hours of measurements were searched and 263 ELF events were identified and localized. Unlike the VLF events, some of the ELF events were observed also during the day-time half-orbits, however, the majority of them occurred on the nightside (249 out of 263). Although they exhibit a rather similar pattern, only 4 ELF events occurred at the time of a VLF event, and a causal link between them thus seems unlikely.

The example event is especially well pronounced in the interval marked by the black rectangle in Figure 5.11. Moreover, it is not biased by any other wave phenomena in this frequency-time interval. Altogether, 244 such well pronounced event parts were selected for a more detailed analysis.

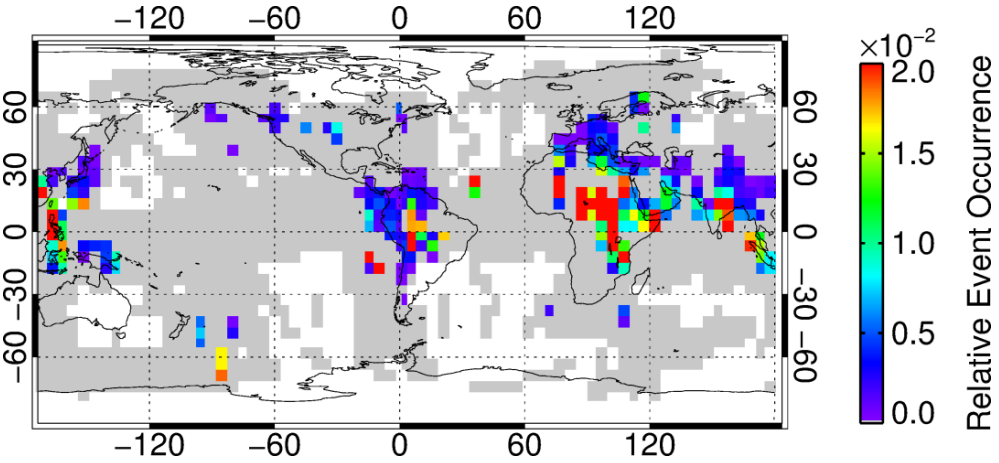

Figure 5.12: Color-coded geomagnetic map of a relative occurrence of the events. Each 5° × 5° bin shows the ratio of the total event duration to the total time of Burst mode measurements. The white color represents the areas with no Burst mode measurements. The gray color represents the areas with no events. Reprinted from Záhlava et al. [2018c].

For each individual event and each well pronounced event part, the minimum and maximum frequencies as well as beginning and ending times were marked. The geomagnetic map of the event relative occurrence is shown in Figure 5.12. The value in each 5° × 5° bin is calculated as a ratio between the total event duration and the total Burst mode measurement duration. The white color corresponds to locations where the Burst mode was not active, whereas the gray color shows the areas where, despite the active Burst mode, no events were observed. Most events were observed within about 30° from the geomagnetic equator, and they are clustered in three main occurrence areas. These correspond to longitudes of South America, Central Africa and the Far East. The latter two apparently merge into one. Generally, the events appear to be more common over the landmass than over the ocean.

Another similarity between the two types of events appears to be in their seasonal occurrence. Figure 5.13 shows the fraction of the ELF(red) and VLF(green) events observed in individual months. The plotted error bars correspond to one standard deviation of a binomial distribution given by

$$\sigma = \sqrt{p(1-p)/N}, \tag{5.2}$$

where N is the total number of events, and p is their relative occurrence in a given month. It is noteworthy that the occurrences of both types of events peak in spring and autumn, whereas only a few of them are observed in summer and winter. The event occurrence is compared with the average flash rate (blue) observed by the OTD/LIS. The flash rate uses the scale given by the right-hand side ordinate. In order to obtain more appropriate results, only lightning observed at geomagnetic latitudes within 30° from the equator and in two geomagnetic longitude intervals (between −20° and 20° and from 70° to 220°) was taken into account. To match the local times when most of the events were observed, the interval between 20 and 24 hours was used. The obtained lightning occurrence also has a peak in autumn, however, it is only slightly enhanced in spring.

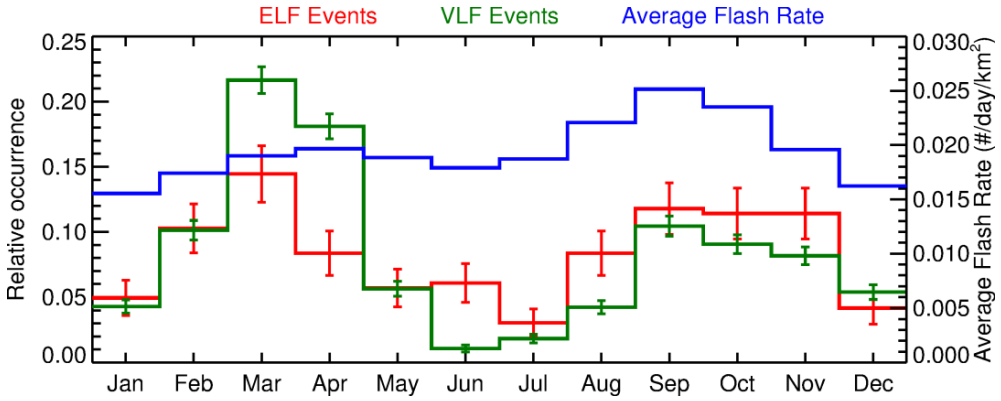

Figure 5.13: Seasonal variation of the occurrence of ELF(red) and previously studied VLF(green) events [Záhlava et al., 2015]. The numbers of events in individual months are normalized by the total number of events. The error bars show one standard deviation. The blue line shows the average flash rate at geomagnetic latitudes lower than 30° and at geomagnetic longitudes from −20° to 20° and from 70° to 220°, where the events are predominantly observed. Reprinted from Záhlava et al. [2018c].

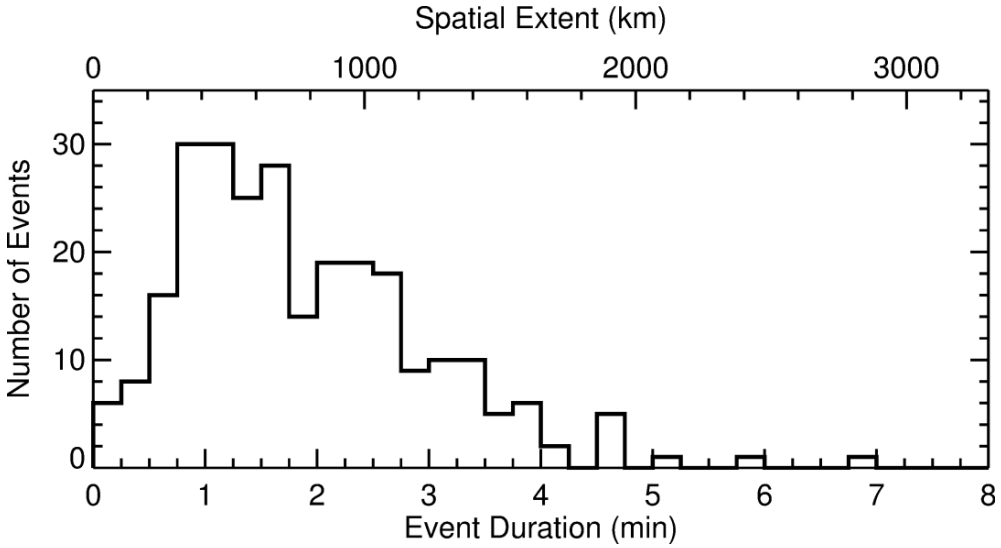

Figure 5.14: Histogram of the observed event durations. The spatial scale at the top was calculated from the observed event durations using the spacecraft orbital velocity. Reprinted from Záhlava et al. [2018c].

Figure 5.14 shows that the ELF events are usually shorter than about 4 minutes. Considering the nearly circular orbit of the DEMETER spacecraft, the upper abscissa shows a corresponding spatial extent. The events are observed over between about 200 and 1500 km. In some cases, however, the events reached one or both ends of the Burst mode interval, and their apparent duration is thus shortened due to the instrument settings.

In the case of VLF events described in section 5.1, the U shape was well pronounced and the minimum and maximum frequencies of the events were therefore marked at its bottom. Given that the ELF events consist of nearly horizontal lines, the frequency limits were marked so that they framed the whole event. Histograms of minimal and maximal frequencies of the events are shown in Figure 5.15a by the green and red colors, respectively. Apparently, there is a large group of events limited below about 500 Hz. On the other hand, the other group spans up to the upper limit of the ELF range (1.25 kHz). Having inspected the corresponding VLF range burst mode data, 9 events extend up to about 1.5 kHz, and one almost up to 2 kHz. Figure 5.15b shows a cumulative histogram of event frequencies, i.e., the value in each bin corresponds to the number of events spanning over a given frequency interval. One can see that the events occur principally in the entire ELF range.

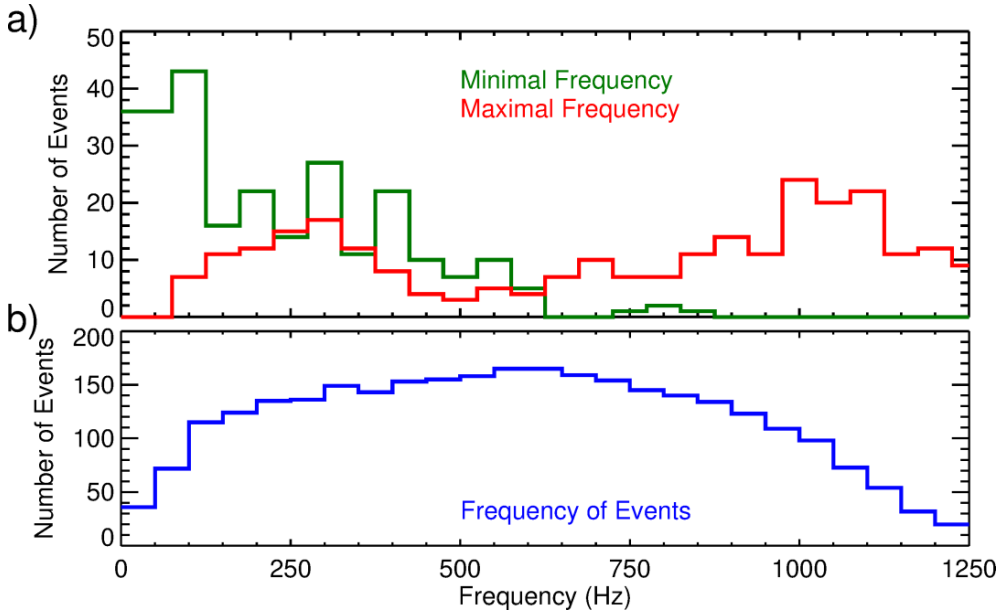

Figure 5.15: (a) Histogram of minimal (green) and maximal (red) frequencies of the events. (b) Cumulative histogram of event frequencies; that is, the total number of events which spanned over a given frequency is shown. Reprinted from Záhlava et al. [2018c].

In order to better understand the event structure, 244 frequency-time subintervals with well pronounced event structure were selected for a detailed analysis. Figure 5.16 shows the wave propagation parameters corresponding to the subinterval marked by the black rectangle in Figure 5.11, i.e., the time interval on 12 April 2007 between 19:35:18 and 19:35:37 UT. Figures 5.16a,b show the frequency-time spectrograms of power spectral density of electric and magnetic field fluctuations, respectively. The white arrows mark the manually selected

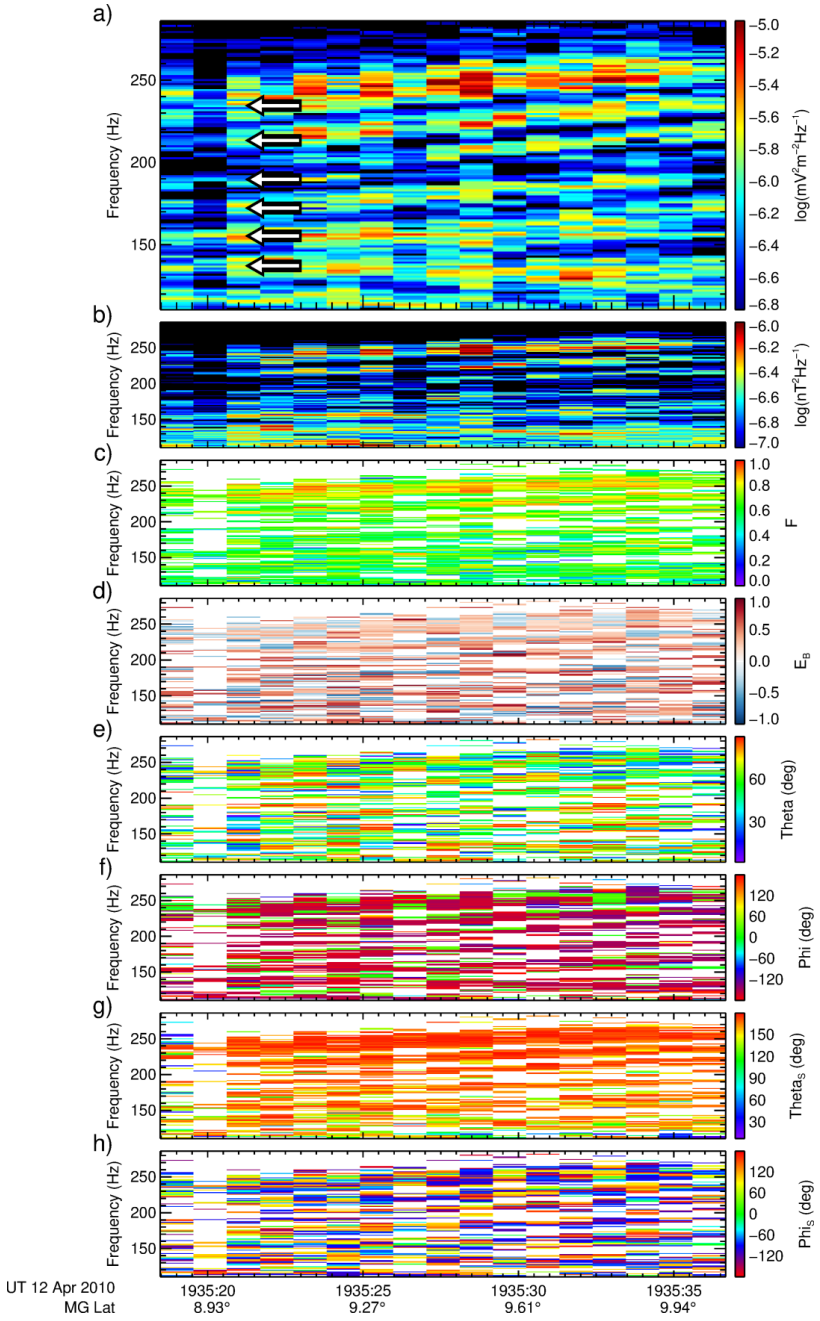

Figure 5.16: (a) Frequency-time spectrogram of power spectral density of electric field fluctuations. Frequencies of individual spectral maxima are marked by the white arrows. (b) Frequency-time spectrogram of power spectral density of magnetic field fluctuations. (c) Planarity of magnetic field fluctuations. (d) Ellipticity of magnetic field fluctuations. (e) Wave normal angle with respect to the ambient magnetic field. (f) Azimuthal angle of wave vector direction. (g) The angle between the Poynting vector and the ambient magnetic field. (h) The azimuthal direction of the Poynting vector. The measurements were taken on 12 April 2007 between 19:35:18 and 19:35:37 UT, corresponding to the frequency-time subinterval from Figure 5.11 marked by the black rectangle. Reprinted from Záhlava et al. [2018c].

frequencies of individual spectral maxima. Planarity of magnetic field fluctuations, defined as one minus ratio between the shortest and the longest axes of the polarization ellipsoid [Santolík et al., 2003], is shown in Figure 5.16c. Its values span from 0 to 1, and the maximal value corresponds to a situation of a single propagating plane wave. Figure 5.16d depicts the ellipticity of magnetic field fluctuations [Santolik and Gurnett, 2002]. It reaches values from -1, corresponding to left-handed circular polarization, through 0, i.e., the linear polarization, up to 1 which corresponds to a circular right-handed polarization. The angle between the wave normal and the ambient magnetic field is depicted in Figure 5.16e, whereas its azimuthal direction is shown in Figure 5.16f [Santolík et al., 2003]. Finally, the angle between the Poynting vector and the ambient magnetic field and the azimuthal direction of the Poynting vector [Santolík et al., 2010] are shown in Figures 5.16g and 5.16h, respectively. The azimuthal direction is defined so that the values of $\pm 180°$ correspond to the Earthward direction. For each subinterval, a threshold was set on the minimum electric power spectral density in order to select only the parts of the spectrogram with enhanced wave intensity. In this particular case, the electric wave intensity threshold was $4 \times 10^{-7} \mathrm{mV}^2 \cdot \mathrm{m}^{-2} \cdot \mathrm{Hz}^{-1}$. An additional condition was set on the planarity of magnetic field fluctuations as it, to some extent, characterizes the viability of the used methods. Therefore, only the frequency-time intervals with the planarity larger than 0.5 are used in the further analysis. Nevertheless, this restriction does not remove any significant number of data points, as is demonstrated by a rather rare occurrence of blueish color tones in Figure 5.16c. We can read that the event is formed by right-hand polarized waves with wave vector oriented oblique to the ambient magnetic field, pointing towards lower radial distances. The Poynting vector is oriented in the direction opposite to the ambient magnetic field, which corresponds, in the northern hemisphere, to the propagation away from the Earth toward the geomagnetic equator. The azimuthal direction of the Poynting vector is, however, difficult to clearly determine.

Such data selection was done for all 244 sub-events and the resulting probability densities of wave propagation parameters are shown in Figure 5.17. Namely, Figures 5.17a–f show the color-coded probability density of planarity and ellipticity of magnetic field fluctuations, wave normal angle with respect to the ambient magnetic field, azimuthal angle of wave vector, angle between the Poynting vector and the ambient magnetic field, and the azimuthal angle of the Poynting vector, respectively, all as functions of the geomagnetic latitude. The aforementioned restriction on planarity of magnetic field fluctuations is not applied in Figure 5.17a, in order to demonstrate the amount of data removed. Planarity values lower than 0.5 are obtained only rarely. Most of the waves forming the event propagate in the right-handed polarized whistler mode with rather oblique wave normals oriented towards the Earth. Poynting vectors are mostly oriented away from the Earth surface towards the geomagnetic equator. Prevailing azimuthal direction points towards lower radial distances. The only exception is a small number of events at geomagnetic latitudes between about 20° and 30°. They, however, do not exhibit any particularly different behavior when the corresponding spectrograms are investigated.

Coming back to the white arrows shown in Figure 5.16a, we further analyzed the frequencies of the spectral maxima. Individual spectral maxima were

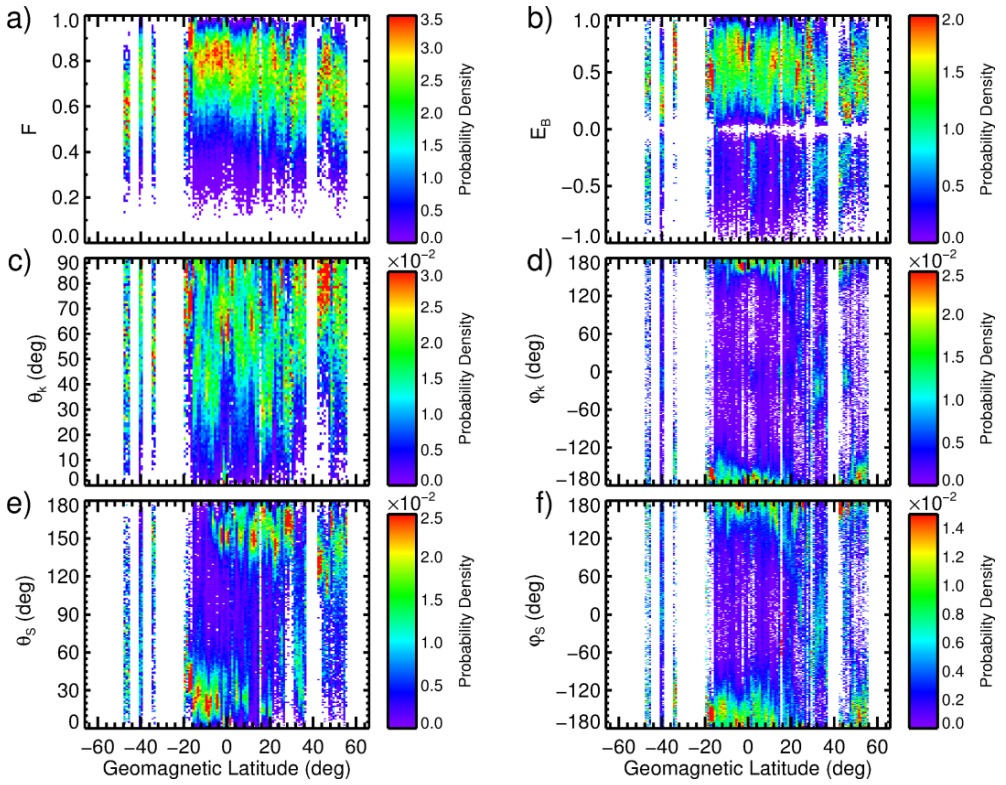

Figure 5.17: Color-coded probability density of (a) planarity of magnetic field fluctuations, (b) ellipticity of magnetic field fluctuations, (c) wave normal angle with respect to the ambient magnetic field, (d) azimuth angle of the wave normal, (e) angle between the Poynting vector and the ambient magnetic field, and (f) the azimuthal direction of the Poynting vector as a function of geomagnetic latitude. Reprinted from Záhlava et al. [2018c].

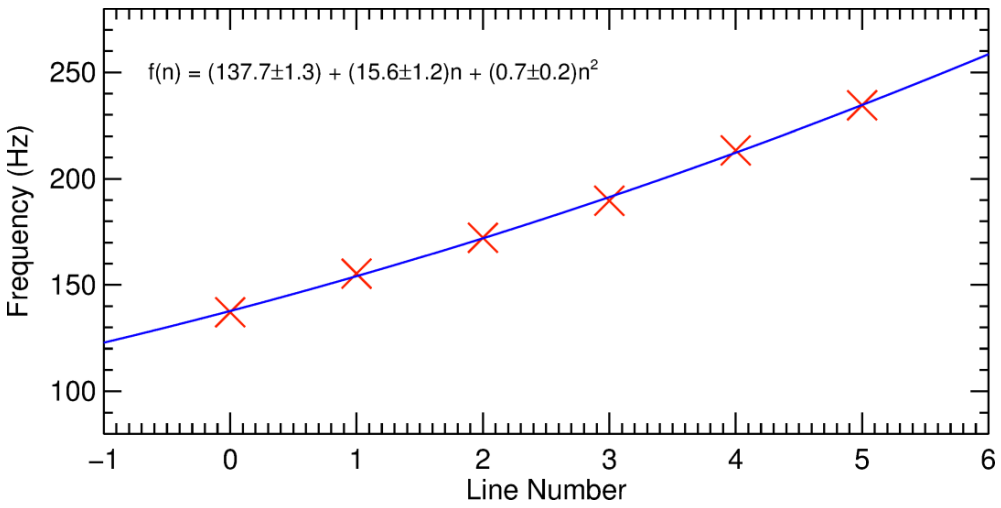

Figure 5.18: Frequencies of the spectral maxima marked by white arrows in Figure 5.16a as a function of their order are shown by the red crosses. The blue curve corresponds to the best quadratic fit. Reprinted from Záhlava et al. [2018c].

numbered by their order n, with the lowest identified spectral line frequency f_0 corresponding to the order $n = 0$. Assuming that the frequency separation between the lines might change with the frequency, we fitted the spectral peak frequencies by a quadratic form:

$$f(n) = f_0 + \Delta_f \cdot n + D_f \cdot n^2, \tag{5.3}$$

where Δ_f is the frequency spacing between the first two spectral maxima and D_f is proportional to the frequency spacing change with increasing n. Figure 5.18 shows the result of such an analysis performed for the event from Figure 5.16a. In this particular case, the frequency spacing slightly increases with the frequency.

The frequency spacing increase with the frequency is, however, not observed for all subintervals. Histograms of the fit parameters D_f and Δ_f obtained from all the subintervals are shown in Figures 5.19a,b, respectively. The distribution of the D_f parameter, i.e., the increase of the frequency spacing with frequency, is roughly centered at zero. There are events exhibiting both slight increase and decrease of the frequency spacing. However, given the accuracy of the selection of individual peak frequencies and the bandwidths of individual spectral maxima, the obtained values are well within the uncertainty of the method. The base frequency spacing Δ_f varies significantly, with the distribution having a broad peak between about 5 and 60 Hz.

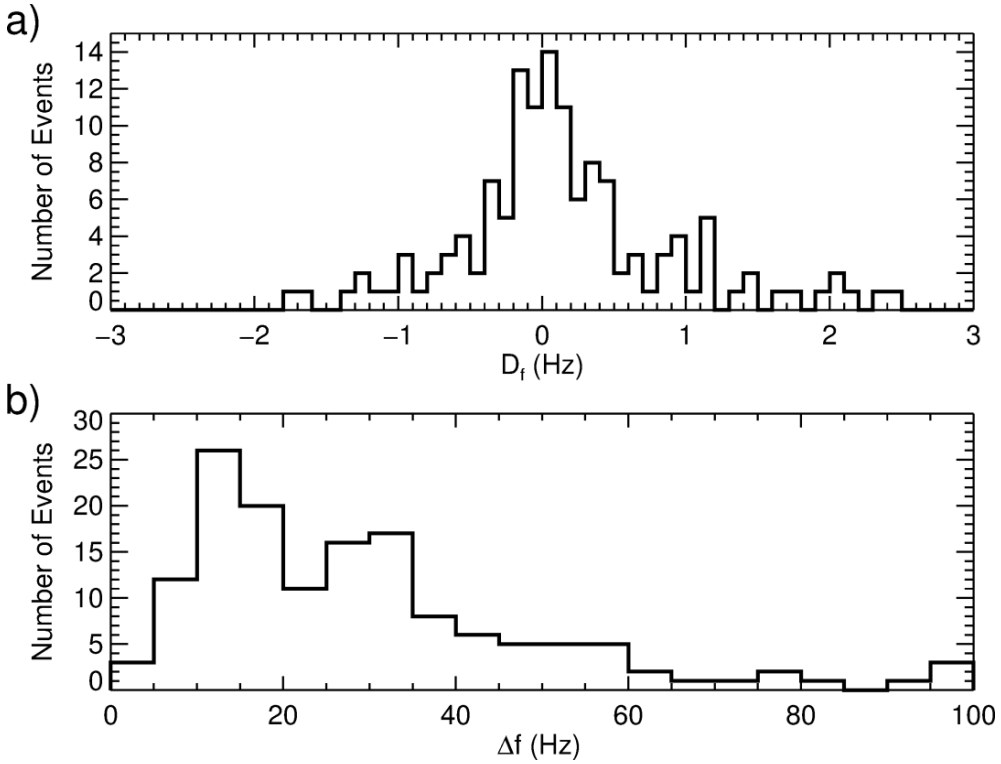

Figure 5.19: (a) Histogram of the fit parameters D_f. (b) Histogram of the fit parameters Δ_f. Reprinted from Záhlava et al. [2018c].

The qualitative similarity of the ELF and VLF events suggests that they are produced by a similar mechanism, i.e., the mode interference in a waveguide. In the case of ELF events, however, the base frequencies as well as the frequency

spacings vary significantly between individual events. This means that a hypothetical waveguide involved in the event formation would need to have a varying dimension, and therefore also the critical frequency. The waveguide critical frequency should be as low as about 50 Hz, which corresponds to the waveguide effective height of about 3000 km.

In the case of R-X whistler mode [Stix, 1992] propagating nearly perpendicularly to the ambient magnetic field, a waveguide can be formed around a maximum of the refractive index. Such refractive index maximum is expected to occur in the lower ionosphere at altitudes between about 90 and 120 km. This is demonstrated in Figure 5.20 that shows a color-coded refractive index calculated for a perpendicularly propagating wave as a function of the wave frequency and altitude. The black curve shows the local lower hybrid resonance frequency. An approximate effective height of the waveguide found around the refractive index maximum at an altitude of about 110 km can be calculated as an optical path s:

$$s = \int_{h=90\ \mathrm{km}}^{h=120\ \mathrm{km}} n(h)\mathrm{d}h, \tag{5.4}$$

where h is the altitude and $n(h)$ is the local value of refractive index. The integration is performed over the altitudinal range corresponding to the refractive index peak, assuming a specular reflection of perpendicularly propagating waves at the altitudes of the refractive index drop. This was evaluated considering a representative frequency of 500 Hz. The plasma number density and ion composition needed for the refractive index calculation were obtained from the International Reference Ionosphere model [Bilitza et al., 2014] at the time and location of the example event. Note that, according to the suggested scheme, the events are formed at altitudes of about 110 km, then escape the waveguide and are eventually observed by the spacecraft at higher altitudes. The wave propagation parameters at the spacecraft location may thus be substantially different from those in the waveguide.

In order to investigate whether the events are formed preferentially during some specific conditions, various parameters were examined for possible changes at the times of the event occurrence. Namely, we focused on the geomagnetic activity, lightning and whistler occurrence rates, and ionospheric conditions. The geomagnetic activity was studied using AE and Kp indices. Superposed epoch analysis spanning from 1 day before to 1 day after the event did not, unfortunately, reveal any systematic variation. A possible link of the event occurrence to enhanced lightning activity was studied using ground based WWLLN lightning detections. Lightning locations were compared to the spacecraft footprints during the events as well as several days before/after the events, with the aim to identify a possible specific lightning activity during the event occurrence. However, this method did not reveal any significant variation of the lightning activity at the times of the events. Similar study was performed for whistler occurrence as derived from the DEMETER RNF data, however, with a similar negative result. The approach of comparing the values obtained during the event occurrence with those obtained several days before/after effectively accounts for any possible long-term dependences. Additionally, given the DEMETER orbit, any dependence on geographic location or MLT is also effectively accounted for. Finally, 22 events took place in a reasonable proximity of ionosondes of Digital

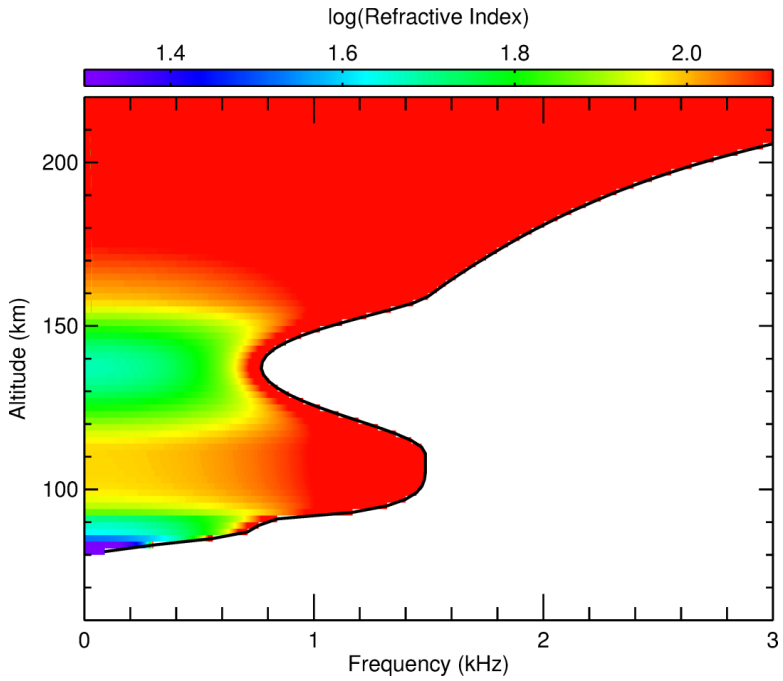

Figure 5.20: Color coded refractive index of a perpendicularly propagating wave as a function of frequency (abscissa) and altitude (ordinate) Reprinted from Záhlava et al. [2018c].

Ionogram DataBase GIRO (Global Ionospheric Radio Observatory) [Reinisch and Galkin, 2011]. Again, the ionospheric characteristics at the times of the events were compared to those shortly before/after the events, as well as to those one day apart. Similarly as for the aforementioned parameters, neither this analysis showed any significant changes.

In this section, special wave events observed at frequencies below about 1 kHz were studied. Altogether, over 3400 hours of Burst mode data obtained by the DEMETER spacecraft were visually inspected and as many as 263 events consisting of alternating bands of enhanced and reduced wave intensity were identified. Additionally, 244 well pronounced frequency-time subintervals were selected for a detailed analysis of propagation parameters of the waves forming the events. Finally, a possible formation mechanism was suggested based on a modal interference in a waveguide formed around the refractive index maximum in the lower ionosphere, at altitudes around 110 km.

Conclusion

We focused on the analysis of various lightning-related electromagnetic wave phenomena observed in the Earth's inner magnetosphere. Two principal topics were studied.

We analyzed the contribution of lightning-generated emissions to the overall wave intensity observed in the plasmasphere. Two different approaches were used. First, neural network implemented onboard the DEMETER spacecraft was used to distinguish between the times of high and low whistler occurrence, which allowed us to accordingly sort the corresponding electromagnetic wave measurements. We were thus able to determine frequency-geomagnetic latitude intervals where the wave intensity is correlated with the whistler occurrence rate. In the ELF range, the results were further compared with a wave propagation direction analysis, resulting in reasonable agreement. Second, we used the longitudinal dependence of the lightning activity and investigated a possible longitudinal dependence of the wave intensity at various frequencies. We showed that it is indeed observed, in particular during the night and for waves with quasi-perpendicular wave normal angles. This is consistent with larger ionospheric attenuation during the day and unducted whistler propagation throughout the plasmasphere.

The second topic was to analyze and understand special electromagnetic wave events observed in the ionosphere that are apparently related to the lightning activity. They consist of several frequency bands of alternating enhanced and reduced wave intensities whose frequencies continuously change over the event durations. Basic properties of the events were summarized. Additionally, their possible formation mechanisms were suggested. These are based on the modal interference of lightning-generated waves in proper waveguides. While higher frequency events are formed due to the propagation in the Earth-ionosphere waveguide, lower frequency events are likely related to the propagation in a waveguide formed around the refraction index peak in the lower ionosphere.

We demonstrated the importance of lightning generated waves for the electromagnetic wave environment in the Earth's inner magnetosphere. They can both significantly increase the overall wave intensity and result in the formation of special, previously not well understood events. Detailed evaluation of the importance of lightning-generated waves for the dynamics of energetic particles trapped in the Van Allen radiation belts remains to be done.

Bibliography

S F Abarca, K L Corbosiero, and T J Galarneau. An evaluation of the worldwide lightning location network (WWLLN) using the national lightning detection network (NLDN) as ground truth. *Journal of Geophysical Research: Atmospheres*, 115(D18), 2010. doi: 10.1029/2009JD013411.

B Abel and R M Thorne. Electron scattering loss in Earth's inner magnetosphere: 1. Dominant physical processes. *Journal of Geophysical Research: Space Physics*, 103(A2):2385–2396, 1998a. doi: 10.1029/97JA02919.

B Abel and R M Thorne. Electron scattering loss in Earth's inner magnetosphere: 2. Sensitivity to model parameters. *Journal of Geophysical Research: Space Physics*, 103(A2):2397–2407, 1998b. doi: 10.1029/97JA02920.

G McK Allcock. A Study of the Audio? Frequency Radio Phenomenon Known as" Dawn Chorus". *Australian Journal of Physics*, 10(2):286–297, 1957. doi: 10.1071/PH570286.

D N Baker, S G Kanekal, V C Hoxie, M G Henderson, X Li, H E Spence, S R Elkington, R H W Friedel, J Goldstein, M K Hudson, et al. A long-lived relativistic electron storage ring embedded in earth's outer van allen belt. *Science*, 340(6129):186–190, 2013. doi: 10.1126/science.1233518.

D N Baker, A N Jaynes, V C Hoxie, R M Thorne, J C Foster, X Li, J F Fennell, J R Wygant, S G Kanekal, P J Erickson, et al. An impenetrable barrier to ultrarelativistic electrons in the Van Allen radiation belts. *Nature*, 515(7528): 531, 2014. doi: 10.1038/nature13956.

T F Bell, U S Inan, M Platino, J S Pickett, P A Kossey, and E J Kennedy. CLUSTER observations of lower hybrid waves excited at high altitudes by electromagnetic whistler mode signals from the HAARP facility. *Geophysical Research Letters*, 31(6), 2004. doi: 10.1029/2003GL018855.

TF Bell, JP Luette, and US Inan. Isee 1 observations of vlf line radiation in the earth's magnetosphere. *Journal of Geophysical Research: Space Physics*, 87 (A5):3530–3536, 1982. doi: 10.1029/JA087iA05p03530.

J J Berthelier, M Godefroy, F Leblanc, M Malingre, M Menvielle, D Lagoutte, J Y Brochot, F Colin, F Elie, C Legendre, et al. ICE, the electric field experiment on DEMETER. *Planetary and Space Science*, 54(5):456–471, 2006. doi: 10.1016/j.pss.2005.10.016.

B Bezděková, F Němec, M Parrot, O Santolík, and O Kruparova. Magnetospheric line radiation: 6.5 years of observations by the DEMETER spacecraft. *Journal of Geophysical Research: Space Physics*, 120(11):9442–9456, 2015. doi: 10.1002/2015JA021246.

B Bezděková, F Němec, M Parrot, M Hajoš, J Záhlava, and O Santolík. Dependence of Properties of Magnetospheric Line Radiation and Quasiperiodic Emissions on Solar Wind Parameters and Geomagnetic Activity. *Journal of*

Geophysical Research: Space Physics, 124(4):2552–2568, 2019. ISSN 2169-9380. doi: 10.1029/2018JA026378.

D Bilitza and B W Reinisch. International Reference Ionosphere 2007: improvements and new parameters. *Advances in Space Research*, 42(4):599–609, 2008. doi: 10.1016/j.asr.2007.07.048.

D Bilitza, D Altadill, Y Zhang, C Mertens, V Truhlík, P Richards, L A McKinnell, and B Reinisch. The International Reference Ionosphere 2012–a model of international collaboration. *Journal of Space Weather and Space Climate*, 4: A07, 2014. doi: 10.1051/swsc/2014004.

J B Blake, D N Baker, N Turner, K W Ogilvie, and R P Lepping. Correlation of changes in the outer-zone relativistic-electron population with upstream solar wind and magnetic field measurements. *Geophysical Research Letters*, 24(8): 927–929, 1997. doi: 10.1029/97GL00859.

D J Boccippio, W J Koshak, and R J Blakeslee. Performance assessment of the optical transient detector and lightning imaging sensor. Part I: Predicted diurnal variability. *Journal of Atmospheric and Oceanic Technology*, 19(9): 1318–1332, 2002. doi: 10.1175/1520-0426(2002)019⟨1318:PAOTOT⟩2.0.CO;2.

J Bortnik and T Bleier. Full wave calculation of the source characteristics of seismogenic electromagnetic signals as observed at LEO satellite altitudes. In *AGU Fall Meeting Abstracts*, 2004.

J Bortnik, U S Inan, and T F Bell. Energy distribution and lifetime of magnetospherically reflecting whistlers in the plasmasphere. *Journal of Geophysical Research: Space Physics*, 108(A5), 2003. doi: 10.1029/2002JA009316.

J Bortnik, U S Inan, and T F Bell. Temporal signatures of radiation belt electron precipitation induced by lightning-generated MR whistler waves: 1. Methodology. *Journal of Geophysical Research: Space Physics*, 111(A2), 2006a. doi: 10.1029/2005JA011182.

J Bortnik, U S Inan, and T F Bell. Temporal signatures of radiation belt electron precipitation induced by lightning-generated MR whistler waves: 2. Global signatures. *Journal of Geophysical Research: Space Physics*, 111(A2), 2006b. doi: 10.1029/2005JA011398.

J Bortnik, R M Thorne, and N P Meredith. The unexpected origin of plasmaspheric hiss from discrete chorus emissions. *Nature*, 452(7183):62–66, 2008. doi: 10.1038/nature06741.

J Bortnik, L Chen, W Li, R M Thorne, and R B Horne. Modeling the evolution of chorus waves into plasmaspheric hiss. *Journal of Geophysical Research: Space Physics*, 116(A8), 2011a. doi: 10.1029/2011JA016499.

J Bortnik, L Chen, W Li, R M Thorne, N P Meredith, and R B Horne. Modeling the wave power distribution and characteristics of plasmaspheric hiss. *Journal of Geophysical Research: Space Physics*, 116(A12), 2011b. doi: 10.1029/2011JA016862.

F Bourriez, J A Sauvaud, J L Pinçon, J J Berthelier, and M Parrot. A statistical study over europe of the relative locations of lightning and associated energetic burst of electrons from the radiation belt. In *Annales Geophysicae*, volume 34, pages 157–164, 2016. doi: 10.5194/angeo-34-157-2016.

K G Budden. *The wave-guide mode theory of wave propagation*. Logos Press, 1961.

K Bullough, M Denby, W Gibbons, A F W Hughes, T R Kaiser, A R L Tatnall, H S W Massey, R Dalziel, and D G King-Hele. E.l.f./v.l.f. emissions observed on Ariel 4. *Proceedings of the Royal Society of London. A. Mathematical and Physical Sciences*, 343(1633):207–226, 1975. doi: 10.1098/rspa.1975.0060.

Ken Bullough. Power line harmonic radiation: Sources and environmental effects. *Handbook of Atmospheric Electrodynamics*, 2:291–332, 1995.

W J Burtis and R A Helliwell. Banded chorus–A new type of VLF radiation observed in the magnetosphere by OGO 1 an OGO 3. *Journal of Geophysical Research*, 74(11):3002–3010, 1969. doi: 10.1029/JA074i011p03002.

R K Burton and R E Holzer. Origin and propagation of chorus in the outer magnetosphere. *Journal of Geophysical Research*, 79(7):1014–1023, 1974. doi: 10.1029/JA079i007p01014.

L J Cahill and P G Amazeen. The boundary of the geomagnetic field. *Journal of Geophysical Research*, 68(7):1835–1843, 1963. doi: 10.1029/JZ068i007p01835.

D L Carpenter. Whistler evidence of a 'knee' in the magnetospheric ionization density profile. *Journal of Geophysical Research*, 68(6):1675–1682, 1963. doi: 10.1029/JZ068i006p01675.

D L Carpenter. Whistler measurements of the equatorial profile of magnetospheric electron density. *Progress in Radio Science 1960-1996, III, The Ionosphere*, pages 76–91, 1965.

D J Cecil, D E Buechler, and R J Blakeslee. Gridded lightning climatology from TRMM-LIS and OTD: Dataset description. *Atmospheric Research*, 135: 404–414, 2014. doi: 10.1016/j.atmosres.2012.06.028.

S Chapman and V C A Ferraro. A new theory of magnetic storms. *Terrestrial Magnetism and Atmospheric Electricity*, 36(2):77–97, 1931. doi: 10.1029/TE036i002p00077.

H J Christian, R J Blakeslee, D J Boccippio, W L Boeck, D E Buechler, K T Driscoll, S J Goodman, J M Hall, W J Koshak, D M Mach, et al. Global frequency and distribution of lightning as observed from space by the Optical Transient Detector. *Journal of Geophysical Research: Atmospheres*, 108(D1), 2003. doi: 10.1029/2002JD002347.

J Chum and O Santolík. Propagation of whistler-mode chorus to low altitudes: divergent ray trajectories and ground accessibility. *Annales Geophysicae*, 23 (12):3727–3738, 2005. doi: 10.5194/angeo-23-3727-2005.

M A Clilverd, D Nunn, S J Lev-Tov, U S Inan, R L Dowden, C J Rodger, and A J Smith. Determining the size of lightning-induced electron precipitation patches. *Journal of Geophysical Research: Space Physics*, 107(A8), 2002. doi: 10.1029/2001JA000301.

M B Cohen and U S Inan. Terrestrial VLF transmitter injection into the magnetosphere. *Journal of Geophysical Research: Space Physics*, 117(A8), 2012. doi: 10.1029/2012JA017992.

L M Coleman, M Stolzenburg, T C Marshall, and M Stanley. Horizontal lightning propagation, preliminary breakdown, and electric potential in new mexico thunderstorms. *Journal of Geophysical Research: Atmospheres*, 113(D9), 2008. doi: 10.1029/2007JD009459.

J J Colman and M J Starks. VLF wave intensity in the plasmasphere due to tropospheric lightning. *Journal of Geophysical Research: Space Physics*, 118 (7):4471–4482, 2013. doi: 10.1002/jgra.50217.

D D Crombie. Reflection from a sharply bounded ionosphere for vlf propagation perpendicular to the magnetic meridian. *J. Res. NBS D*, 65:455–463, 1961.

S A Cummer. Modeling electromagnetic propagation in the earth-ionosphere waveguide. *IEEE Transactions on Antennas and Propagation*, 48(9):1420–1429, 2000. doi: 10.1109/8.898776.

R L Dowden, J B Brundell, and C J Rodger. VLF lightning location by time of group arrival (TOGA) at multiple sites. *Journal of Atmospheric and Solar-Terrestrial Physics*, 64(7):817–830, 2002. doi: 10.1016/S1364-6826(02)00085-8.

R L Dowden, R H Holzworth, C J Rodger, J Lichtenberger, N R Thomson, A R Jacobson, E Lay, J B Brundell, T J Lyons, Z Kawasaki, et al. World-wide lightning location using vlf propagation in the earth-ionosphere waveguide. *IEEE Antennas and Propagation Magazine*, 50(5):40–60, 2008. doi: 10.1109/MAP.2008.4674710.

F Elie, M Hayakawa, M Parrot, J L Pinçon, and F Lefeuvre. Neural network system for the analysis of transient phenomena on board the DEMETER microsatellite. *IEICE TRANSACTIONS on Fundamentals of Electronics, Communications and Computer Sciences*, 82(8):1575–1581, 1999.

J Fišer, J Chum, G Diendorfer, M Parrot, and O Santolík. Whistler intensities above thunderstorms. In *Annales Geophysicae*, volume 28, pages 37–46. Copernicus GmbH, 2010. doi: 10.5194/angeo-28-37-2010.

J C Foster, P J Erickson, D N Baker, A N Jaynes, E V Mishin, J F Fennel, X Li, M G Henderson, and S G Kanekal. Observations of the impenetrable barrier, the plasmapause, and the VLF bubble during the 17 march 2015 storm. *Journal of Geophysical Research: Space Physics*, 121(6):5537–5548, 2016. doi: 10.1002/2016JA022509.

R J Gamble, C J Rodger, M A Clilverd, J A Sauvaud, N R Thomson, S L Stewart, R J McCormick, M Parrot, and J J Berthelier. Radiation belt electron precipitation by man-made VLF transmissions. *Journal of Geophysical Research: Space Physics*, 113(A10), 2008. doi: 10.1029/2008JA013369.

E S Gemelos, U S Inan, M Walt, M Parrot, and J A Sauvaud. Seasonal dependence of energetic electron precipitation: Evidence for a global role of lightning. *Geophysical Research Letters*, 36(21), 2009. doi: 10.1029/2009GL040396.

H Goldstein. *Classical mechanics*. Pearson Education India, 1965.

J L Green, S Boardsen, L Garcia, W W L Taylor, S F Fung, and B W Reinisch. On the origin of whistler mode radiation in the plasmasphere. *Journal of Geophysical Research: Space Physics*, 110(A3), 2005. doi: 10.1029/2004JA010495.

J L Green, S Boardsen, L Garcia, S F Fung, and B W Reinisch. Reply to "Comment on "On the origin of whistler mode radiation in the plasmasphere" by Green et al.". *Journal of Geophysical Research: Space Physics*, 111(A9), 2006. doi: 10.1029/2006JA011622.

M Hayakawa and S S Sazhin. Mid-latitude and plasmaspheric hiss: A review. *Planetary and space science*, 40(10):1325–1338, 1992. doi: 10.1016/0032-0633(92)90089-7.

Mykhaylo Hayosh, F Němec, Ondrej Santolík, and Michel Parrot. Statistical investigation of vlf quasiperiodic emissions measured by the demeter spacecraft. *Journal of Geophysical Research: Space Physics*, 119(10):8063–8072, 2014. doi: 10.1002/2013JA019731.

R A Helliwell. *Whistlers and related ionospheric phenomena*, volume 50. Stanford University Press Stanford, 1965.

R A Helliwell. *Whistlers and Related Ionospheric Phenomena (Dover Books on Electrical Engineering)*. Dover Publications, 2014. ISBN 978-0486445724.

R A Helliwell, J P Katsufrakis, T F Bell, and R Raghuram. Vlf line radiation in the earth's magnetosphere and its association with power system radiation. *Journal of Geophysical Research*, 80(31):4249–4258, 1975. doi: 10.1029/JA080i031p04249.

RH Holzworth, RM Winglee, BH Barnum, YaQi Li, and MC Kelley. Lightning whistler waves in the high-latitude magnetosphere. *Journal of Geophysical Research: Space Physics*, 104(A8):17369–17378, 1999. doi: 10.1029/1999JA900160.

ARW Hughes. Satellite measurements of whistler dispersion at low latitudes. *Advances in Space Research*, 1(1):377–380, 1981. doi: 10.1016/0273-1177(81)90138-1.

M L Hutchins, R H Holzworth, J B Brundell, and C J Rodger. Relative detection efficiency of the world wide lightning location network. *Radio Science*, 47(6), 2012a. doi: 10.1029/2012RS005049.

M L Hutchins, R H Holzworth, C J Rodger, and J B Brundell. Far-field power of lightning strokes as measured by the World Wide Lightning Location Network. *Journal of Atmospheric and Oceanic technology*, 29(8):1102–1110, 2012b. doi: 10.1175/JTECH-D-11-00174.1.

M L Hutchins, R H Holzworth, K S Virts, J M Wallace, and S Heckman. Radiated vlf energy differences of land and oceanic lightning. *Geophysical Research Letters*, 40(10):2390–2394, 2013a. doi: 10.1002/grl.50406.

M L Hutchins, A R Jacobson, R H Holzworth, and J B Brundell. Azimuthal dependence of VLF propagation. *Journal of Geophysical Research: Space Physics*, 118(9):5808–5812, 2013b. doi: 10.1002/jgra.50533.

A R Jacobson, X M Shao, and E Lay. Time domain waveform and azimuth variation of ionospherically reflected VLF/LF radio emissions from lightning. *Radio Science*, 47(4), 2012. doi: 10.1029/2012RS004980.

M H Johnson and J Kierein. Combined release and radiation effects satellite (CRRES): Spacecraft and mission. *Journal of Spacecraft and Rockets*, 29(4): 556–563, 1992. doi: 10.2514/3.55641.

Y Katoh and Y Omura. Electron hybrid code simulation of whistler-mode chorus generation with real parameters in the earth's inner magnetosphere. *Earth, Planets and Space*, 68(1):192, 2016. doi: 10.1186/s40623-016-0568-0.

C A Kletzing, W S Kurth, M Acuna, R J MacDowall, R B Torbert, T Averkamp, D Bodet, S R Bounds, M Chutter, J Connerney, et al. The electric and magnetic field instrument suite and integrated science (EMFISIS) on RBSP. *Space Science Reviews*, 179(1-4):127–181, 2013. doi: 10.1007/s11214-013-9993-6.

W S Kurth, S De Pascuale, J B Faden, C A Kletzing, G B Hospodarsky, S Thaller, and J R Wygant. Electron densities inferred from plasma wave spectra obtained by the Waves instrument on Van Allen Probes. *Journal of Geophysical Research: Space Physics*, 120(2):904–914, 2015. doi: 10.1002/2014JA020857.

W Li, R M Thorne, J Bortnik, G D Reeves, C A Kletzing, W S Kurth, G B Hospodarsky, Harlan E Spence, J B Blake, J F Fennell, et al. An unusual enhancement of low-frequency plasmaspheric hiss in the outer plasmasphere associated with substorm-injected electrons. *Geophysical Research Letters*, 40 (15):3798–3803, 2013. doi: 10.1002/grl.50787.

W Li, L Chen, J Bortnik, R M Thorne, V Angelopoulos, C A Kletzing, W S Kurth, and G B Hospodarsky. First evidence for chorus at a large geocentric distance as a source of plasmaspheric hiss: Coordinated THEMIS and Van Allen Probes observation. *Geophysical Research Letters*, 42(2):241–248, 2015. doi: 10.1002/2014GL062832.

J Manninen, N G Kleimenova, O V Kozyreva, P A Bespalov, and A E Kozlovsky. Non-typical ground-based quasi-periodic vlf emissions observed at l 5.3 under quiet geomagnetic conditions at night. *Journal of Atmospheric and Solar-Terrestrial Physics*, 99:123–128, 2013. doi: 10.1016/j.jastp.2012.05.007.

M Markgraf and O Montenbruck. Total Ionizing Dose Testing of the Orion and Phoenix GPS Recievers. *DLR TN 04-01, Deutsches Zentrum für Luft- und Raumfahrs*, 2004.

AS Maxworth and M Gołkowski. Magnetospheric whistler mode ray tracing in a warm background plasma with finite electron and ion temperature. *Journal of Geophysical Research: Space Physics*, 122(7):7323–7335, 2017. doi: 10.1002/2016JA023546.

C E McIlwain. Coordinates for mapping the distribution of magnetically trapped particles. *Journal of Geophysical Research*, 66(11):3681–3691, 1961. doi: 10.1029/JZ066i011p03681.

N P Meredith, R B Horne, and R R Anderson. Substorm dependence of chorus amplitudes: Implications for the acceleration of electrons to relativistic energies. *Journal of Geophysical Research: Space Physics*, 106(A7):13165–13178, 2001. doi: 10.1029/2000JA900156.

N P Meredith, R B Horne, R M Thorne, D Summers, and R R Anderson. Substorm dependence of plasmaspheric hiss. *Journal of Geophysical Research: Space Physics*, 109(A6), 2004. doi: 10.1029/2004JA010387.

N P Meredith, R B Horne, M A Clilverd, D Horsfall, R M Thorne, and R R Anderson. Origins of plasmaspheric hiss. *Journal of Geophysical Research: Space Physics*, 111(A9), 2006. doi: 10.1029/2006JA011707.

N P Meredith, R B Horne, S A Glauert, and R R Anderson. Slot region electron loss timescales due to plasmaspheric hiss and lightning-generated whistlers. *Journal of Geophysical Research: Space Physics*, 112(A8), 2007. doi: 10.1029/2007JA012413.

N P Meredith, R B Horne, S A Glauert, D N Baker, S G Kanekal, and J M Albert. Relativistic electron loss timescales in the slot region. *Journal of Geophysical Research: Space Physics*, 114(A3), 2009. doi: 10.1029/2008JA013889.

I Nagano, M Mambo, and G Hutatsuishi. Numerical calculation of electromagnetic waves in an anisotropic multilayered medium. *Radio Science*, 10(6):611–617, 1975. doi: 10.1029/RS010i006p00611.

F Němec, O Santolík, M Parrot, and J J Berthelier. Power line harmonic radiation (PLHR) observed by the DEMETER spacecraft. *Journal of Geophysical Research: Space Physics*, 111(A4), 2006. doi: 10.1029/2005JA011480.

F Němec, O Santolík, M Parrot, and J Bortnik. Power line harmonic radiation observed by satellite: Properties and propagation through the ionosphere. *Journal of Geophysical Research: Space Physics*, 113(A8), 2008. doi: 10.1029/2008JA013184.

F Němec, M Parrot, O Santolík, CJ Rodger, MJ Rycroft, M Hayosh, D Shklyar, and A Demekhov. Survey of magnetospheric line radiation events observed by the demeter spacecraft. *Journal of Geophysical Research: Space Physics*, 114 (A5), 2009. doi: 10.1029/2008JA014016.

F Němec, O Santolík, M Parrot, and C J Rodger. Relationship between median intensities of electromagnetic emissions in the VLF range and lightning activity. *Journal of Geophysical Research: Space Physics*, 115(A8), 2010. doi: 10.1029/2010JA015296.

F Němec, K Čížek, M Parrot, O Santolík, and J Záhlava. Line radiation events induced by very low frequency transmitters observed by the DEMETER spacecraft. *Journal of Geophysical Research: Space Physics*, 2017. doi: 10.1002/2017JA024007.

B Ni, J Bortnik, R M Thorne, Q Ma, and L Chen. Resonant scattering and resultant pitch angle evolution of relativistic electrons by plasmaspheric hiss. *Journal of Geophysical Research: Space Physics*, 118(12):7740–7751, 2013. doi: 10.1002/2013JA019260.

Atsuhiro Nishida. Formation of plasmapause, or magnetospheric plasma knee, by the combined action of magnetospheric convection and plasma escape from the tail. *Journal of Geophysical Research*, 71(23):5669–5679, 1966. doi: 10.1029/JZ071i023p05669.

MN Oliven and DA Gurnett. Microburst phenomena: 3. an association between microbursts and vlf chorus. *Journal of Geophysical Research*, 73(7):2355–2362, 1968. doi: 10.1029/JA073i007p02355.

Y Omura, Y Katoh, and D Summers. Theory and simulation of the generation of whistler-mode chorus. *Journal of Geophysical Research: Space Physics*, 113 (A4), 2008. doi: 10.1029/2007JA012622.

E N Parker. Dynamics of the interplanetary gas and magnetic fields. *The Astrophysical Journal*, 128:664, 1958. doi: 10.1086/146579.

M Parrot, D Benoist, J J Berthelier, J Blecki, Y Chapuis, F Colin, F Elie, P Fergeau, D Lagoutte, F Lefeuvre, et al. The magnetic field experiment IMSC and its data processing onboard DEMETER: Scientific objectives, description and first results. *Planetary and Space Science*, 54(5):441–455, 2006. doi: 10.1016/j.pss.2005.10.015.

M Parrot, U S Inan, and N G Lehtinen. V-shaped VLF streaks recorded on DEMETER above powerful thunderstorms. *Journal of Geophysical Research: Space Physics*, 113(A10), 2008. doi: 10.1029/2008JA013336.

M Parrot, J J Berthelier, J Blecki, J Y Brochot, Y Hobara, D Lagoutte, J P Lebreton, F Němec, T Onishi, J L Pinçon, et al. Unexpected very low frequency (VLF) radio events recorded by the ionospheric satellite DEMETER. *Surveys in Geophysics*, 36(3):483–511, 2015. doi: 10.1007/s10712-015-9315-5.

M Parrot, J-L Pinçon, and D Shklyar. Short-fractional hop whistler rate observed by the low-altitude satellite DEMETER at the end of the solar cycle 23. *Journal of Geophysical Research: Space Physics*, 2019. doi: 10.1029/2018JA026176.

M Platino, U S Inan, T F Bell, D A Gurnett, J S Pickett, P Canu, and P M E Décréau. Whistlers observed by the Cluster spacecraft outside the plasmasphere. *Journal of Geophysical Research: Space Physics*, 110(A3), 2005. doi: 10.1029/2004JA010730.

C Price and M Blum. ELF/VLF radiation produced by the 1999 leonid meteors. *Earth Moon and Planets*, 82-83:545–554, 01 1998. doi: 10.1023/A:1017033320782.

V A Rakov and M A Uman. *Lightning: physics and effects*. Cambridge University Press, 2003. ISBN 9780521583275.

B W Reinisch and I A Galkin. Global ionospheric radio observatory (giro). *Earth, planets and space*, 63(4):377–381, 2011. doi: 10.5047/eps.2011.03.001.

Craig J Rodger, Mark A Clilverd, Keith H Yearby, and Andy J Smith. Magnetospheric line radiation observations at halley, antarctica. *Journal of Geophysical Research: Space Physics*, 104(A8):17441–17447, 1999. doi: 10.1029/1999JA900153.

Craig J Rodger, Mark A Clilverd, Keith H Yearby, and Andy J Smith. Is magnetospheric line radiation man-made? *Journal of Geophysical Research: Space Physics*, 105(A7):15981–15990, 2000. doi: 10.1029/1999JA000413.

S D Rudlosky and D T Shea. Evaluating wwlln performance relative to trmm/lis. *Geophysical Research Letters*, 40(10):2344–2348, 2013. doi: 10.1002/grl.50428.

M J Rycroft, S Israelsson, and C Price. The global atmospheric electric circuit, solar activity and climate change. *Journal of Atmospheric and Solar-Terrestrial Physics*, 62(17-18):1563–1576, 2000. doi: 10.1016/S1364-6826(00)00112-7.

M J Rycroft, K A Nicoll, K L Aplin, and R G Harrison. Recent advances in global electric circuit coupling between the space environment and the troposphere. *Journal of Atmospheric and Solar-Terrestrial Physics*, 90:198–211, 2012. doi: 10.1016/j.jastp.2012.03.015.

O Santolik and D A Gurnett. Propagation of auroral hiss at high altitudes. *Geophysical Research Letters*, 29(10), 2002. doi: 10.1029/2001GL013666.

O Santolík and M Parrot. Propagation analysis of electromagnetic waves between the helium and proton gyrofrequencies in the low-altitude auroral zone. *Journal of Geophysical Research: Space Physics*, 103(A9):20469–20480, 1998. doi: 10.1029/98JA01386.

O Santolík and M Parrot. Case studies on the wave propagation and polarization of ELF emissions observed by Freja around the local proton gyrofrequency. *Journal of Geophysical Research: Space Physics*, 104(A2):2459–2475, 1999. doi: 10.1029/1998JA900045.

O Santolik, M Parrot, L R O Storey, J S Pickett, and D A Gurnett. Propagation analysis of plasmaspheric hiss using Polar PWI measurements. *Geophysical Research Letters*, 28(6):1127–1130, 2001. doi: 10.1029/2000GL012239.

O Santolik, D A Gurnett, J S Pickett, M Parrot, and N Cornilleau-Wehrlin. Spatio-temporal structure of storm-time chorus. *Journal of Geophysical Research: Space Physics*, 108(A7), 2003. doi: 10.1029/2002JA009791.

O Santolík, M Parrot, and F Lefeuvre. Singular value decomposition methods for wave propagation analysis. *Radio Science*, 38(1), 2003. doi: 10.1029/2000RS002523.

O Santolík, J Chum, M Parrot, D A Gurnett, J S Pickett, and N Cornilleau-Wehrlin. Propagation of whistler mode chorus to low altitudes: Spacecraft observations of structured ELF hiss. *Journal of Geophysical Research: Space Physics*, 111(A10), 2006a. doi: 10.1029/2005JA011462.

O Santolík, F Němec, M Parrot, D Lagoutte, L Madrias, and J J Berthelier. Analysis methods for multi-component wave measurements on board the DEMETER spacecraft. *Planetary and Space Science*, 54(5):512–527, 2006b. doi: 10.1016/j.pss.2005.10.020.

O Santolík, M Parrot, U S Inan, D Burešová, D A Gurnett, and J Chum. Propagation of unducted whistlers from their source lightning: A case study. *Journal of Geophysical Research: Space Physics*, 114(A3), 2009. doi: 10.1029/2008JA013776.

O Santolík, J S Pickett, D A Gurnett, J D Menietti, B T Tsurutani, and O Verkhoglyadova. Survey of Poynting flux of whistler mode chorus in the outer zone. *Journal of Geophysical Research: Space Physics*, 115(A7), 2010. doi: 10.1029/2009JA014925.

O Santolík, E Macúšová, I Kolmašová, N Cornilleau-Wehrlin, and Y Conchy. Propagation of lower-band whistler-mode waves in the outer Van Allen belt: Systematic analysis of 11 years of multi-component data from the Cluster spacecraft. *Geophysical Research Letters*, 41(8):2729–2737, 2014. doi: 10.1002/2014GL059815.

S S Sazhin and M Hayakawa. Magnetospheric chorus emissions: A review. *Planetary and space science*, 40(5):681–697, 1992. doi: 10.1016/0032-0633(92)90009-D.

R L Smith and J J Angerami. Magnetospheric properties deduced from OGO 1 observations of ducted and nonducted whistlers. *Journal of Geophysical Research*, 73(1):1–20, 1968. doi: 10.1029/JA073i001p00001.

M J Starks, R A Quinn, G P Ginet, J M Albert, G S Sales, B W Reinisch, and P Song. Illumination of the plasmasphere by terrestrial very low frequency transmitters: Model validation. *Journal of Geophysical Research: Space Physics*, 113(A9), 2008. doi: 10.1029/2008JA013112.

T H Stix. *Waves in plasmas*. Springer Science & Business Media, 1992.

L R O Storey. An investigation of whistling atmospherics. *Philosophical Transactions of the Royal Society of London A: Mathematical, Physical and Engineering Sciences*, 246(908):113–141, 1953. doi: 10.1098/rsta.1953.0011.

D Summers, B Ni, N P Meredith, R B Horne, R M Thorne, M B Moldwin, and R R Anderson. Electron scattering by whistler-mode ELF hiss in plasmaspheric plumes. *Journal of Geophysical Research: Space Physics*, 113(A4), 2008. doi: 10.1029/2007JA012678.

X Tao, J Bortnik, and M Friedrich. Variance of transionospheric VLF wave power absorption. *Journal of Geophysical Research: Space Physics*, 115(A7), 2010. doi: 10.1029/2009JA015115.

R M Thorne, E J Smith, R K Burton, and R E Holzer. Plasmaspheric hiss. *Journal of Geophysical Research*, 78(10):1581–1596, 1973. doi: 10.1029/JA078i010p01581.

R M Thorne, R B Horne, and N P Meredith. Comment on "On the origin of whistler mode radiation in the plasmasphere" by Green et al. *Journal of Geophysical Research: Space Physics*, 111(A9), 2006. doi: 10.1029/2005JA011477.

R M Thorne, W Li, B Ni, Q Ma, J Bortnik, D N Baker, Harlan E Spence, G D Reeves, M G Henderson, C A Kletzing, et al. Evolution and slow decay of an unusual narrow ring of relativistic electrons near L˜ 3.2 following the September 2012 magnetic storm. *Geophysical Research Letters*, 40(14):3507–3511, 2013. doi: 10.1002/grl.50627.

S Toledo-Redondo, M Parrot, and A Salinas. Variation of the first cut-off frequency of the Earth-ionosphere waveguide observed by DEMETER. *Journal of Geophysical Research: Space Physics*, 117(A4), 2012. doi: 10.1029/2011JA017400.

B T Tsurutani and E J Smith. Postmidnight chorus: A substorm phenomenon. *Journal of Geophysical Research*, 79(1):118–127, 1974.

B T Tsurutani and E J Smith. Two types of magnetospheric ELF chorus and their substorm dependences. *Journal of Geophysical Research*, 82(32):5112–5128, 1977. doi: 10.1029/JA082i032p05112.

B T Tsurutani, B J Falkowski, O P Verkhoglyadova, J S Pickett, O Santolík, and G S Lakhina. Dayside ELF electromagnetic wave survey: A Polar statistical study of chorus and hiss. *Journal of Geophysical Research: Space Physics*, 117 (A9), 2012. doi: 10.1029/2011JA017180.

University of Calgary. Above an array for broadband observations of VLF/ELF emissions: http://www.ucalgary.ca/above/node/34 (7.1.2016), 2012.

J A Van Allen. Observation of high intensity radiation by satellites 1958 Alpha and Gamma. *Journal of Jet Propulsion*, 28(9):588–592, 1958. doi: 10.2514/8.7396.

J A Van Allen and L A Frank. Radiation around the Earth to a radial distance of 107,400 km. *Nature*, 183, 1959. doi: 10.1038/183430a0.

H D Voss, M Walt, W L Imhof, J Mobilia, and U S Inan. Satellite observations of lightning-induced electron precipitation. *Journal of Geophysical Research: Space Physics*, 103(A6):11725–11744, 1998. doi: 10.1029/97JA02878.

A D Watt and R D Croghan. Comparison of observed VLF attenuation rates + excitation factors with theory. *JOURNAL OF RESEARCH OF THE NATIONAL BUREAU OF STANDARDS SECTION D-RADIO SCIENCE*, 500 (1):1–+, 1964. doi: 10.6028/jres.068D.006.

E R Williams. The tripole structure of thunderstorms. *Journal of Geophysical Research: Atmospheres*, 94(D11):13151–13167, 1989. doi: 10.1029/JD094iD11p13151.

J Záhlava, F Němec, O Santolík, I Kolmašová, M Parrot, and C J Rodger. Very low frequency radio events with a reduced intensity observed by the low-altitude DEMETER spacecraft. *Journal of Geophysical Research: Space Physics*, 120 (11):9781–9794, 2015. doi: 10.1002/2015JA021607.

J Záhlava, F Němec, J L Pinçon, O Santolík, I Kolmašová, and M Parrot. Whistler influence on the overall VLF wave intensity in the upper ionosphere. *Journal of Geophysical Research: Space Physics*, 123(7):5648–5660, 2018a. ISSN 2169-9380. doi: 10.1029/2017JA025137.

J Záhlava, F Němec, O Santolík, I Kolmašová, G B Hospodarsky, M Parrot, W S Kurth, J Bortnik, and C Kletzing. Longitudinal dependence of whistler mode electromagnetic waves in the earth's inner magnetosphere. *Journal of Geophysical Research: Space Physics*, 123(8):6562–6575, 2018b. ISSN 2169-9380. doi: 10.1029/2018JA025284.

J Záhlava, F Němec, O Santolík, I Kolmašová, M Parrot, and D Kouba. Selective attenuation of lightning-generated whistlers at extralow frequencies observed by a low-altitude spacecraft. *Journal of Geophysical Research: Space Physics*, 123(10):8631–8640, 2018c. ISSN 2169-9380. doi: 10.1029/2018JA025879.

J Záhlava, F Němec, O Santolík, I Kolmašová, G B Hospodarsky, M Parrot, W S Kurth, and C Kletzing. Lightning contribution to overall whistler mode wave intensities in the plasmasphere. *Geophysical Research Letters*, 46:8607–8616, 2019.

H Zell. Radiation belts with satelites: http://www.nasa.gov/sites/default/files/images/730056main_20130228-radiationbelts-orig_full.jpg (10.3.2016), NASA, 2015.

List of publications

Publications appended to the thesis

A1: Záhlava, J., Němec, F., Santolík, O., Kolmašová, I., Parrot, M., Rodger, C.J., Very low frequency radio events with a reduced intensity observed by the low-altitude DEMETER spacecraft. *J. Geophys. Res. Space Phys.* **120**(11): 9781–9794, 2015, doi:10.1002/2015JA021607.

A2: Záhlava, J., Němec, F., Pincon, J.L., Santolík, O., Kolmašová, I., Parrot, M., Whistler Influence on the Overall Very Low Frequency Wave Intensity in the Upper Ionosphere. *J. Geophys. Res. Space Phys.* **123**(7): 5648–5660, 2018, doi:10.1002/2017JA025137.

A3: Záhlava, J., Němec, F., Santolík, O., Kolmašová, I., Hospodarsky, G.B., Parrot, M., Kurth, W.S., Bortnik, J., Kletzing, C., Longitudinal Dependence of Whistler Mode Electromagnetic Waves in the Earth's Inner Magnetosphere. *J. Geophys. Res. Space Phys.* **123**(8): 6562–6575, 2018, doi:10.1029/2018JA025284.

A4: Záhlava, J., Němec, F., Santolík, O., Kolmašová, I., Parrot, M., Kouba, D., Selective Attenuation of Lightning-Generated Whistlers at Extralow Frequencies: DEMETER Spacecraft Observations. *J. Geophys. Res. Space Phys.* **123**(10): 8631–8640, 2018, doi:10.1029/2018JA025879.

A5: Záhlava, J., Němec, F., Santolík, O., Kolmašová, I., Hospodarsky, G.B., Parrot, M., Kurth, W.S., Kletzing, C., Lightning contribution to overall whistler mode wave intensities in the plasmasphere. *Geophys. Res. Lett.* **46**: 8607–8616, 2019, doi:10.1029/2019GL083918.

Other publications

- Němec, F., Čížek, K., Parrot, M., Santolík, O., Záhlava, J., Line radiation events induced by very low frequency transmitters observed by the DEMETER spacecraft. *J. Geophys. Res. Space Phys.* **122**(7): 7226–7239, 2017, doi:10.1002/2017JA024007.

- Záhlava, J., Němec, F., Santolík, O., Kolmašová, I., Hospodarsky, G.B., Kurth, W.S., Kletzing, C., Parrot, M., Longitudinal Dependence of the Intensity of Whistler Mode Electromagnetic Emissions, *in WDS'17 Proceedings of Contributed Papers - Physics*, eds. J. Safrankova and J. Pavlu, Prague, Matfyzpress, pp. 46-54, ISBN 978-80-7378-356-3, 2017.

- Záhlava, J., Němec, F., Santolík, O., Kolmašová, I., Parrot, M., Lightning Contribution to the VLF Wave Intensity Observed by DEMETER in the Upper Ionosphere, *in WDS'18 Proceedings of Contributed Papers - Physics*, eds. J. Safrankova and J. Pavlu, Prague, Matfyzpress, pp. 77-84, ISBN 978-80-7378-374-7, 2018.

- Bezděková, B., Němec, F., Parrot, M., Hajoš, M., Záhlava, J., Santolík, O., Dependence of Properties of Magnetospheric Line Radiation and Quasiperiodic Emissions on Solar Wind Parameters and Geomagnetic Activity. *J. Geophys. Res. Space Phys.* **124**(4): 2552–2568, 2019, doi:10.1029/2018JA026378.

A1 - Záhlava et al. [2015]

Záhlava, J., Němec, F., Santolík, O., Kolmašová, I., Parrot, M., Rodger, C.J., Very low frequency radio events with a reduced intensity observed by the low-altitude DEMETER spacecraft. *J. Geophys. Res. Space Phys.* **120**(11): 9781–9794, 2015, doi:10.1002/2015JA021607.

A2 - Záhlava et al. [2018a]

Záhlava, J., Němec, F., Pincon, J.L., Santolík, O., Kolmašová, I., Parrot, M., Whistler Influence on the Overall Very Low Frequency Wave Intensity in the Upper Ionosphere. *J. Geophys. Res. Space Phys.* **123**(7): 5648–5660, 2018, doi:10.1002/2017JA025137.

A3 - Záhlava et al. [2018b]

Záhlava, J., Němec, F., Santolík, O., Kolmašová, I., Hospodarsky, G.B., Parrot, M., Kurth, W.S., Bortnik, J., Kletzing, C., Longitudinal Dependence of Whistler Mode Electromagnetic Waves in the Earth's Inner Magnetosphere. *J. Geophys. Res. Space Phys.* **123**(8): 6562–6575, 2018, doi:10.1029/2018JA025284.

A4 - Záhlava et al. [2018c]

Záhlava, J., Němec, F., Santolík, O., Kolmašová, I., Parrot, M., Kouba, D., Selective Attenuation of Lightning-Generated Whistlers at Extralow Frequencies: DEMETER Spacecraft Observations. *J. Geophys. Res. Space Phys.* **123**(10): 8631–8640, 2018, doi:10.1029/2018JA025879.

A5 - Záhlava et al. [2019]

Záhlava, J., Němec, F., Santolík, O., Kolmašová, I., Hospodarsky, G.B., Parrot, M., Kurth, W.S., Kletzing, C., Lightning contribution to overall whistler mode wave intensities in the plasmasphere. *Geophys. Res. Lett.* **46**: pp 8607–8616, 2019, doi:10.1029/2019GL083918.